Shot Noise Detection in Carbon Nanotube Quantum Dots

Dissertation
zur Erlangung des Doktorgrades der Naturwissenschaften
(Dr. rer. nat.)
der Fakultät für Physik
der Universität Regensburg

vorgelegt von

Daniel Steininger
aus
Passau

im Jahr 2017

Die Arbeit wurde von Prof. Dr. Christoph Strunk angeleitet.
Das Promotionsgesuch wurde am 07.07.2016 eingereicht.
Das Kolloquium fand am 11.05.2017 statt.

Prüfungsausschuss:	Vorsitzender:	Prof. Dr. Vladimir Braun
	1. Gutachter:	Prof. Dr. Christoph Strunk
	2. Gutachter:	Prof. Dr. Milena Grifoni
	weiterer Prüfer:	Prof. Dr. Dominique Bougeard

Contents

1 Introduction

Shot noise investigations have become a matter of growing interest in the community of mesoscopic physics within the last twenty years as it opens up a great number of new possibilities for the study of transport phenomena in electrical conductors.
The field of mesoscopic physics usually deals with measurements of electrical current through small conductors somewhere in the range of 100 nm to 1 µm. One can imagine that the current and voltage amplitudes in such a small conductor have to be of equally small magnitude, as opposed to macroscopic devices. Electrical current is defined as the number of charge carriers with charge q which move in a time interval Δt. Charge carriers obey certain statistical processes when passing a conductor for instance due to scattering mechanisms. That means that the number of charges within a small time interval is not constant, leading to fluctuations in the current. This effect only becomes visible for a small number of charge carriers in a limited number of transport channels. Transport statistics then obey a Poissonian distribution which manifests as white noise in the average current signal $\langle \mathrm{I} \rangle$. The measured noise power spectral density $i_S^2 = S_I \propto \langle I^2 \rangle - \langle I \rangle^2$ is directly proportional to the variance of the signal and also to the average current through the conductor and reads as $\mathrm{S_I} = 2\mathrm{q}\langle \mathrm{I} \rangle$. This effect was first discovered in 1918 by Walter Schottky [1] when he investigated the current of a small number of electrons in vacuum tubes. The discovery of shot noise is closely linked to the development of sensitive amplifiers which made it possible to detect such small currents in the first place. With shot noise measurements, additional information is accessible which is otherwise discarded in standard transport measurements in mesoscopic devices: figure 1.1 shows two different examples of current signals (black). Due to a certain integration time defined by the dc measurement device, the signal one can obtain in such a measurement is restricted to an average current represented as a red line. While the actual signals look completely different, the measured dc current is exactly the same. What is lost in dc transport investigations is the amplitude of current fluctuations or the variance of the signal.
Acquiring noise, i.e., the variance of the noise signal, as additional data in the course of a transport experiment can give us a powerful tool to gain a deeper understanding of the processes in our devices [2–6]. Or as it was stated by Rolf Landauer's publication "The noise is the signal" [7] from 1998: "Noise is not only a hindrance to signal detection. Advances in measurement techniques mean that it can now be used to probe the kinetics of electrons."

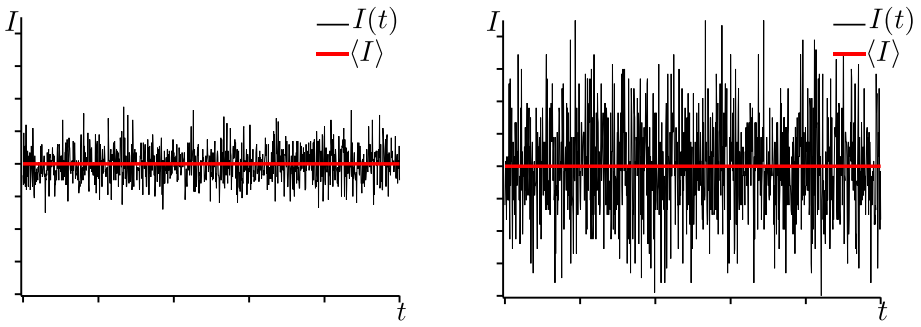

Figure 1.1: Two examples of different noise signals where the average current (red) however is similar in both cases. The variance of the signal is lost in dc measurements.

Having access to noise data makes it for example possible to determine the charge q in systems where $q \neq e$ and exotic charge carriers are involved in the transport. For instance quasi-particles in the fractional quantum Hall regime [8, 9] or Cooper pairs in superconductor-hybrid systems [10] where q is a fraction or a multiple of e.
Also correlations of charge carriers which often occur in mesoscopic devices can lead to a suppression of noise even down to zero in a completely open channel with transmission $T = 1$ [11, 12]. Shot noise can also account for other distinct values like in double barrier systems (quantum dots), where the noise usually is $S = 1/2 \times S_I$ [13]. In disordered wires noise values of $S = 1/3 \times S_I$ can be observed [14, 15], while in open chaotic cavities $S = 1/4 \times S_I$ [4, 16].
In multi-terminal devices measurements of cross-correlations of two noise signals can open even further possibilities: while canceling out unwanted intrinsic noise from the amplifiers used in the experiment, correlation measurements can at the same time give information about electron bunching or anti-bunching [17, 18]. Electron-electron correlations which usually are negative since fermions obey Fermi-Dirac statistics can also become positive when two electrons arrive at two detectors at the same time. This is for instance the case when they originate from the same source, for instance a Cooper-pair from a superconductor which was separated in a so called *Cooper-pair splitter* device (CPS) [19–21].
All these examples give us the motivation to establish a system in our group which is capable of not only measuring the resistance of conductors at low temperatures but also acquires noise data. The goal was the development and construction of a state of the art amplifier setup customized for our existing low temperature measurement system, capable of detecting current noise in the range of $S_I \sim 10^{-30}\,A^2/Hz$ at low temperatures. After testing and calibrating the setup, first noise measurements in carbon nanotube based quantum dot devices should prove the functionality of our setup and also give first insight in the transport mechanisms in such devices.
This work is organized as follows: in chapter 2 the basic theoretical ingredients for understanding the subsequent chapters are presented. After giving a first introduction to

our material system, i.e., carbon nanotubes, the basics of quantum dots and Coulomb blockade are explained. The last section in chapter 2 then deals with noise and noise measurement techniques in general. In the main chapter 3 the construction of our cryogenic amplifier system in described in detail. Together with additional technical information provided in the appendix, this chapter covers the entire process including the planning and simulation, the construction and software implementations and finally the calibration of our setup.
The experimental methods needed for our shot noise investigations in this work are demonstrated in chapter 4, starting with the processes of device fabrication. Later details about the measurement setup including the cryogenic environment and the measurement procedure are shown here.
The most important results of our first measurements in our new noise setup are collected in chapter 5. After an extensive electronic characterization of our carbon nanotube device at low temperatures we acquired a large amount of noise data. Parts of it, which we were able to interpret together with the theory group of Prof. Milena Grifoni are presented here. After a general discussion and outlook in chapter 6 we want to briefly show additional transport and noise data from the same device in the appendix (A) which still lack proper interpretation.

2 Basics

The following chapter introduces the basic principles and theoretical background for this work.
First carbon nanotubes (CNTs) as the material system of choice are introduced with respect to their structural and electronic properties followed by the electronic transport mechanisms in CNTs.
Later the essentials of Coulomb blockade, quantum dots in general as well as the special case of carbon nanotubes are discussed. Many quantities which become important later in the interpretation of the experimental results are defined here.
Since the focus of this work lies on noise measurements, the last section of this chapter is dealing with the various sources of noise in physical experiments as well as measurement techniques and gives a short overview of previous noise experiments and theoretical predictions of noise in quantum dots.

2.1 Carbon Nanotubes

This section is intended to provide an overview of the general properties of carbon nanotubes. First the atomic structure for different types of carbon crystals is introduced, later we focus on the electronic properties which will then lead to the different electronic transport mechanisms present in this material system. This section is following references [22–36].

2.1.1 Structural Properties

Pure carbon appears in different shapes and atomic configurations, such as diamond, graphite, graphene, fullerenes or carbon nanotubes. These carbon molecules are classified by their atomic bonds between the carbon atoms. The crystal structure of diamond for instance is formed by the so called sp^3 hybridization where one s-orbital and three p-orbitals hybridize to form four sp^3-orbitals. This results in a tetrahedral structure with angles of 109.5 ° between the atomic sites. *Diamond* is known to be transparent and the hardest natural material in the world (10 on Mohs scale). It is semiconducting with a large band gap of about 6 eV.

Graphite on the other hand consists of many layers of sp^2 hybridized carbon. In this configuration one *s*-orbital and two *p*-orbitals form three sp^2 orbitals. The resulting hexagonal structure is a two dimensional sheet with angles of 120 ° between the atoms. Such a single layer is called *graphene*. Graphite as a stack of many layers of carbon has been studied for a long time [37], however the experimental isolation of one single layer of graphene first succeeded in 2004 [38]. Andre Gaim and Konstantin Novoselov were eventually awarded the Nobel Prize in Physics in 2010 for their work.
*Carbon nanotube*s (CNTs) can be illustrated as a sheet of graphene rolled up to form a cylinder (tube). These *single walled carbon nanotubes* (SWCNTs) consist of only one layer of graphene (see figure 2.1). The wall thickness therefore corresponds to the size of one carbon atom.

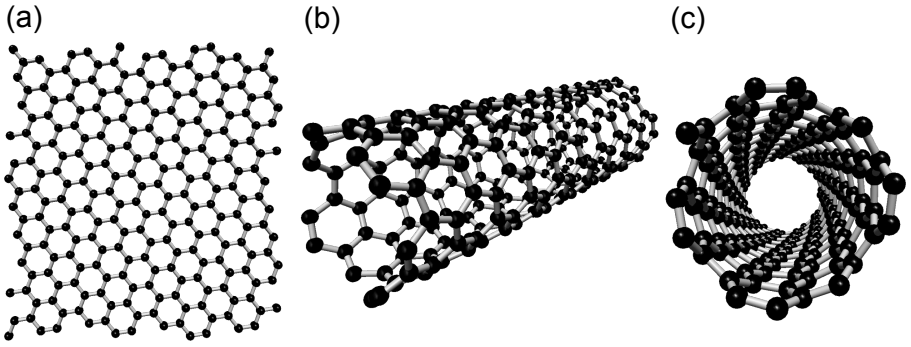

Figure 2.1: 3D model of a carbon nanotube with chiral angle $\vec{C}$=(7,4) as also shown in figure 2.2. (a) Shows the underlying graphene sheet. (b) A carbon nanotube forms by rolling up the sheet along the translational vector $\vec{T}$ (see figure 2.2). (c) View along the CNT's axis through the tube. Created with *Nanotube Modeler 1.7.6* (© JCrystalSoft, 2015)

A coaxial arrangement of multiple tubes inside each other is known as *multi walled carbon nanotube* (MWCNT). These different types of CNTs can as well be found as bundles or ropes consisting of many SWCNTs, MWCNTs or both sticking together by means of van der Waals forces. Carbon fiber-like structures have been observed already in 1952 and 1986 [39, 40]. Yet the first clear observation of MWCNTs using a high resolution transmission electron microscope was achieved in 1991 in the labs of NEC in Japan [41]. Two years later in 1993 the first SWCNTs could be synthesized and observed [42, 43]. As it turned out in further investigations, carbon nanotubes exhibit a number of remarkable features such as a Young's modulus of $\sim 1\,\mathrm{TPa}$ which makes CNTs one of the stiffest materials known today [44,45]. Furthermore they can sustain a current density of $\sim 10^9\,\mathrm{A/cm^2}$ in electrical transport measurements [46].

Carbon nanotubes can be synthesized in different ways such as arc discharge, laser ablation, high pressure CO conversion (HiPCO) and chemical vapor deposition (CVD) [22]. The latter approach is the method of choice in this work and can be briefly described

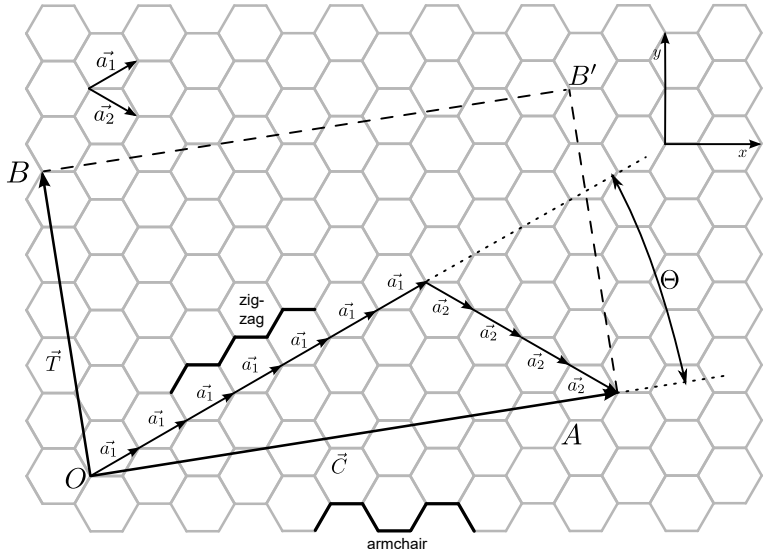

Figure 2.2: Honeycomb lattice of graphene as the underlying structure of a carbon nanotube: the chiral vector $\vec{C}$ and the translational vector $\vec{T}$ define the surface area of the nanotube.

as follows: a sample chip with catalyst material[1] on top is heated up in an atmosphere of hydrocarbon gases like methane CH_4 or ethylene C_2H_4. At temperatures of 600 °C - 1200 °C the process gas decomposes and carbon tubes start to grow out of the catalyst particles. This process is presented in more detail in chapter 4.1 and in appendix C.2.

As the crystal structure of single walled carbon nanotubes is similar to the one of a flat graphene sheet they are usually labeled in terms of graphene lattice vectors $\vec{a_1}$ and $\vec{a_2}$ which define the unit cell of graphene (figure 2.2). A single walled carbon nanotube is obtained by seamlessly rolling up a sheet of graphene along the so called *chiral-* or *circumferential vector* $\vec{C}$ which is defined as

$$\vec{C} = m \cdot \vec{a_1} + n \cdot .\vec{a_2}. \tag{2.1}$$

The *chiral indices* m and n therefore define the entire structure of a regular SWCNT including the *chiral angle* Θ which describes the tilt angle of the hexagon structure with respect to the nanotube axis.

$$\Theta = \arctan\left(\frac{\sqrt{3}m}{m+2n}\right) \tag{2.2}$$

Figures 2.1 and 2.2 show examples for a $(n,m) = (7,4)$ type nanotube. The chiral angle Θ is in the range of $0° \leq |\Theta| \leq 30°$. One can distinguish different species of SWCNTs: *zig-zag*, where $(n,m) = (n,0)$ and $\Theta = 0°$ which show a zig-zag like pattern along the

[1] As catalyst material often a mixture of different nano particles is used. Another possibility is the deposition of a non-continuous thin metal film.

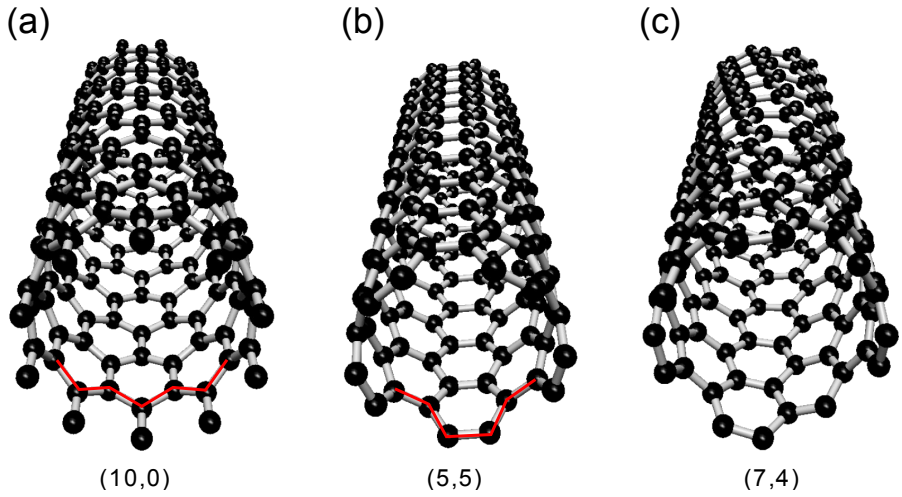

Figure 2.3: The three different species of single walled carbon nanotubes. The red lines in the 3D models emphasize the shape of the nanotube edges: (a) Zig-zag $(n,m) = (10,0)$, (b) armchair $(n,m) = (5,5)$ and (c) chiral $(n,m) = (7,4)$ (as in figures 2.2 and 2.1). Created with *Nanotube Modeler 1.7.6* (© JCrystalSoft, 2015)

circumference, *armchair*, where $(n,m) = (n,n)$ and $\Theta = 30°$ which exhibit an armchair pattern and general *chiral* tubes with $(n, m \neq n \neq 0)$ and $0° < |\Theta| < 30°$ (see figure 2.3)
The diameter of a nanotube d_{CNT} can be estimated by the formula

$$d_{CNT} = \left|\frac{\vec{C}}{\pi}\right| = \frac{a}{\pi}\sqrt{n^2 + nm + m^2} \tag{2.3}$$

where $a = \sqrt{(3)}a_{cc}$ with $a_{cc} \simeq 0.142\,\text{nm}$ is the lattice constant of graphene, i.e., the distance from one carbon atom to its nearest neighbor.
The area $OABB'$ in figure 2.2 spanned by the vectors $\vec{C}$ and $\vec{T}$, is known as the unit cell of the carbon nanotube. The number of hexagons that define the unit cell of the CNT is defined by the the relation

$$N = \frac{|\vec{C} \times \vec{T}|}{|\vec{a_1} \times \vec{a_2}|}. \tag{2.4}$$

Each graphene unit cell consists of two atoms. Therefore the number of carbon atoms in one unit cell of the CNT is $2N$.

2.1.2 Electronic Properties

The electronic structure of carbon nanotubes can be directly deduced from the graphene band structure as the crystal lattices of both are similar. Here again the consideration of CNTs being formed by rolling up a flat sheet of graphene is employed. Figure 2.4 (a) shows the primitive unit cell of graphene in real space (green shaded area) consisting of two atoms and the corresponding base vectors a_1 and a_2. The reciprocal lattice of

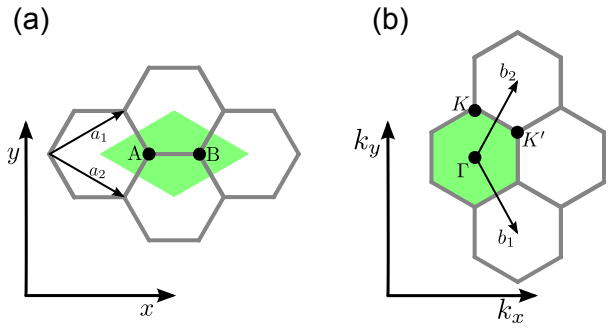

Figure 2.4: (a) The primitive unit cell of graphene in real space (green area) containing two atoms A and B. The unit cell is spanned by the two base vectors $\vec{a_1}$ and $\vec{a_2}$. (b) Reciprocal lattice of graphene, the hexagonal first Brillouin zone is indicated in green. $\vec{b_1}$ and $\vec{b_2}$ are the corresponding base vectors in reciprocal space.

graphene as well as its first Brillouin zone are again hexagonal (see green shaded area in figure 2.4 (b). Within the tight binding approach the dispersion relation of graphene can be expressed as

$$E(k_x, k_y) = \pm\gamma_0 \left[1 + 4\cos\left(\frac{\sqrt{3}k_x a}{2}\right)\cos\left(\frac{k_y a}{2}\right) + 4\cos^2\left(\frac{k_y a}{2}\right)\right]^{1/2}, \tag{2.5}$$

where $\gamma_0 \approx 3\,\text{eV}$ is the hopping energy between carbon atoms.
A plot of this expression is shown in figure 2.5. One can immediately see that the conduction and the valence band touch at six discrete points in the $k_x - k_y$ plane at zero energy. These six points are the corners of the Brillouin zone as also indicated in figure 2.4. They can be classified by two triplets of points K and K' which are equivalent under lattice translation.

Now the "rolling up" of the graphene sheet to a carbon nanotube is taken into account when calculating the dispersion relation. This so called *zone folding* method leads to periodic boundary conditions for electron moving along the chiral vector $\vec{C}$, that is perpendicular to the tube's axis $\vec{T}$ around its circumference. As a consequence the corresponding wave vector component perpendicular to the tube axis becomes quantized: $k_\perp = \vec{k}\cdot\vec{C} = 2\pi q$ where $(q = 0, 1, 2, ..., 2n)$. The component parallel to $\vec{T}$ remains continuous as long as the CNT length is assumed infinite. This quantization of the k-vector shows as cuts through the graphene dispersion indicated as white dashed lines in figure 2.5. The spacing of these subbands is inversely proportional to the nanotube diameter $\Delta k = 2/d$ and their orientation in the reciprocal space is determined by the chiral vector Θ. The spacing and the orientation are very important parameters as they determine whether the nanotube is metallic or semiconducting. As depicted in figure 2.6 the graphene dispersion relation can be approximated as linear for low energies, forming a cone-like shape around the K points where valence and conduction band touch. The quantization in-

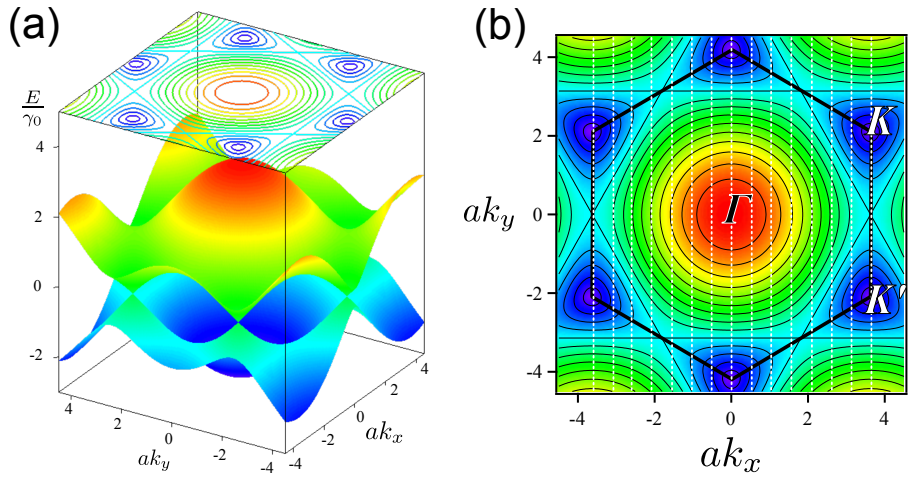

Figure 2.5: (a) The dispersion relation of graphene as a result of tight binding calculations. The valence and the conduction band touch at six points in the reciprocal lattice. For symmetry reasons these points fall into two distinguishable triplets called K and K'. Close to this points the dispersion relation can be approximated as linear. The Fermi energy lies exactly in between the valence and conduction band and therefore only consists of six points. (b) As a consequence of "rolling up" the graphene lattice into a CNT, additional boundary conditions around the tube's circumference for k_x are introduced. This results in a discretization of allowed $\vec{k}$ vectors (indicated by white lines).

duced by zone folding leads now to numerous subbands which can be imagined as cuts through the cones along the k_y direction. When the cut intersects with a K point the resulting subband is linear and the tube is metallic (red line in figure 2.6). Any other cut away from the K points causes hyperbolic dispersion relations with a band gap between valence and conduction band. These tubes are semiconducting (blue line in figure 2.6). Only nanotubes where the chiral indices are such that $(n-m)/3 \in \mathbb{Z}$ are metallic.

2.1.3 Electronic Transport in CNTs

In a macroscopic conductor electron transport is diffusive. The conductance is given by $G = \sigma A/L$, where L and A are the length and the cross sectional area of the conductor and σ is the specific conductance which depends on the material. For the resistance the inverse relation $R = 1/G = \rho L/A$ with the specific resistance ρ holds true. When the dimensions of the conductor become smaller than the mean free path of an electron L_m and the phase coherence length L_ϕ, transport can take place without scattering (*ballistic transport*). For a noninteracting system it is conveniently described by the Landauer-Büttiker formalism [4, 47]. Current through such a mesoscopic structure connected to two electron reservoirs with a Fermi-Dirac density of states is defined by

$$I = \frac{e}{h} \int d\epsilon (f_L(\epsilon) - f_R(\epsilon)) T(\epsilon), \tag{2.6}$$

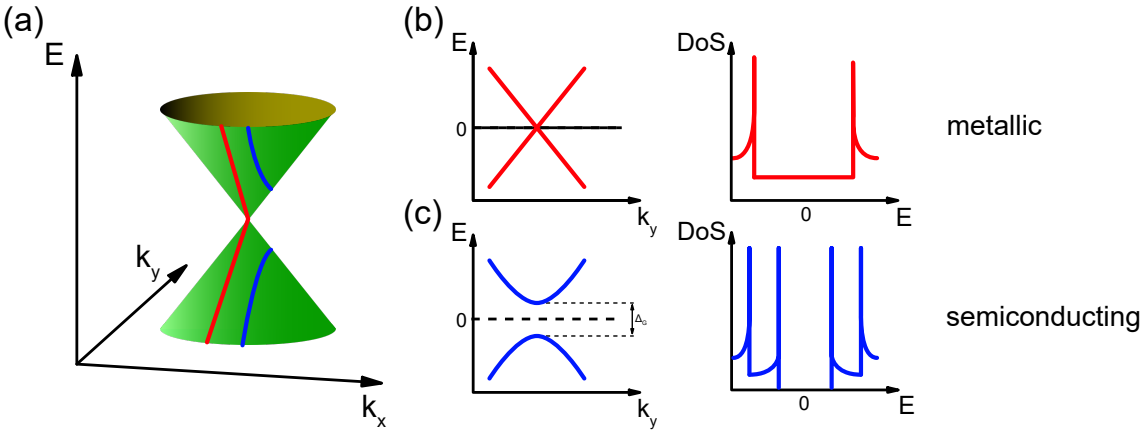

Figure 2.6: (a) At low energies the dispersion relation of graphene can be approximated as cones around the K point. The quantization due to zone folding leads to discrete cuts of the graphene dispersion, which then form the subbands of the CNT dispersion. If the cut lies exactly on a K point (red lines) the CNT dispersion is linear, therefore the tube is metallic. If the cut through the cone does not run through a K point (blue line) the CNT dispersion has hyperbolic shape and features a gap between valence and conduction band and the nanotube is semiconducting. (b) The corresponding density of states for a metallic tube features constant values around K while in the semiconducting case (c) the density of states is zero within the gap.

with the transmission probability $T(\epsilon)$ and the Fermi-Dirac distribution

$$f_{L,R}(E) = \frac{1}{1 + e^{(E-\mu_{L,R})/k_B T}}. \tag{2.7}$$

The conductance of such a system is given by

$$G(\epsilon') = \frac{e^2}{h} \int d\epsilon T(\epsilon) F_T(\epsilon - \epsilon'), \tag{2.8}$$

where $F_T(\epsilon - \epsilon') = -\frac{d}{d\epsilon}(e^{(\epsilon-\epsilon')/k_B T} + 1)^{-1}$ is the thermal broadening function. In the limit of zero temperature the thermal broadening becomes a Dirac-δ function and the result of the integral is

$$G(\epsilon') = \frac{e^2}{h} T(\epsilon'). \tag{2.9}$$

Therefore the maximum conductance of a mesoscopic conductor in the ballistic transport regime with full transmission ($T = 1$) can not be larger than $G_{max} = e^2/h$. Here one transport channel was taken into account, however because of K, K' and spin degeneracy four transport channels are available in a carbon nanotube. Therefore the maximum conductance in a carbon nanotube can be

$$G_{max} = 4\frac{e^2}{h}, \tag{2.10}$$

and the minimal resistance

$$R_{min} = 1/G_{max} \approx 6.4\,\mathrm{k}\Omega. \tag{2.11}$$

In real samples this value is usually smaller and in the range of $G \approx 3e^2/h$ due to impurities in the carbon nanotubes formed already during the growth process or later in the course of subsequent sample fabrication steps (see section 4.1). Examples for ballistic transport measurements in carbon nanotubes can be found in [30,48] where the tube between two contacts acts as a Fabry-Pérot interferometer. In this case the so called *contact resistance* from tube to contacts was low. For contacts with higher opacity where the contact resistance is in the order of several kΩ or more, transport is dominated by Coulomb blockade. This phenomenon which is important for the formation of quantum dots will be explained in the next section.

2.2 Quantum Dots and Coulomb Blockade

In general a quantum dot (QD) is a conductive island in the nanoscale and therefore considered "zero dimensional". It is surrounded by a non-conductive environment. For transport measurements the dot is capacitively coupled to metallic contacts, i.e., source and drain (see figure 2.7). The potential on the dot can be changed via the electric field of an also capacitively coupled gate electrode.
In principle there are many possibilities how a quantum dot can be defined. Either as a small metallic particle, a molecule, a nano constriction or as in our case a segment of an already one dimensional carbon nanotube onto which metallic contact electrodes are deposited to further restrict its dimensions. The metal-CNT interface forms a natural tunnel junction. When the temperature as well as the coupling of source and drain leads to the dot are sufficiently low, an effect called *Coulomb blockade* dominates the transport as we have to take into account electron-electron interaction which was not considered in the previous subsection 2.1.3.

2.2.1 Classical Coulomb Blockade

In classical Coulomb blockade the dot can be considered as a metallic capacitor which can be charged with electrons. To overcome the Coulomb repulsion of the electron that already sits on the dot the so called *charging energy*

$$U = \frac{e^2}{C_\Sigma}$$

has to be provided. C_Σ is the total capacitance of the dot which is a sum of source, drain, gate and additional capacitances ($C_\Sigma = C_s + C_d + C_{gate} + C_{add}$). For the effect of Coulomb blockade two major conditions have to be fulfilled:

1. The system's temperature has to be sufficiently low in order to suppress thermally induced fluctuations of the charge number on the dot. The charging energy has to

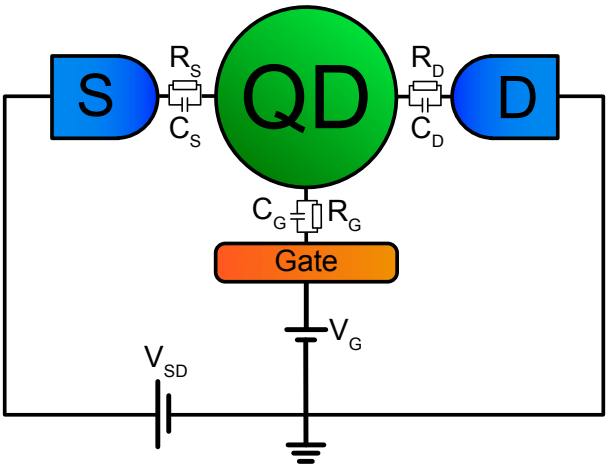

Figure 2.7: A simple sketch of a quantum dot: a conductive island capacitively coupled to source and drain contacts. A gate electrode in the vicinity of the dot can be used to manipulate the electronic states on the dot.

be greater than the thermal energy $E_{th} = k_B T$:

$$\frac{e^2}{C_\Sigma} \gg k_B T.$$

2. The time for charging or discharging the island has to be long enough so that the number of charges is well defined. Considering the typical charging time for a capacitor $\Delta t = R_t C_{s,d}$ and the tunneling resistance $R_t = R_{s,d}$ with the Heisenberg uncertainty relation $\Delta E \Delta t = U \Delta t = (e^2/C_\Sigma) R_t C_{s,d}$, the tunneling resistance R_t has to exceed the quantum of resistance h/e^2:

$$R_t \gg \frac{h}{e^2} = 25.813\,\mathrm{k}\Omega.$$

Many Coulomb blockade experiments are carried out in cryogenic setups to achieve sufficiently low temperatures. The tunnelling resistance can be either tuned by selecting proper materials or by artificially introducing tunneling barriers like oxide layers. In a CNT based quantum dot the coupling is defined by the interface between the metal electrodes and the carbon nanotube.
The situation is illustrated in figure 2.8 (a,b). μ_s and μ_d are the chemical potentials of the source and drain electrode, respectively. Between the electrodes the quantum dot with its discrete energy levels forms. The dot is separated from the leads by tunneling barriers drawn in light red.
The dot becomes conductive when the number of charges on the dot can fluctuate by at least one. This means that the probability to find the dot with N charges has to be equal to the probability that the dot is occupied with $N+1$ charges. Using the grand canonical

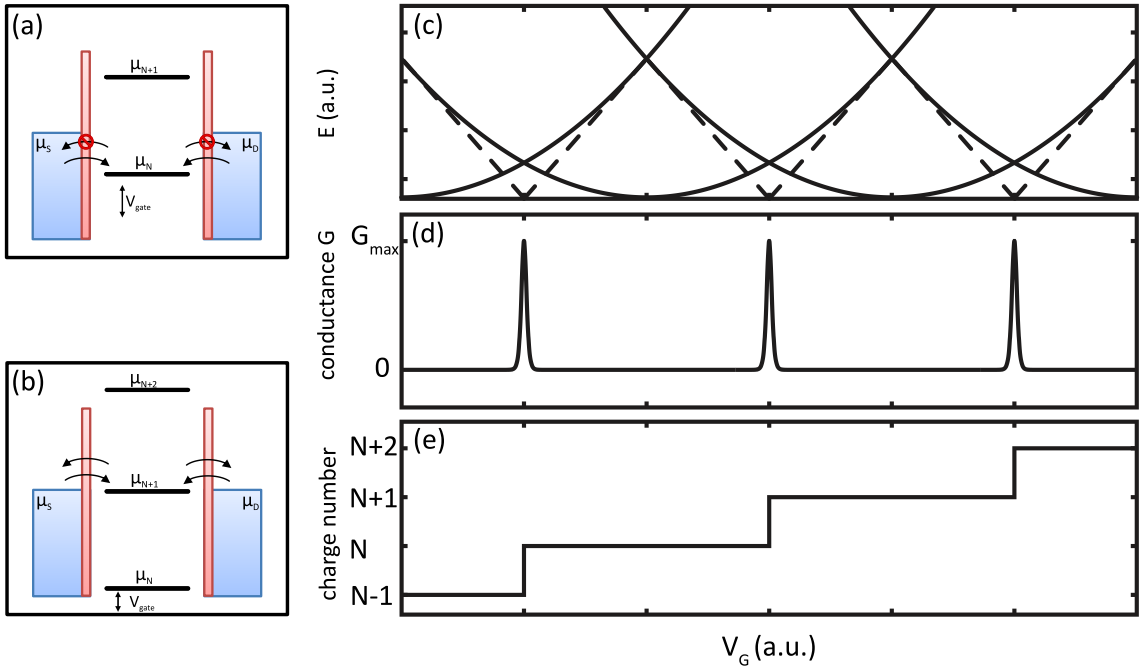

Figure 2.8: Coulomb blockade in a quantum dot at zero bias ($\mu_s = \mu_d$). (a) Energy levels lie below or above the lead potential. Charges can tunnel onto the lower state but are unable to leave the dot, current is blocked. (b) If the potential of the dot μ_N is aligned to the lead potentials, charge fluctuations are possible, the dot becomes conductive. By varying the gate voltage continuously the conductance plot (d) shows equidistant peaks when the dot potential is aligned to the leads. (c) The charging energy with its quadratic dependence of the gate voltage (equation 2.15). If the energy of state N and $N+1$ are equal, two neighboring parabolas intersect and charges are able to fluctuate. (e) Each conductance peak coincides with a step like change by $N = 1$ of the dot's total occupation number.

potential $\Omega(N) = F(N) - \mu N$ the probability to find the dot with N charges is [26, 27]

$$P(N) = \frac{1}{Z} \exp\left(- \frac{\Omega(N)}{k_B T} \right), \tag{2.12}$$

where μ is the chemical potential of the leads connected to the dot, Z is the partition function and $F(N) = E(N) - ST$ the free energy which can be simplified to the ground state energy of the dot $E(N)$ for low temperatures. From the condition $P(N) = P(N+1)$ it follows

$$E(N) - E(N+1) = \mu. \tag{2.13}$$

Therefore the chemical potential of the leads has to be as large as the energy difference between the dot with N and $N+1$ charges in order to enable conductance in the dot.

The chemical potential of the dot with N charges can be defined as the the energy difference of two ground state energies:

$$\mu_{dot} \equiv E(N) - E(N+1). \tag{2.14}$$

Current through the dot can be passed when the condition $\mu = \mu_{dot}$ is fulfilled. In figure 2.8 (a) a situation is illustrated where the chemical potential of the dot lies below the chemical potential of source and drain leads. Charges can tunnel onto the unoccupied state and are trapped there since they can not overcome the energy difference to leave the dot. As shown in figure 2.8 (b), if the chemical potentials match, charges can fluctuate and current can flow.
The ground state energy of the dot can be expressed by the classical charging energy for a capacitor when we assume that the dot is a metallic island with a constant density of states:

$$E(N) = \simeq \frac{1}{C_\Sigma}(eN + C_{gate}V_{gate})^2. \tag{2.15}$$

Using the so called *gate conversion factor*, which is defined as the ratio of gate and total capacitance $\alpha_{gate} \equiv \frac{C_{gate}}{C_\Sigma}$ and the expression for the ground state energy, the condition for single electron tunneling is

$$\mu = e\alpha_{gate}V_{gate} + \frac{e^2}{C_\Sigma}\left(N + \frac{1}{2}\right) = e\alpha_{gate}V_{gate} + U\left(N + \frac{1}{2}\right). \tag{2.16}$$

The potential of the dot can be changed by applying a voltage to the gate electrode. To align the next energy level $\mu_{dot}(N+1)$ to the potential of the leads one has to change the gate voltage by

$$\Delta V_{gate} = \frac{e}{\alpha_{gate}C_\Sigma} = \frac{e}{C_{gate}}. \tag{2.17}$$

A continuous sweep of the gate voltage results in sharp equidistant peaks in conductance with separation ΔV_{gate} (see figure 2.8 (d)). Every time the dot potential is aligned to the lead potentials Coulomb blockade is lifted which results in a conductance peak and the number of charges on the dot increases by $\Delta N = 1$ (see figure 2.8 (e)). The quadratic dependence of the energies of the gate voltage (equation 2.15) are shown in figure 2.8 (c). When two neighboring parabolas intersect, the energy of N is the same as in $N+1$, the tunneling condition is fulfilled. Charges can fluctuate and the dot becomes conductive.

2.2.2 Quantum Coulomb Blockade

In the previous section only a metallic quantum dot with a constant density of states was discussed. Due to the geometry of the sample configuration electrons on the dot

occupy quantized levels which can be resolved in measurements when their energy level spacing is larger than the thermal energy ($\Delta\epsilon \gg k_B T$). For a particle in a box of size L the level spacing $\Delta\epsilon$ depends on the dimensionality of the system. For a quadratic dispersion relation for instance we obtain:

$$\Delta\epsilon = \frac{N}{4}\frac{\hbar^2\pi^2}{mL^2} \quad \text{(1D)}$$

$$\Delta\epsilon = \frac{1}{\pi}\frac{\hbar^2\pi^2}{mL^2} \quad \text{(2D)}$$

$$\Delta\epsilon = \left(\frac{1}{3\pi^2 N}\right)^{\frac{1}{3}}\frac{\hbar^2\pi^2}{mL^2} \quad \text{(3D)}$$

A two dimensional semiconductor quantum dot of a typical size of around 100 nm therefore features a level spacing of around 0.03 meV, which is within the experimental range of a dilution refrigerator where $k_B \cdot 100\,\text{mK} = 8.6\,\mu\text{eV}$. With both charge quantization and quantized energy levels observable in experiment, these quantum dots are often referred to as *artificial atoms* [49].

2.2.3 Coulomb Blockade at Finite Bias

Up to now energy was provided to the dot only by charging it via the gate electrode. In addition also the difference of chemical potentials μ_s and μ_d can be varied by applying a bias voltage to the leads ($eV_{sd} = \mu_s - \mu_d$).
In the classical regime, transport through the dot is only possible when the chemical potential of the dot lies within the interval between μ_s and μ_d, the so called *bias window*.
In a bias spectroscopy measurement both gate voltage and bias voltage are changed continuously while the current through the dot is measured. The data can be visualized in a two dimensional map with two axes V_{gate} and V_{sd} and a color scale as a third axis. Such a map is called *charging* or *stability diagram* and is shown in figure 2.9.
In the white diamond-like shaped areas (figure 2.9: ⋆1) the current is blocked as there is no energy level available within the bias window. This pattern is known as *Coulomb diamonds*. The corresponding energy diagram also marked with ⋆1 illustrates the situation where charges from both leads can tunnel onto the dot but the current is blocked as no charge can leave the dot again. In the areas marked with ⋆2 one state lies within the bias window, the blockade is lifted and current can flow. When V_{sd} is increased even further, the next state would enter the bias window leading to a step-ike increase of current. The energy which has to be provided is the classical charging energy e^2/C_Σ.
Tunneling spectroscopy in the quantum regime can reveal additional energy levels. Here the discrete levels on the dot as seen before, as well as excitations of these levels (as in section 2.2.2) can be observed. The area in figure 2.9 marked with ⋆3 and the corresponding energy diagram illustrate the situation where an excited state μ_N^* (red) enters the bias

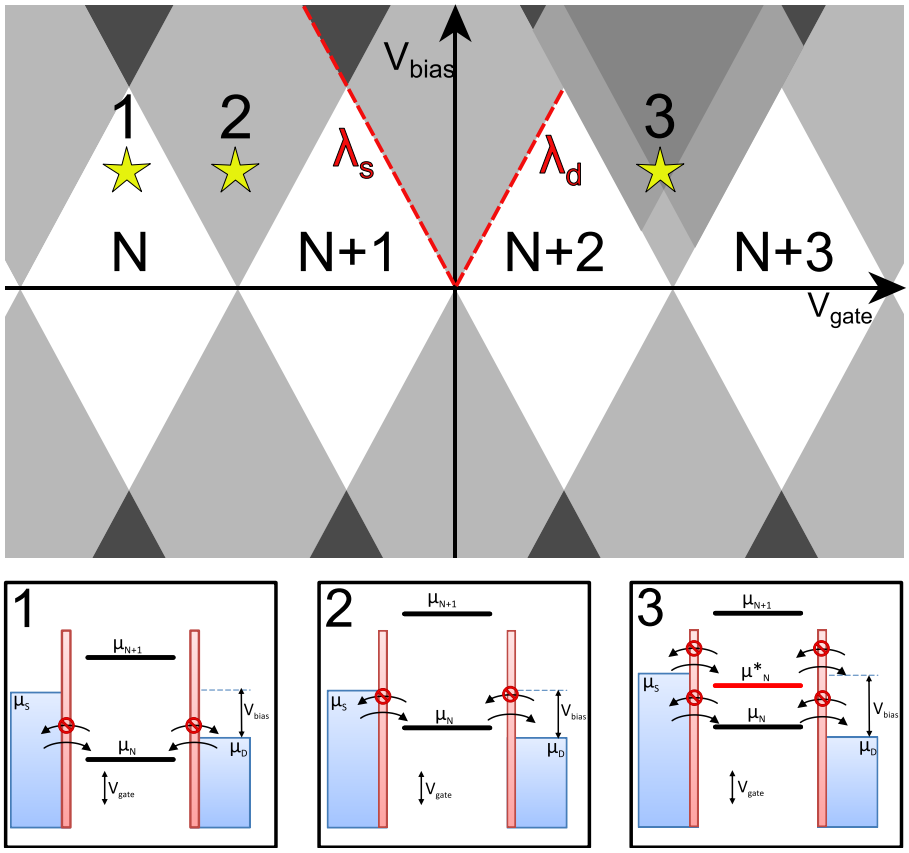

Figure 2.9: Stability diagram of a quantum dot showing the so called *Coulomb diamond* pattern. (1) No accessible state within the bias window: current is blocked. (2) Sequential tunneling: one available state enters the bias window and enables transport. (3) An additional excited state opens an extra transport channel which shows as a step up in current.

window. When $\mu_d > \mu_N, \mu_N^* > \mu_s$ two energy levels contribute to the transport leading to a step up in current.

Depending on the origin of the current steps in the charging diagram, the energy difference is either called *addition energy* for the first type of current changes and *excitation energy* when excited states are involved.

The red dashed single electron tunneling (SET) lines labeled λ_s and λ_d in figure 2.9 define the edges of the Coulomb diamonds, they are called *source-* and *drain lines*. Along these lines the chemical potential of the source (drain) contact μ_s (μ_d) is aligned to the dot potential μ_{dot}.

When we assume a constant drain potential ($\mu_d = const.$) the dot potential along the drain line can be written according to equation 2.16 as

$$\mu_{dot} = \mu_d = E_N + \left(N + \frac{1}{2}\right)\frac{e^2}{C_\Sigma} + e(\alpha_s V_{sd} + \alpha_{gate} V_{gate}) = const. \tag{2.18}$$

In a similar way the source line can be expressed as

$$\mu_{dot} = \mu_s = E_N + \left(N + \frac{1}{2}\right)\frac{e^2}{C_\Sigma} + e((1-\alpha_s)V_{sd} + \alpha_{gate}V_{gate}) = const. \tag{2.19}$$

introducing additional conversion factors for source (α_s) and drain (α_d) contacts:

$$\alpha_s \equiv \frac{C_s}{C_\Sigma} \qquad \alpha_d \equiv \frac{C_d}{C_\Sigma} \tag{2.20}$$

The slopes of the two SET lines are determined the following way:

$$\lambda_s \equiv \frac{dV_{gate}}{dV_{sd}} = \frac{1-\alpha_s}{\alpha_{gate}} = \frac{C_\Sigma - C_s}{C_{gate}} \tag{2.21}$$

$$\lambda_d \equiv \frac{dV_{gate}}{dV_{sd}} = -\frac{\alpha_s}{\alpha_{gate}} = -\frac{C_s}{C_{gate}} \tag{2.22}$$

From these slopes it is therefore possible to determine the gate conversion factor α_{gate} as:

$$\alpha_{gate} = \frac{1}{|\lambda_s| + |\lambda_d|}. \tag{2.23}$$

2.2.4 Carbon Nanotube Based Quantum Dots

In this work we are investigating carbon nanotube based quantum dots. While in the previous sections quantum dots in general were discussed, CNT based systems show additional features attributed to their special structure. Depending on the transparency of the contact leads to the tube, we can find different transport regimes in such devices. Unlike in semiconductor based (2DEG) systems where the transparency can be tuned for instance by a split gate, in a CNT device transparency is set by the metal/-carbon interface and can also vary with the gate voltage. In semiconducting tubes it is often observed that the transparency is different in the electron and hole side, this was observed for instance in [50] where figure 2.10 was taken from. Also more recent experiments with ultra clean carbon nanotubes impressively show this behavior [51, 52]. Actual measurement data taken from [50] is presented in figure 2.10. Three different transport regimes can be discriminated. In panel (a) the transparency is high with the conductance in the order of $1\,e^2/h \lesssim G \lesssim 2\,e^2/h$. In this so called *Fabry-Pérot regime* the nanotube behaves as an electron wave guide between the two metal contacts (see section 2.1.3). When the CNT to contact interface is more opaque an intermediate transport regime can be observed. As illustrated in panel (b) the conductance here is $G \lesssim 1.5\,e^2/h$ and several signatures of the *Kondo effect* manifest in the diagram. This regime therefore is often called the *Kondo regime*. More details about the Kondo

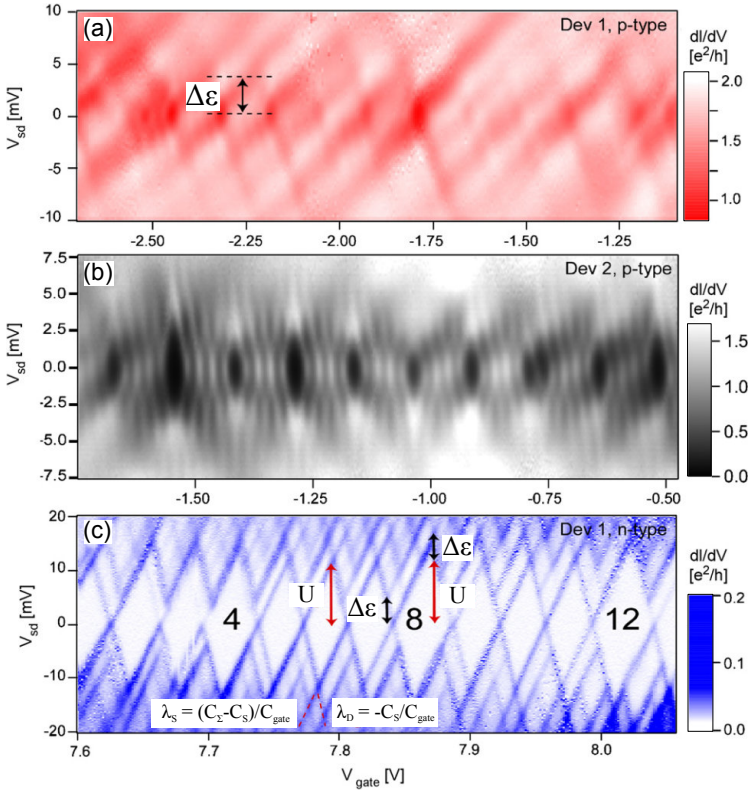

Figure 2.10: Conductance vs gate and bias voltage (stability diagrams) for different transport regimes in a carbon nanotube device with two metallic contacts and backgate (taken from [50]). (a) For highly transparent contacts the tube acts as an electron waveguide with cavity length $\Delta\varepsilon$ and interference patterns can be observed. In the intermediate coupling regime (b), higher order processes like the Kondo effect can play a role, this regime is therefore often called the Kondo regime. (c) Single electron tunneling in the low transparency regime with several excited states visible in the diagram. From this diagram important transport parameters (see equation 2.24) can be extracted. Note that panel (a) and (c) show measurements of the same device but different gate voltages, the coupling of a CNT to the leads can be strongly gate dependent.

effect in carbon nanotubes and the other transport regimes can be found for instance in [53–55].

At low contact transparencies ($G \lesssim 1.5\,e^2/h$) like in panel (c), one can find the so called *closed regime* which is governed by the effect of Coulomb blockade and single electrons can tunnel sequentially through the dot. Such a device is often called single electron transistor (SET), the effect of Coulomb blockade has been already discussed in the previous sections.

The Coulomb diamond pattern in the measurement data from the SET regime in figure 2.10 reflects the shell filling on the dot. Because of both K,K' and spin degeneracy (up, down) one can observe a fourfold pattern in the transport data (see section 2.1.3) which allows us to extract important transport parameters for the device. As described in the

model of Oreg et al. [56–58] one can deduce five parameters from a typical charging diagram: the charging energy U, the quantum energy level separation $\Delta\varepsilon$, the sub band mismatch δ, the exchange energy J, and the excess Coulomb energy dU. A schematic visualization of these parameters can be found in figure 2.11 (adapted from [57]). $\Delta\varepsilon$ is simply the spacing between the quantized energy levels on the two linear branches of the CNT band structure. The sub band mismatch δ accounts for a slight difference between the two branches (bands). J corresponds to the energy difference between a parallel and antiparallel spin configuration in different orbitals. dU is the difference between the energy of two different spins in one orbital and two different spins distributed over two orbital states.

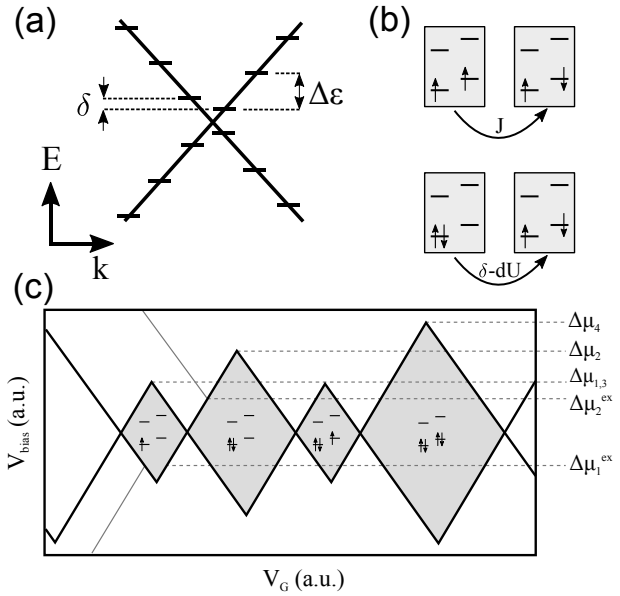

Figure 2.11: Shell filling for metallic carbon nanotube with two contact electrodes (adapted from [57]). (a) Discrete energy levels with separation $\Delta\varepsilon$ within the two branches of the dispersion relation due to the restriction of the CNT length. The levels on the two branches can be shifted slightly by the subband mismatch δ. (b) The exchange coupling J is the difference between two spins with same orientation and an antiparallel configuration on two different energy levels, while the excess Coulomb energy dU is the extra energy associated with placing two electrons to the same energy level. (c) Stability diagram for a CNT quantum dot featuring fourfold symmetry, the size of the Coulomb diamonds varies in size: small, medium, small and a large diamond in a regular way. The energy scales which can be extracted from such a diagram are labeled $\Delta\mu_i$ with charge number i, for $i = 1, 2$ also excited states $\Delta\mu_i^{ex}$ are shown.

From an ideal charging diagram as shown in panel (c) of figure 2.11 the following values can be extracted:

$$\begin{aligned} \Delta\mu_1 &= U + dU + J, & \Delta\mu_2 &= U + \delta - dU, \\ \Delta\mu_3 &= \Delta\mu_1, & \Delta\mu_4 &= U + \Delta\varepsilon - \delta - dU, \\ \Delta\mu_1^{ex} &= \delta, & \Delta\mu_2^{ex} &= \delta - J - dU. \end{aligned} \tag{2.24}$$

$\Delta\mu_i, i \in 1,2,3,4$ are the addition energies for the different charge numbers as indicated in figure 2.11 (c). Energies marked with *ex* indicate that there is an excited state involved in the transport through this channel.

2.3 Noise and Noise Measurements

Noise usually describes spontaneous and random fluctuations of a physical quantity in time around a certain mean value [1]. For electrical systems current deviations from the average current value $\Delta I(t) = I(t) - \langle I \rangle$ are usually referred to as *current noise*.
In all previous considerations only transport measurements were taken into account, i.e., voltage, current and conductance measurements. In mesoscopic devices however current is described by the charge q times the time derivative of the number of charge carriers on the leads ($I(t) = q\frac{dN}{dt}$). As the number of carriers is based on tunneling events (see sections 2.1.3, 2.2) which are statistic processes, also the fluctuation of current is such a process.
In standard transport experiments at low temperatures one usually tries to keep the level of noise in the experimental setup as low as possible as fluctuations in current can for instance compromise the detection of weak features in a conductance measurement of CNTs. Employing extensive filtering to the low temperature measurement setup (cryostat) helps to screen the sample from radiation coming from the outside world, e.g., radio/TV signals or signals in the higher MHz or GHz range like mobile phones or other wireless networks.
However noise can not only be the unwanted signals we want to remove by filtering. Out of equilibrium noise (shot noise) can also provide an additional source of information which can give us more insight in the transport mechanisms involved in our measurements [7].
A combination of conductance and shot noise studies can for instance reveal details about the charge of the carriers involved in transport and about their statistics [2–6].

To characterize current fluctuations $\Delta I(t) = I(t) - \langle I \rangle$ one can introduce a current-current correlation function [3, 4, 59]

$$C(t) \equiv \langle \Delta I(t + t_0) \Delta I(t_0) \rangle \tag{2.25}$$

and the Fourier transformation of this function

$$S_I = \int_{-\infty}^{+\infty} dt\, e^{i\omega t} C(t) = \int_{-\infty}^{+\infty} dt\, e^{i\omega t} \langle \Delta I(t + t_0) \Delta I(t_0) \rangle, \tag{2.26}$$

the *power spectral density* (PSD) which is the noise power per units of frequency. For the classical case the correlation function is symmetric in time $C(t) = C(-t)$. Therefore the PSD is symmetric in frequency $S_I(\omega) = S_I(-\omega)$, which is true for low frequency noise

measurements away from the quantum limit $\hbar\omega \gg k_B T$. The quantity which can be detected my means of standard low frequency noise measurements is the symmetrized spectrum

$$S_I(\omega) = S_I(\omega) + S_I(-\omega) = 2\int_{-\infty}^{+\infty} dt\, e^{i\omega t} C(t). \tag{2.27}$$

The presence of noise in mesoscopic devices can be caused by several mechanisms. The relation between thermal energy $k_B T$, the energy provided by the bias voltage eV and the photon energy $\hbar\omega$ depending on the frequency where the noise is measured determine which noise mechanism is dominant. Various sources of noise are discussed in the following section.

2.3.1 Sources of Noise

In a typical experimental setup one has to deal with different mechanisms which produce noise, i.e., random fluctuations of a certain value around its mean value.

Thermal Noise

As already mentioned in section 2.2, at finite temperature thermal fluctuations in the number of charge carriers on the device lead to voltage and current fluctuations in the system in equilibrium ($V_{bias} = 0$). This type of noise was first reported experimentally by J. B. Johnson [60], theoretical work on this topic was done by H. Nyquist [61]. Thermal noise is therefore also called *Nyquist-Johnson* noise, it dominates in a configuration where $k_B T \gg eV, \hbar\omega$. Thermal noise is frequency independent (*white noise*) up to the quantum limit $\omega = k_B T/\hbar$ (see section 2.3.1). The amplitude of thermal noise is directly proportional to the sample or system conductance G and is given by the *Nyquist-Johnson formula*:

$$S_I = 4k_B T G. \tag{2.28}$$

Since this noise amplitude is directly proportional to the temperature and the conductance of the sample it is clear that there is no additional information besides what is already known from transport measurements. However thermal noise can be employed for calibration of a noise amplifier system, to compare the expected thermal noise from a known resistor at a known temperature with a measured power spectral density.

1/f Noise

Slow changes in the resistance of a device cause current fluctuations in the low frequency regime. This kind of noise is present in almost every material. Its amplitude is proportional to the square of the injected current but decays inversely with the frequency. *1/f - noise* is strongly suppressed for higher frequencies (several kHz) and does not play a

role in our measurements as we chose frequencies in in the MHz regime for those reasons. An extensive study for all kinds of fluctuations in conductors can be found in [62].

Shot Noise

When current is passed through a conductor, i.e., the system is not in equilibrium and $V_{bias} \neq 0$, charge carriers are transmitted or reflected randomly which results in fluctuations of this current (*shot noise*). This phenomenon is a direct consequence of charge quantization and was first described by W. Schottky [1]. Like thermal noise, shot noise is white. Shot noise is the dominant source of noise for $eV \gg k_B T, \hbar\omega$.
An incident beam of charge quanta, partitioned by a barrier into a transmitted and a reflected beam can be described with a standard binomial distribution

$$P = \binom{n}{n_\Gamma} n_\Gamma \Gamma^{n_\Gamma} (1-\Gamma)^{n-n_\Gamma}, \tag{2.29}$$

the average number of transmitted particles n_Γ in a stream of n charge quanta with transmission probability Γ is given by

$$\langle n_\Gamma \rangle = n\Gamma. \tag{2.30}$$

Shot noise is also known as *partition noise*.
The variance of the number of transmitted particles is given by

$$\begin{aligned} \langle \Delta n_\Gamma^2 \rangle &= \langle n_\Gamma^2 \rangle - \langle n_\Gamma \rangle^2 = n\Gamma(1-\Gamma) \\ &= \langle n_\Gamma \rangle (1-\Gamma). \end{aligned} \tag{2.31}$$

Since the average current $\langle I \rangle = q\frac{d}{dt}\langle n_\Gamma \rangle$ with the particle charge q and the power spectral density S_I is proportional to the variance of the current ($S_I \propto \langle \Delta I \rangle^2$), shot noise can be expressed by the relation [1, 4, 62]:

$$S_I = 2e\langle I \rangle (1-\Gamma), \tag{2.32}$$

where e is the electron charge, $\langle I \rangle$ the average current and Γ the transmission probability of a tunneling barrier.
In the limit of $\Gamma \to 0$, charge carriers are entirely uncorrelated, and obey a Poissonian distribution (*Poissonian limit*). For this scenario equation 2.32 simplifies to the well known *Schottky formula* [1]:

$$S_I = 2e\langle I \rangle. \tag{2.33}$$

When correlations between the charge carriers are involved, shot noise can be suppressed or enhanced with respect to the Poissonian limit (sub or super Poissonian noise). To account for deviations from this limit the *Fano factor*

$$F = \frac{S_I}{2e\langle I \rangle} \tag{2.34}$$

is used which was first introduced by Ugo Fano in 1947 [63]. In a quantum point contact (QPC) [64] for instance, where $G = 2e^2/h$ and therefore $\Gamma = 1$, transport is noiseless as a consequence of the Pauli exclusion principle. This follows directly from equation 2.32 [11, 12]. Another example is noise suppression in a quantum dot (QD) when transport is dominated by Coulomb blockade in a double barrier system [13, 65–69]. In such a scenario noise is suppressed by a factor of two, leading to $F = \frac{1}{2}$, whereas $F = \frac{1}{3}$ in disordered wires [14, 15] and $F = \frac{1}{4}$ in open chaotic cavities [4, 16].
On the other hand scenarios like blocked channels in the conductor which release more than one charge quantum in bunches or in an avalanche-like process can result in *super Poissonian* noise [18] where F > 1.0. Such a blocking of channels can for instance be caused by Franck-Condon blockade which will be discussed later in section 2.4 and in chapter 5.
Shot noise can also give insight into the nature of charge carriers, in superconductor-hybrid systems for instance noise can be twice as large when charge is carried by Cooper pairs with $q = 2e$ [10]. An extensive review of noise in mesoscopic conductors can be found in [4] or in [3].

Quantum Noise

In the high frequency limit when $\hbar\omega \gg k_B T$ the noise spectrum is not symmetric anymore: $S(\omega) \neq S(-\omega)$. This means that the emitted noise is different from the absorbed noise. Zero point fluctuations (ZEP) in the device are responsible for this effect. More complicated detection schemes than used in this work are necessary to detect this kind of fluctuations [70,71]. As quantum noise does not play a role in our measurements since we work at $f \sim 2\,\mathrm{MHz}$, this topic should only be mentioned briefly, reference [72] gives an introduction to quantum noise. For our setup at $T = 25\,\mathrm{mK}$ the threshold frequency for quantum noise would be $f \gtrsim 400\,\mathrm{MHz}$.

2.3.2 Noise Measurement Techniques

In this section several methods for shot noise measurements will be discussed. Depending on the setup, the sample, and also on the physical effects one wants to investigate, the best technique for shot noise detection can vary.

Cross-Correlation Technique (Low Frequencies)

Usually current fluctuations in a sample $S_I = \langle \Delta I_S^2 \rangle$ is the interesting quantity in shot noise experiments as is converts directly to the important Fano factor (equation 2.34). It is however easier to measure voltage fluctuations $S_V = \langle \Delta V_S^2 \rangle$ across the sample using low noise voltage amplifiers and feed the signal into a spectrum analyzer. The conversion voltage to current power spectral density is then performed via the differential resistance of the sample $R_S = dV/dI$: $\langle \Delta V_S^2 \rangle = (R_S)^2 \langle \Delta I_S^2 \rangle$. Such a setup is shown in figure 2.12.

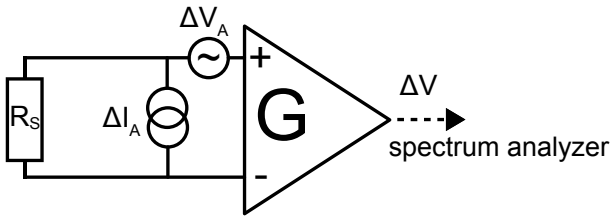

Figure 2.12: A simple noise measurement setup using a single amplifier: the current noise ΔI_A, generated by the resistor R_S is detected as voltage fluctuations ΔV_A across the resistor and amplified by a voltage amplifier resulting in an output voltage ΔV.

Together with the current and voltage noise generated at the input of the amplifier $\langle \Delta I_A^2 \rangle$ and $\langle \Delta V_A^2 \rangle$ the measured power spectral density of the total signal in a certain bandwidth Δf can be expressed as:

$$\langle \Delta V^2 \rangle = \langle \Delta V_S^2 \rangle + (R_S + R_L)^2 \langle \Delta I_A^2 \rangle + 4 R_L k_B T_L \Delta f \tag{2.35}$$

with R_L being the resistance of the leads, T_L the lead temperature.
To precisely determine the noise generated in the sample one has to exactly know all the other quantities in equation 2.35. The temperature of the leads for instance is not easy to determine. Also with increasing integration time the stability of the amplifiers regarding their noise output becomes more and more important.
To get rid of all voltage noise arising from the involved voltage amplifiers a setup as shown in figure 2.13 can be considered [3,73].

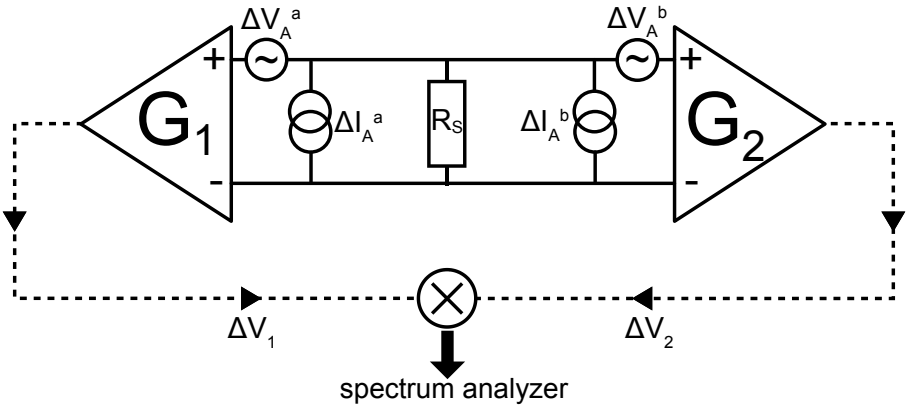

Figure 2.13: Two independent amplifiers are connected in parallel to the same source of noise R_S. After the amplification stage two voltage signals ΔV_1 and ΔV_2 are fed into a spectrum analyzer where the cross correlation of both signals is calculated. This method results in a much cleaner signal compared to a single amplifier setup as intrinsic noise from the amplifiers and the leads which is different in the two signals is canceled out.

Here two independent amplifiers are connected in parallel to the same source of noise. The voltage drop measured from both amplifiers is again fed into a two channel spec-

trum analyzer which is capable of multiplying the two signals and calculating a cross-correlated spectrum:

$$\langle \Delta V_a \Delta V_b \rangle = \langle \Delta V_S^2 \rangle + R_S (R_S + R_L^a)^2 \langle \Delta I_a^2 \rangle + R_S (R_S + R_L^b)^2 \langle \Delta I_b^2 \rangle. \tag{2.36}$$

Now the voltage noise from the amplifiers as well as the thermal noise coming from the leads is canceled out, leaving only the current noise from both amplifiers and the lead resistances. Current noise from an amplifier does usually contain no $1/f$-noise [3]. Therefore this type of measurement is suitable for lower frequencies.
One limiting factor of this method is the usable bandwidth in the setup. The combination of cable capacitances, filters, resistors, input capacitances of the amplifiers etc. sets an upper limit of $f_{max} = \frac{1}{2\pi RC}$ for the measurement frequency which usually lies in the several 100 kHz range.

Resonant Scheme (MHz Frequencies)

For measurements in the MHz range a modified version of the aforementioned setup can be used as it is done in references [8, 9, 11, 74] or recently in [10, 71, 75–77]. The cited setups are slightly different but have one thing in common: an inductance in parallel to the coaxial capacitance of the measurement line forms an RLC circuit together with the sample resistance. The impedance of the RLC circuit at resonance frequency converts the current noise from the sample to a voltage noise which can be measured as the amplitude of a resonance peak. An example for such a setup is shown in figure 2.14.

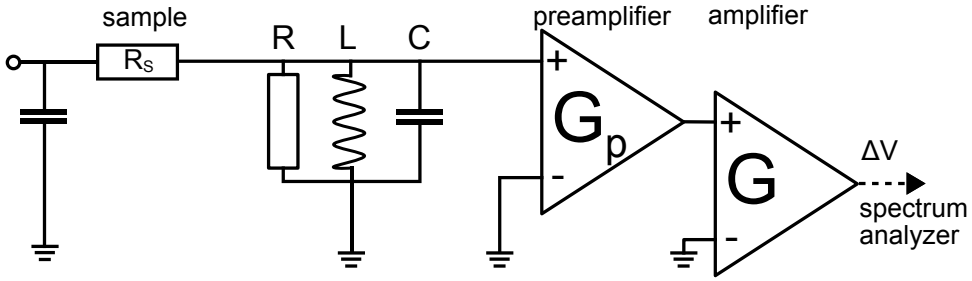

Figure 2.14: Resonant scheme for noise detection: an RLC circuit is connected to the source of noise, confining the otherwise white noise to a bell shaped resonance curve determined by the components of the RLC circuit. The resonance frequency where the signal is maximal is given by $f_{res} = \frac{1}{2\pi\sqrt{LC}}$. The impedance of the RLC circuit at f_{res} converts current noise S_I to voltage noise S_V which can be amplified by a voltage amplifier. For an even better signal-to-noise ratio and measurement bandwidth, the amplification chain can be split into a preamplifier sitting close to the sample and a second one outside the cryostat.

In this case (as in [8, 74]) the amplification chain is split into a preamplifier (cryogenic FET) at low temperatures and a second amplifier at room temperature. Even though

the noise characteristics of cryogenic FETs are not necessarily better than for room temperature amplifiers, such systems have the advantage that the distance between the first amplification stage to the sample is much smaller which increases the bandwidth for the measurement [3].
Systems like these can also be combined again with a cross-correlation setup by adding a second amplifier chain to further increase the resolution. If the experiment is based on measuring cross-correlations between different terminals as in [78,79], two independent amplification circuits are absolutely necessary.

2.4 Franck-Condon Blockade

Franck-Condon blockade is a common phenomenon often observed in suspended carbon nanotubes [80] and other systems featuring electronic states and additionally vibrational degrees of freedom [81]. Since Franck-Condon blockade gives rise to slow transport channels in a quantum dot device, it is often associated with super Poissonian noise [82, 83]. Later in chapter 5 we will employ this model for the analysis of our measurement data. Franck-Condon blockade leads to a suppression of current at lower bias voltages in transport. The Franck-Condon principle originates from optical spectroscopy where photons couple to vibrational modes in molecules but can also be used as a generic model for electron-phonon coupling. First discovered by James Franck [84] and later described theoretically by Edward Condon [85], the Franck-Condon principle relies on the assumption that electronic transitions are several orders of magnitude faster than movements of the nuclei in the molecule. For the electron the nuclear position is the same before and after an electronic transition. As shown figure 2.15 the Franck-Condon principle can be illustrated by two parabolic potentials which represent the effective nuclear potentials of two consecutive electronic states N and $N+1$. Electron-phonon coupling in the system leads to a lateral displacement of the nuclei potentials. The dimensionless electron phonon-coupling constant g is defined as

$$g = \frac{1}{2}\left(\frac{x}{x_0}\right)^2 \tag{2.37}$$

where x is the lateral displacement of the nucleus after an electronic transition with respect to its position before the transition, x_0 is called the *oscillator length*. Considering a suspended carbon nanotube, the oscillator length can be defined as

$$x_o = \sqrt{\frac{\hbar}{nm\omega}} \tag{2.38}$$

with the frequency

$$\omega = \frac{\pi}{L}\sqrt{\frac{AY}{\rho_m}}, \tag{2.39}$$

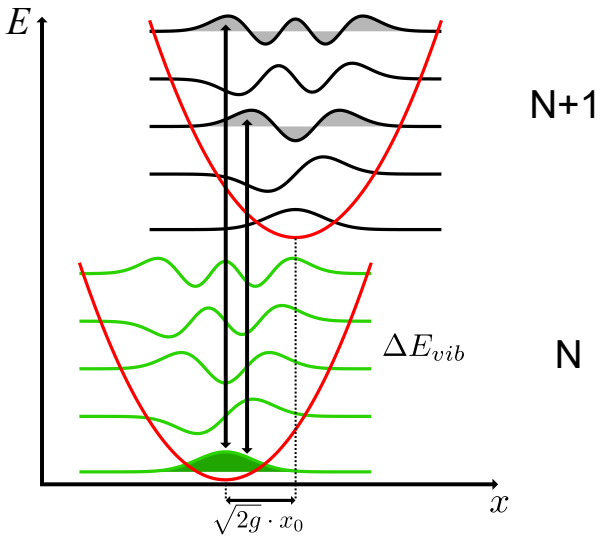

Figure 2.15: Visualization of the Franck-Condon principle: vibrational modes of a quantum harmonic oscillator with energy separation $\Delta E_{vib} = \hbar\omega$ give rise to vibron assisted transition from one electronic level to another. The transition probability is proportional to the square integral of the overlapping wave functions leading to multiple steps in current separated by ΔE_{vib}. The lateral displacement of the two parabolas illustrates the electron-phonon coupling. For strong coupling the lower wave functions show no overlap anymore causing a decrease of current at low bias, the Franck-Condon blockade.

where Y is the Young's modulus, ρ_m the mass density, L the length and $A = \pi R^2$ the area of the cross section of the tube. The magnitude of g determines the structure of the vibrational sidebands in the transport. For $g << 1$ no sidebands are visible, clear sidebands appear for $g \sim 1$. For a large electron-phonon coupling $g >> 1$, current is suppressed at low bias [86].
In figure 2.15 transitions from the N ground state to the $N+1$ second and fourth excited state are the most probable as the overlap of these wave functions is the largest. The transition from the first vibron in N to the first vibron in $N+1$ is suppressed since the overlap of these two wave functions is small.
When the bias voltage applied to the dot matches an integer multiple of the vibron energy $E_{vib} = \hbar\omega$, conductance through the dot is enhanced leading to an equidistant spectrum of replicas of excitation lines as seen in [80, 87, 88].
In current versus bias voltage characteristics, the enhancement of conductance manifests as steps in the current. While for low damping of the oscillator the step heights are constant in energy (bias voltage), for strong relaxation the step heights are given by a Poissonian distribution [87, 88]

$$P_n = \frac{e^{-g} g^n}{n!} \tag{2.40}$$

where n is the number of the excitation line and g again the electron-phonon coupling. The larger g becomes, the more pronounced is the effect of Franck-Condon blockade. When the system is in the vibrational ground state, a long waiting time is required before the electron can tunnel out of this state. Once the electron tunnels out, the higher excited states with smaller relaxation time become available which leads to a series of fast tunneling events where many electrons tunnel in an avalanche-like process followed again by a longer waiting time. Due to a large number of electrons per avalanche the Fano factor in those regions can become much larger as opposed to a situation where electrons are transferred one by one where the noise is purely sub Poissonian [83].

2.5 Theoretical Model

In this section we want to give a description of the theoretical model underlying the numerical simulations shown in section 5.3. At the time being a fully analytical model for our problem was not yet available, for that reason numerical calculations of the density matrix are supposed to give a first approximation. The model as well as the code was developed and provided by Michael Niklas from the chair of Prof. Milena Grifoni, it is implemented in Matlab[2].
The theory group is using code based on previous calculations of phonon assisted features in carbon nanotubes [89], where additionally full counting statistics (FCS) in the style of reference [90] was enclosed. The following sections are based on notes by Michael Niklas [91]. The code calculates current as well as the noise in the system including phonon modes (longitudinal stretching modes) and coupling asymmetry for left and right lead as well as orbital asymmetry. The model is able to determine the population on the dot by calculating a reduced density matrix $\rho = \mathrm{tr}_B(\rho^{tot})$, independent from the bath B (leads) for our system.

2.5.1 Calculating the Density Matrix

The goal was to find an equation for the time evolution of the reduced density matrix ρ:

$$\dot{\rho} = \mathcal{L}\rho. \tag{2.41}$$

$\mathcal{L}$ is a Superoperator which we call Liouvillian. The total model Hamiltonian for our system $H = H_S + H_B + H_V$ consists of a system, a bath (= leads) and an interaction part. We start with the following von Neumann equation in the interaction picture for the total density matrix

$$\dot{\rho}_I^{tot}(t) = -\frac{i}{\hbar}\Big[H_{V,I}(t), \rho_I^{tot}(t)\Big] \tag{2.42}$$

[2] http://www.mathworks.com/products/matlab/

which is integrated formally and again inserted in equation 2.42, giving

$$\dot{\rho}_I^{tot}(t) = -\frac{i}{\hbar}\Big[H_{V,I}(t), \rho_I^{tot}(0)\Big] - \frac{1}{\hbar^2}\int_o^t \mathrm{d}t' \Big[H_{V,I}(t), \Big[H_{V,I}(t'), \rho_I^{tot}(t')\Big]\Big]. \tag{2.43}$$

The reduced density matrix, which is independent from the leads, can be obtained by tracing this equation over the bath B according to $\rho = \mathrm{tr}_B(\rho^{tot})$:

$$\dot{\rho}_I(t) = -\frac{i}{\hbar}\mathrm{tr}_B\Big[H_{V,I}(t), \rho_I^{tot}(0)\Big] - \frac{1}{\hbar^2}\int_o^t \mathrm{d}t'\ \mathrm{tr}_B\Big[H_{V,I}(t), \Big[H_{V,I}(t'), \rho_I^{tot}(t')\Big]\Big]. \tag{2.44}$$

In the limit of weak coupling the total density matrix can be factorized as $\rho^{tot}(t) = \rho(t) \otimes \rho_B$ (Born-Approximation). The part for the leads in equilibrium ρ_B can be considered constant as the population of the leads is assumed thermal. The first term in equation 2.44 vanishes since $\mathrm{tr}_B\Big[H_{V,I}(t)\rho_B\Big] = 0$. Integrating over $s = t - t'$ then leads to

$$\dot{\rho}_I(t) = -\frac{1}{\hbar^2}\int_o^t \mathrm{d}s\ \mathrm{tr}_B\Big[H_{V,I}(t), \Big[H_{V,I}(t-s), \rho_I(t-s) \otimes \rho_B\Big]\Big]. \tag{2.45}$$

Using the Markov approximation allows us to replace $\rho(t-s)$ by $\rho(t)$ with integration to infinity and a transformation back to the Schrödinger picture gives the master equation

$$\dot{\rho} = -\frac{i}{\hbar}[H_S, \rho] - \frac{1}{\hbar^2}\int_0^\infty \mathrm{d}s\ \mathrm{tr}_B\Big[H_V, \Big[H_{V,I}, \rho^{tot}\Big]\Big]. \tag{2.46}$$

For the interaction part of the Hamiltonian a standard tunneling term from the system to the leads and vice versa

$$H_V = \sum_{k,\alpha} V_{k,\alpha} c_{k,\alpha}^\dagger d_\alpha + \mathrm{h.c.} \tag{2.47}$$

was chosen, where $c_{k,\alpha}^{(\dagger)}$ annihilates (creates) an electron in lead α and mode k and $d_\alpha^{(\dagger)}$ annihilates (creates) an electron in the system. In the eigenbasis of the system where $H_S|m\rangle = \epsilon_m|m\rangle$ the trace over B in equation 2.46 and integration over time using the Dirac identity results in the terms

$$\sum_k |V_{k,\alpha}|^2 f_\alpha^\pm(\epsilon_{k,\alpha}) \int_{-\infty}^\infty \mathrm{d}s\ e^{\frac{i}{\hbar}(\omega \mp \epsilon_{k,\alpha})s} = \underbrace{2\pi \sum_k |V_{k,\alpha}|^2 \delta(\omega \mp \epsilon_{k,\alpha})}_{=\Gamma_\alpha} f_\alpha^\pm(\omega) \tag{2.48}$$

where ω are the energy differences in the system. This gives us the tunneling rates Γ_α. The master equation can be written in the Lindblad form as

$$\dot{\rho} = -\frac{i}{\hbar} + \sum_\alpha \sum_{mn} \Gamma_\alpha f_\alpha^+(\omega_{mn}) \mathcal{D}_{mn}(d_\alpha^\dagger)\rho + \Gamma_\alpha f_\alpha^-(\omega_{mn}) \mathcal{D}_{mn}(d_\alpha)\rho \tag{2.49}$$

with $\omega_{mn} = \epsilon_m - \epsilon_n$ and the Lindblad operator

$$\mathcal{D}_{mn}(X)\rho = |m\rangle X_{mn}\rho_{nn}X^{\dagger}_{nm}\langle m| - \frac{1}{2}\left\{X_{mn}X^{\dagger}_{nm}, \rho\right\} \tag{2.50}$$

where $X_{mn} = \langle m|X|n\rangle$.
The Liouville superoperator $\mathcal{L}$ from equation 2.41 acts on the density matrix in the following way:

$$\dot{\rho}_{mn} = \sum_{kl} \mathcal{L}_{mn,kl}\rho_{kl}. \tag{2.51}$$

$\mathcal{L}$ is therefore a four dimensional object. To simplify the problem it is convenient to work in the Liouville space. This means that the density matrix is rewritten into a vector which makes the Liouvillian a two dimensional matrix.
Taking a closer look at equation 2.49 reveals that it contains the matrix elements of $\mathcal{L}$. The diagonal part describes all ways of leaving the corresponding level while the off diagonal part describes the ways to enter it. In simple words, the Liouvillian contains all tunneling rates on and off a level on the quantum dot. In Liouville space a stationary solution for the density matrix vector is a right eigenvector of $\mathcal{L}$ to the eigenvalue 0. A solution can therefore be obtained by calculating the kernel of the Liouvillian

$$\rho = \ker(\mathcal{L}). \tag{2.52}$$

The problem can be solved numerically by means of matrix calculations, which can be performed in Matlab. From a given phononic excitation energy $\Delta E_{ph} = \hbar\omega_{ph}$, which we know from our experimental data, the code calculates the number of degenerate states on the dot and the corresponding configuration of phononic modes according to [89]. The tunneling rates for two different charge states on a CNT $\Gamma^1_s = \Gamma$, $\Gamma^1_d = b\Gamma$, $\Gamma^2_s = a\Gamma$ and $\Gamma^2_d = ba\Gamma$ are computed according to reference [89], where a is the coupling asymmetry and b the channel asymmetry. In the calculation of Γ the electron phonon coupling parameter λ enters. The transition rates Γ directly enter the Liouvillian. To account for the observation that higher excitations are not or only faintly visible in the experiment, the simulation also introduces artificial dissipation for phonons and electrons separately. Relaxation times τ_e and τ_{ph} for electrons and phonons, which restrict the number of accessible states by allowing them to relax to the bath, are included into the dissipative part of the Liouvillian $\mathcal{L}$. As a result the density matrix describing the populations on the dot is obtained.

2.5.2 Full Counting Statistics

So far only the populations were calculated. To get access to current and noise data a counting variable χ which increases or decreases by one at each tunneling event is introduced. It is then possible to integrate this counting variable χ into our reduced

density matrix ρ and replace

$$\rho \to \rho_\chi = \mathrm{tr}_B\left[e^{i\chi N}\rho^{tot}\right]. \tag{2.53}$$

From ρ_χ we can obtain the moment generating function later by tracing out the system degrees of freedom:

$$\phi(\chi) = \mathrm{tr}_S\left[\rho_\chi\right]. \tag{2.54}$$

Using the modified density matrix and performing the same operations as before in section 2.5.1 results in the following expression for the modified Liouvillian

$$\mathcal{L}_\chi = \mathcal{L}_0 + \left(e^{i\chi} - 1\right)\mathcal{J}^+ + \left(e^{-i\chi} - 1\right)\mathcal{J}^- \tag{2.55}$$

where $\mathcal{L}_0$ is the standard Liouvillian from the previous section and $\mathcal{J}^+$ and $\mathcal{J}^-$ are forward and backward jump operators

$$\mathcal{J}^+\rho = \sum_{mn} \Gamma f^+(\omega_{mn})|m\rangle\, d^\dagger_{\alpha,mn}\rho_{nn}d_{\alpha,nm}\langle m|, \tag{2.56}$$

$$\mathcal{J}^-\rho = \sum_{mn} \Gamma f^-(\omega_{nm})|m\rangle\, d_{\alpha,mn}\rho_{nn}d^\dagger_{\alpha,nm}\langle m| \tag{2.57}$$

which can be calculated numerically using the already determined transition rates Γ. To access the moments which we need to calculate current and noise data we now expand ρ_χ into a Taylor series as ρ_χ contains the moment generating function (see equation 2.54).

$$\rho_\chi = \rho + \sum_{k=1}^{\infty} \frac{(i\chi)^k}{k!}\mathcal{F}_k. \tag{2.58}$$

Expanding the master equation in orders of χ results in the following expressions for the first three orders

$$\begin{aligned}
\dot\rho &= \mathcal{L}_0\rho,\\
\dot{\mathcal{F}}_1 &= \mathcal{L}_0\mathcal{F}_1 + (\mathcal{J}^+ - \mathcal{J}^-)\rho,\\
\dot{\mathcal{F}}_2 &= \mathcal{L}_0\mathcal{F}_2 + 2(\mathcal{J}^+ - \mathcal{J}^-)\mathcal{F}_1 + (\mathcal{J}^+ + \mathcal{J}^-)\rho,\\
&\vdots
\end{aligned} \tag{2.59}$$

The current, which is proportional to the first cumulant can be calculated now from the trace of the first moment using $\mathrm{tr}_S\mathcal{L}_0 = 0$:

$$I = -e\ \mathrm{tr}_S\left[\dot{\mathcal{F}}_1\right] = -e\ \mathrm{tr}_S\left[(\mathcal{J}^+ - \mathcal{J}^-)\rho\right]. \tag{2.60}$$

The noise S is related to the moments by $C_2 = M_2 - M_1^2$ and can be expressed as:

$$\begin{aligned}
S &= e^2\left(\mathrm{tr}_S\left[\dot{\mathcal{F}}_2\right] - \mathrm{tr}_S\left[\dot{\mathcal{F}}_1\right]^2\right)\\
&= e^2\mathrm{tr}_S\left[\dot{\mathcal{F}}_2\right] - 2e^2\ \mathrm{tr}_S\left[\mathcal{F}_1\right]\mathrm{tr}_S\left[\dot{\mathcal{F}}_1\right]\\
&= e^2\mathrm{tr}_S\Big[2(\mathcal{J}^+ - \mathcal{J}^-)\underbrace{(\mathcal{F}_1 - \rho\mathrm{tr}_S\left[\mathcal{F}_1\right])}_{=:\mathcal{Q}\mathcal{F}_1} + (\mathcal{J}^+ + \mathcal{J}^-)\rho\Big],
\end{aligned} \tag{2.61}$$

where $P = \rho \mathrm{tr}_S$ and $\mathcal{Q} = 1 - P$ are projectors onto the density matrix and its perpendicular part and obey $\mathcal{Q}\mathcal{L}\mathcal{Q} = \mathcal{L}$. Using the pseudo inverse of the Liouvillian

$$\mathcal{R} = \lim_{z \to 0} \mathcal{Q} \frac{1}{z - \mathcal{L}} \mathcal{Q} \tag{2.62}$$

allows us to write equation 2.61 as

$$S = e^2 \mathrm{tr}_S \Big[2(\mathcal{J}^+ - \mathcal{J}^-) \underbrace{\mathcal{R}(\mathcal{J}^+ - \mathcal{J}^-)\rho}_{=:\mathcal{Q}\mathcal{F}_1} + (\mathcal{J}^+ + \mathcal{J}^-)\rho \Big]. \tag{2.63}$$

Our Matlab code calculates $\mathcal{Q}\mathcal{F}_1$ numerically. From the calculated matrices for current M_I and noise M_{S_I}, color plots and line cuts as seen later in section 5.3 are created.

3 Construction of a Cryogenic Amplifier Setup

One of the main objectives of this work was the construction of an amplifier setup supposed to operate at cryogenic temperatures. It should be fitted into our existing dilution cryostat and be capable of measuring small current fluctuations (noise) in a sample. As such systems are not commercially available or at least not compatible with the limited space in our dilution cryostat (see section 4.2), it was necessary to design and build such a system from scratch. In principle current noise in a device can be determined by measuring fluctuations of the voltage drop across a known resistance. Because shot noise amplitudes can become very small for low currents (in the order of $10^{-31}\,\mathrm{A}^2/\sqrt{\mathrm{Hz}} \leq S_I \leq 10^{-29}\,\mathrm{A}^2/\sqrt{\mathrm{Hz}}$, see equation 2.33), it is crucial to achieve a high resolution, i.e., a high signal (= shot noise) to background noise ratio for the setup.
This can be realized by using voltage amplifiers together with a sufficiently high resistance as current-to-voltage converters. However large resistors introduce additional noise (equation 2.28) and also active measurement devices like amplifiers generate noise which is temperature dependent.
To keep the noise level as low as possible, it is crucial to use amplifiers with a low input noise and to find a compromise for the values of the resistors used. To further minimize noise levels one can think about putting the amplifiers and resistors to a fixed, low temperature inside a cryostat. Of course one has to consider the cooling power of the cryostat and compare it to the power dissipation of the amplifier parts. It is not possible to just install an amplifier at the mixing chamber stage with its cooling power in the range of a few μW. Therefore in our setup the amplification chain is distributed over several temperatures. Passive parts with no power dissipation are situated at the lowest temperature stage (mixing chamber) to minimize the thermal noise originating from the resistors. The active part of the setup, the low noise field effect transistor (FET) circuit, is directly connected to the liquid helium bath at a constant temperature of $\mathrm{T} = 4.2\,\mathrm{K}$.
The construction of our noise measurement setup was inspired by different experiments of other groups [8, 10, 15, 59, 71, 76, 77, 79, 92], but adapted for usage in our minidil dilution refrigerator. The overall circuit consists of three main parts, each one located at a different stage of the dilution cryostat (see figure 3.1).
The schematic shows two similar amplifier chains employed in the system in parallel. This setup is intended for future cross correlation measurements, for the moment only one of these is used.

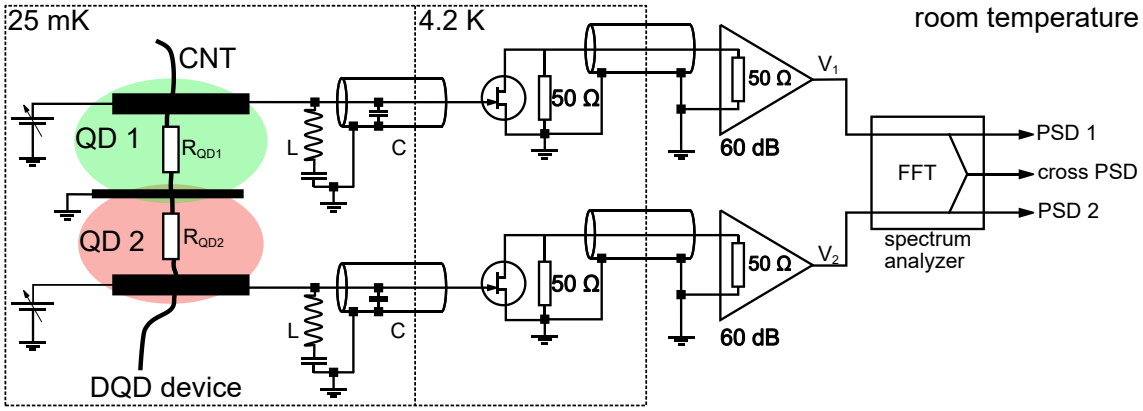

Figure 3.1: Simplified sketch of the cryo amplifier setup: Two similar amplification chains with passive RLC circuits at the base temperature stage and active components at T = 4.2 K, connected to the helium bath. An additional commercial RF amplifier at room temperature finalizes the setup. For reasons of clarity only the high frequency (noise) circuit is shown. See figure 3.7 for a sketch of the entire setup.

To correctly map the measured noise to the current and differential conductance of the sample, the latter two quantities have to be measured simultaneously with the noise signal. The system therefore has to be designed such that also low frequency signals from a lock-in amplifier in the Hz range are able to pass the circuit while also being amplified by our FET stage. At room temperature the signal is split into a high frequency part which is then fed into a spectrum analyzer for further analysis and a low frequency signal going back into the lock-in amplifier. The goal is to obtain a charging diagram of the quantum dot (see figure 2.9) for current, differential conductance (dI/dV) and noise or Fano factor.
In the following sections each sub system of the amplifier chain is explained in more detail.

3.1 RLC-Circuit

The sample holder of our system is located at the lowest position in the cryostat (see section 4.2). It is thermally coupled to the mixing chamber by a silver rod supported by a frame of stainless steel. This stage can thus reach temperatures down to base temperature (T ≈ 25 mK).
The sample chip itself is glued to a PCB board (see figure 3.2), electrical and thermal contact to the board is established by aluminum wire bonding. Two resonant circuits (RLC) with a resonance frequency of $f_0 = \frac{1}{2\pi\sqrt{LC}}$ are located on this board as well and therefore have the same temperature as the sample chip. All passive components used for our RLC circuit are certified non-magnetic to sustain the magnetic forces in the cryostat

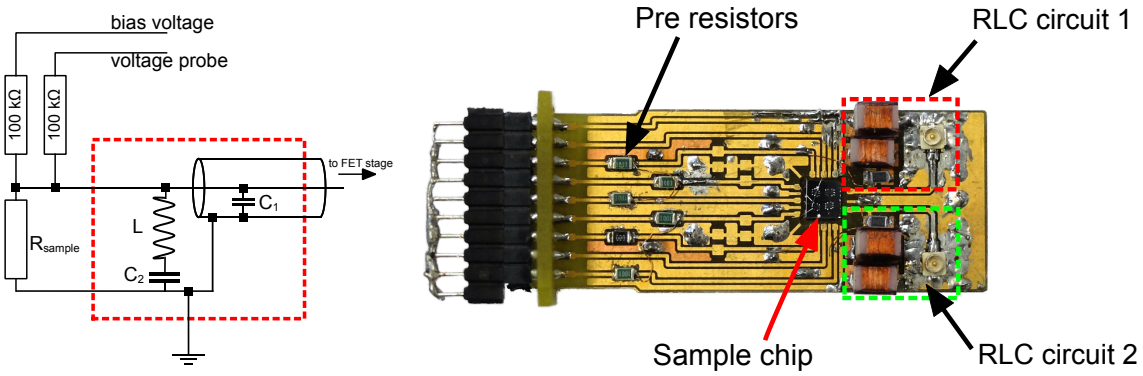

Figure 3.2: Sample holder PCB: pre-resistors and RLC circuit sit close to the sample chip which is connected to the board directly via wire bonding.

when measurements have to be performed at a high magnetic field. The capacitance of the RLC circuit is a combination of the cable capacitance of the coax lines from the board to the FET stage at T = 4.2 K and a second capacitance C_2 (Murata COG GRM21, 0805 surface mount) between the inductor $L = 66\,\mu H$ ($2 \times 33\,\mu H$ Coilcraft 1812CS) and ground as a correction, to equalize the small difference in cable capacitance of the two amplifier chains. The cable capacitances for both resonant circuits from the sample holder up to the FET stage were determined using a LCR-Meter (Agilent E4980A) and account for $C_{cable} = 134\,pF$ for the first circuit and $C_{cable} = 142\,pF$ for the second one with cable resistance of $R_{cable} = 40\,\Omega$ each. For the simulation shown in figure 3.4 the coaxial cables from the RLC circuits to the FET were modeled using a chain of 100 RC-circuits in series (see appendix B). The two $R = 100\,k\Omega$ resistors (Vishay TNPW thin film, 0805 surface-mount) before and after the sample act together with the coaxial lines as an RC - low pass filter to shield the sample from noise coming from the outside world.
For later cross correlation measurements it is crucial that the resonance curves of the two amplifier chains do not differ too much so that a maximum overlap of the two bells is maintained. For that purpose the difference in cable capacitances has to be compensated by an additional capacitance in the circuit. Table 3.1 shows an overview of the components used in the two RLC circuits on the sample holder board. Figure 3.3 shows raw data of a typical spectrum for the voltage noise S_V (after amplification) around the resonance frequency of one RLC circuit used in our setup. The amplitude of the bell shaped resonance curve is a measure for the impedance of the RLC circuit in parallel to the sample impedance R_S which is in series to the $50\,k\Omega$ resistors before and after the sample. In our extended analysis of the circuit (see appendix B) it turned out that for the particular sample measured in this work, the sample resistance is negligible as it is much higher than the impedance of the RLC circuit. For that reason the RLC circuit provides a conversion of current noise generated in the sample to voltage noise at the resonance frequency, which is $f_0 \approx 1.83\,MHz$. For reasons of verification of the chosen capacitances

	RLC 1	**RLC 2**
L	66 µH	66 µH
C_1	134 pF	142 pF
C_2	2.0 nF	1.1 nF

Table 3.1: Values of $C_{1,2}$ and L for both RLC circuits in the system. The additional capacitance C_2 is needed to compensate the different cable capacitances C_1.

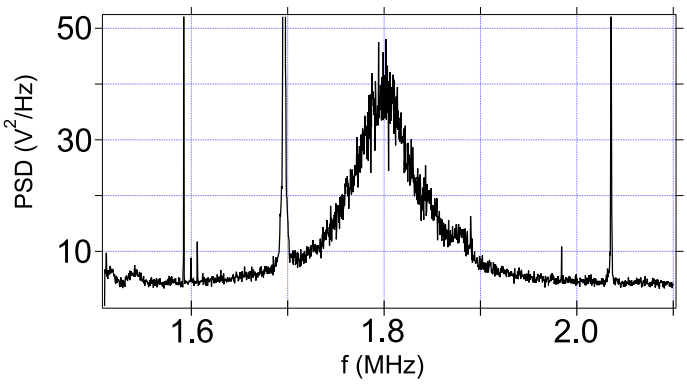

Figure 3.3: An example of the resonance curve generated by one of our RLC circuits. The already squared raw voltage data features Lorentzian shape with a center (resonance) frequency of $f_0 \approx 1.83\,\text{MHz}$.

we performed simulations of the circuit using LTspice IV.[1] With the help of this tool we were able to find proper values for C_2 in figure 3.2 to match the resonance frequency of the two RLC circuits. Figure 3.4 shows the results of a circuit simulation using the values of table 3.1.
As shown in figure 3.4, apart from the resonance bell at $f_0 \approx 1.83\,\text{MHz}$ also a *low frequency window* around $f \approx 100\,\text{Hz}$ is present which allows for lock-in frequencies to pass through the RLC circuit.
The voltage noise signal as well as the lock-in frequencies are transferred to the gate of a low noise p-HEMT field effect transistor at the T = 4.2 K stage via coaxial cabling.

[1] http://www.linear.com/designtools/software/#Spice

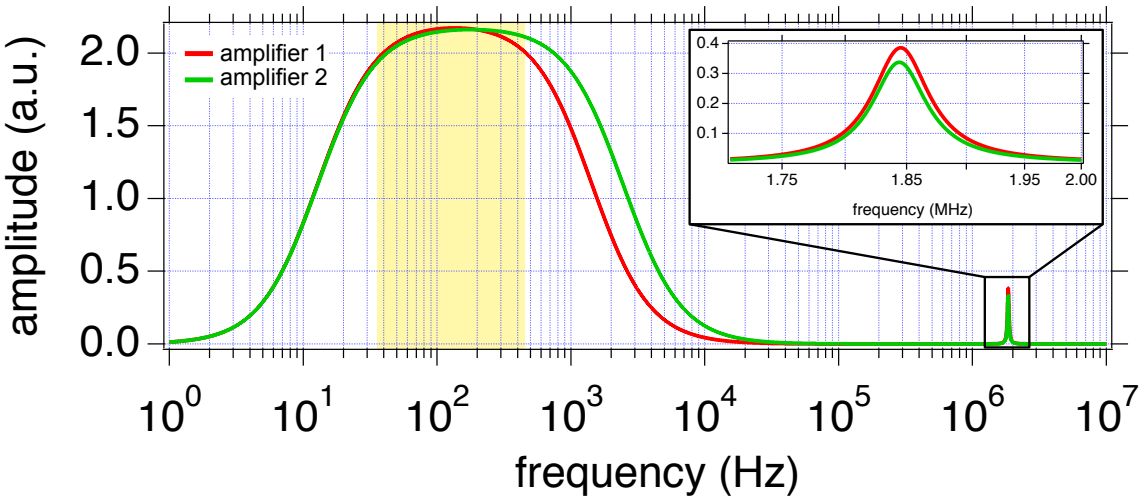

Figure 3.4: SPICE simulation of our RLC circuits. Red and green curves show the output amplitude for the first and second circuit respectively. At $f \approx 1.83\,\mathrm{MHz}$ a sharp resonance peak emerges. A zoom into the resonance bells is shown in the inset. The area where both curves overlap has to be maximized in order to perform cross-correlation measurements later. Lower (lock-in) frequencies can pass through a frequency window around 100 Hz.

3.2 4K Amplification Stage

The T = 4.2 K stage of the cryostat is directly connected to the Helium bath of the dewar by a copper rod. The cooling power is therefore sufficient to handle the heat load of active components used in the amplifier circuit. The two amplifier boards are fabricated on (8 mm x 8 mm) sapphire chips. Sapphire is both electrically insulating and at the same time a good thermal conductor at low temperatures [93]. These properties make sapphire the ideal material for our amplifier boards, since it allows for the patterning of electrical circuits, similar to a printed circuit board, and additionally provides good thermal contact of leads and electronic components to the copper walls of the cryostat.
Gold leads are patterned onto the chip by means of electron beam lithography and lift-off process, which is demanding as the sapphire is insulating and will charge upon irradiation with electrons and eventually deflect the beam so that the structures are not well defined and/or underexposed. To handle this problem, the scanning electron microscope (SEM) we usually use for lithography is operated in the so called *variable pressure mode* [94]: the pressure in the sample chamber of the SEM can be adjusted continuously from base pressure ($P_{base} \approx 10^{-6}$ mbar) up to P ≈ 30 mbar by injecting nitrogen into the chamber through an automatic mass flow controller. This atmosphere of nitrogen allows for charges on the sample chip to flow to the grounded chamber walls. On the other hand too much residual gas in the chamber leads to a scattering of the electron beam and can again affect the quality of the lithography. One has to find a compromise between discharge and sufficiently low scattering. In our case best results were achieved

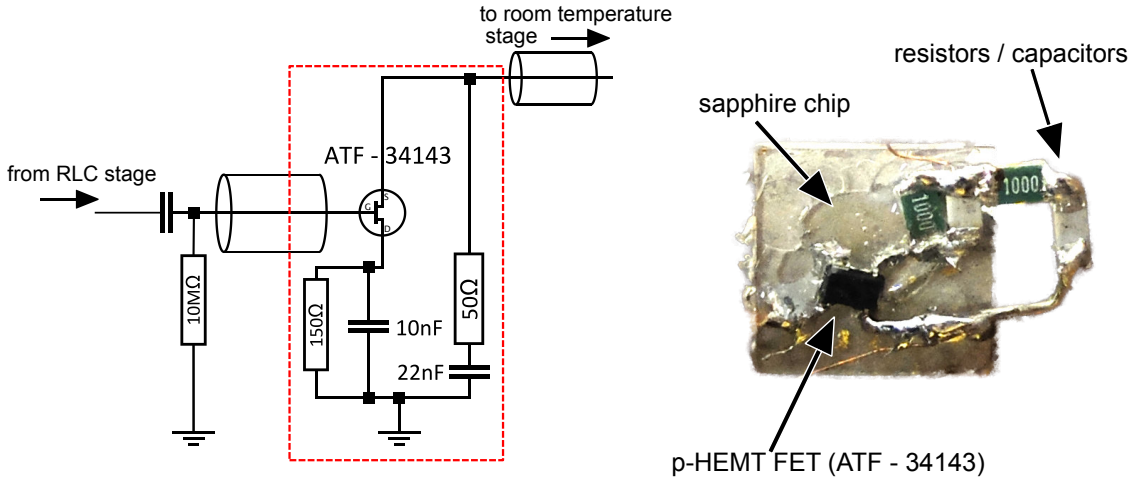

Figure 3.5: FET amplifier circuit fabricated onto a sapphire chip, thermally connected to the T = 4.2 K stage. The boards include a circuit to operate the FETs in self biasing mode.

at P ≈ 1 mbar. The system is equipped with a special detector which is able to provide images of sufficient quality for alignment purposes during EBL, despite the increased electron scattering due to a chamber pressure in the mbar range. After preparing the boards, the p-HEMT field effect transistors (Avago technologies type ATF 34143, data sheet: [95]) together with pre-resistors and capacitances as drawn in figure 3.7 are soldered onto the boards (see figure 3.5). The boards are then glued to the walls of a copper box in the cryostat using conductive adhesive (silver paint). After the cryostat is inserted into the dewar the FETs are thermally connected to the helium bath, their temperature should therefore be fixed at T = 4.2 K.
Each FET is operated in a *self biasing* mode: resistors between its drain contact and the ground, as well as between source and ground set the bias current through the transistor to a fixed value of $I_{bias} \approx 5.5$ mA. The source line provides the bias and at the same time passes the input voltage signal from the gate contact as current fluctuations to the room temperature frequency splitter. This has the advantage that only one line from the top of the cryostat down to the transistor is needed, the FET can therefore be easily included into the existing setup. One FET alone reaches gains of $g_{LF} \approx -10$ (negative means signal is inverted) in the lock-in frequency range and $1 \leq g_{HF} \leq 3$ in the MHz regime (see section 3.6).

3.3 Room Temperature Part

At room temperature the frequency splitter box (see figure 3.6) is connected directly to the head of the cryostat via SMA connectors. As sketched in figures 3.6 and 3.7 the box

contains a circuit which provides the bias for the FET at the T = 4.2 K stage generated by an external voltage source type Yokogawa GS200, as well as it serves as a frequency splitter
Again two similar circuits are implemented into this box, separated by a grounded conductive wall as a shield to avoid cross talk between them. The box can provide two independent bias voltages for the two FETs at the T = 4.2 K stage which allows for compensating intrinsic differences in the gain of the two FETs. The lines which provide the bias also carry the noise and lock-in signals arriving at the gate of the FET as fluctuations in the FET-bias current. The circuit now splits the fluctuations on the bias lines into a high and a low frequency part.

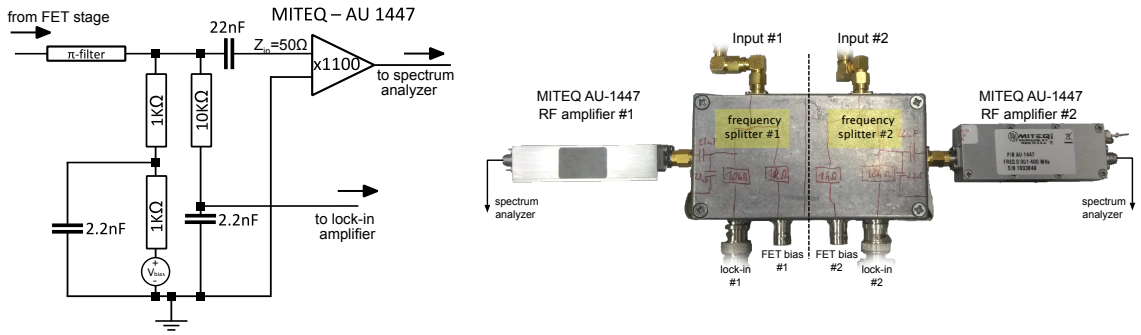

Figure 3.6: Room temperature frequency splitter box separates high frequencies (noise) from the low frequency (lock-in) signal. RF-amplifiers type MITEQ AU-1447 (Gain = 63 dB) are directly connected to the high frequency output.

The low frequency outputs pass the lock-in signal (f ≈ 100 Hz) directly back to the lock-in amplifiers or if the signal is too low an additional voltage amplifier can go in between. The high frequency outputs are connected directly to RF amplifiers type MITEQ AU-1447 featuring an additional gain of 63 dB before the signal arrives at the spectrum analyzer (Agilent 89140a). The two channel spectrum analyzer performs fast Fourier transformation of the noise signal and is capable of calculating the cross spectrum of two input channels.

3.4 The Complete Setup

The full cryo amp setup as it was ultimately included into the cryostat together with all measurement devices connected is shown in figure 3.7. Two bias branches labeled *bias 1* and *bias 2* provide two independent dc bias and ac excitation voltages ($V_{dc-appl}$, $V_{ac-appl}$) applied to a two terminal device, e.g., a CNT based double quantum dot. These lines are filtered against radio frequencies using π-filters. Additionally pre-resistors ($R_{pre} = 100\,\text{k}\Omega$) at each line close to the sample together with the cable capacitances form an RC low pass filter to cut spurious noise from the outside. The pre-resistors of course change the actual bias voltage at the sample when the sample resistance R_S is in the order of R_{pre}, the

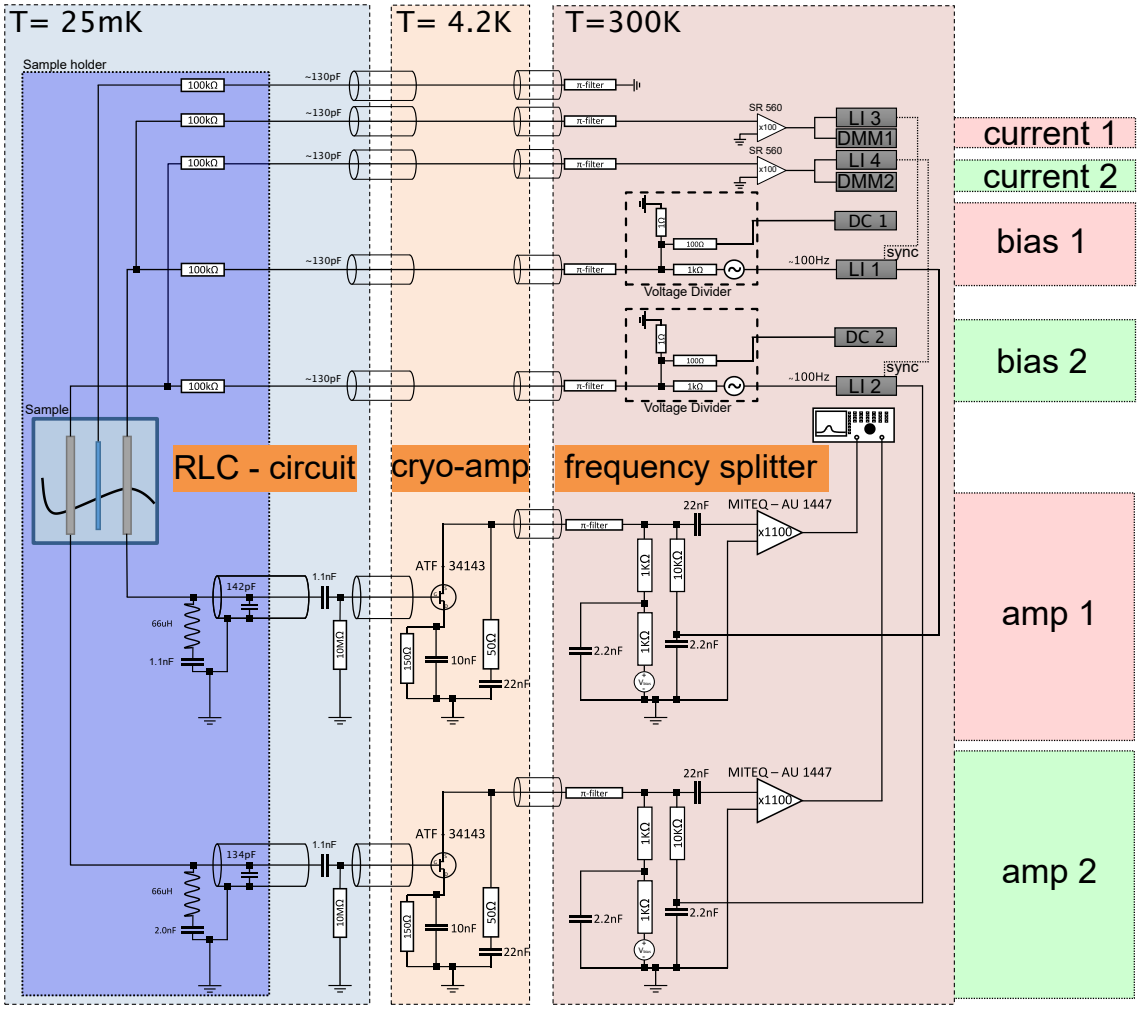

Figure 3.7: Our measurement setup consists of three main parts: the RLC circuit at base temperature (T = 25 mK) provides a resonant enhancement of noise. The signal is amplified by a FET transistor circuit at T = 4.2 K, passed to the room temperature frequency splitter / RF amplifier. The sections on the right-hand side indicate the **bias**ing, **current** detection and noise **amp**lification stages for amplifier chain 1 and 2 in red and green respectively.

actual values are smaller than the voltages applied from the outside. For this reason two further similar lines labeled *current 1* and *current 2* serve as voltage probes to determine both dc and differential current from the exact voltages at the sample (V_{dc}, V_{ac}). The ac bias V_{ac} at the sample is the same as the differential voltage dV. In this setup the current through the sample can be calculated according to

$$I_{dc} = \frac{V_{dc-appl} - V_{dc}}{R_{pre}}. \tag{3.1}$$

A similar relation holds true for the differential current $I_{ac} = dI$:

$$dI = I_{ac} = \frac{V_{ac-appl} - V_{ac}}{R_{pre}}. \tag{3.2}$$

The differential conductance of the sample is

$$\frac{dI}{dV} = \frac{I_{ac}}{V_{ac}} = \frac{V_{ac-appl} - dV}{dV \cdot R_{pre}}. \tag{3.3}$$

From the center contact of the device an equally filtered line arrives at the top of the cryostat. Instead of grounding the device through a cold ground connection at the base temperature stage, ground connection is established via the aforementioned cable on top of the cryostat using a terminator cap. This approach allows us to simply measure current from the device by replacing the terminator cap by an additional current amplifier. This is however not possible in a multi terminal device with common ground, here the current has to be calculated according to equation 3.1.
The two sections labeled *amp 1* and *amp 2* indicate the two high frequency amplifiers for noise detection included in the final setup. As described earlier each amplifier chain again consists of three parts. The RLC circuit at base temperature (T = 25 mK) providing a resonant enhancement of noise and confining the signal into a bell shaped resonance curve. The cryo-amp itself at T = 4.2 K amplifies the signal before the frequency splitter at room temperature feeds the high frequency signal into an additional RF amplifier and finally into the spectrum analyzer.

3.5 Signal Processing

This section describes how the signal is processed in the spectrum analyzer and later by means of software in the computer. As mentioned in the previous section the noise signals from the two amplifier chains arrive at a spectrum analyzer type Agilent 89410a. Here the fast Fourier transformation (FFT) and integration of the signal is performed to obtain the raw amplitude spectral density (ASD) in units of $\frac{\mathrm{V}}{\sqrt{\mathrm{Hz}}}$. In our case an integration over 100 spectra is sufficient, so that the resonance bell with its center frequency of $f_0 \approx 1.8\,\mathrm{MHz}$ is clearly visible.
For further processing one integrated spectrum (1600 data points) is acquired from the spectrum analyzer via GPIB interface. For that it is crucial that the sweeping of bias voltages is stopped completely during the integration time of the analyzer as the commands used by the GPIB bus for communication create distortions in the noise spectrum. The noise spectrum is then written into a data file along with other data such as the bias voltage, gate voltage, dc current, differential conductance. This means, depending on the resolution of the measurement, 20,000 spectra or more are acquired and written to the file which can result in large file sizes of several hundreds of megabytes even up to gigabytes. After the measurement the file is processed using the data analysis software Wave-

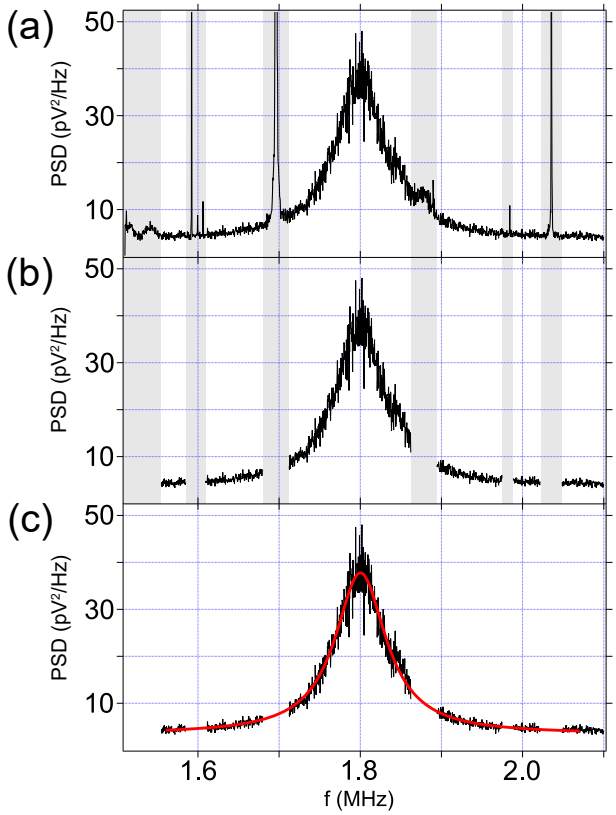

Figure 3.8: An example of a typical spectrum acquired from our setup. The raw data (a) features extrinsic noise peaks (gray marked areas) which are manually cut as can be seen in (b) to improve the quality of the later performed Lorentzian fits in (c) from which the amplitude is extracted.

metrics IGOR Pro 6.[2] The measured voltage signal from the spectrum analyzer $V_{meas}(f)$ has to be squared in order to obtain the power spectral density (PSD) $S_V(f) = V_{meas}(f)^2$ in units of $\frac{\mathrm{V}^2}{\mathrm{Hz}}$. Within the measurement window $1.51\,\mathrm{MHz} \leq \mathrm{f} \leq 2.10\,\mathrm{MHz}$ close to the resonance bell some distortions and sharp peaks arise. The amplitude of those peaks can be at least ten times higher that the bell (see figure 3.8 (a)) while their width usually is much smaller than the width of the resonance bell, therefore the unwanted parts of the curve can be removed from the spectrum by simply cutting out the data points and replacing them by "empty points" (NaN = not a number) to not change the scaling of the frequency axis (figure 3.8 (b)). After that an automatic fitting procedure cycles through all the acquired spectra and applies a Lorentzian fit to the resonance bell according to

$$S_V(f) = \frac{1}{\pi} \frac{\frac{1}{2}\Gamma}{(f - f_{res})^2 + (\frac{1}{2}\Gamma)^2} \tag{3.4}$$

where the bell's amplitude, i.e., the voltage power spectral density at resonance frequency $S_V(f_{res}) = \frac{2}{\pi\Gamma}$ is extracted (see figure 3.8 (c)).

[2] http://www.wavemetrics.com/

These values for the voltage noise can now be converted to current noise employing the conversion factor $g^2\alpha^2 = 3.6\times10^{15}\,\Omega^2$ from the calibration using a QPC sample chip (see section 3.6).
Having now the amplitude of the current noise for every single data point lets us calculate the Fano factors according to equation 2.34 and create matrices (and image plots) for all relevant measurement data. In figure 3.9 the process is visualized: (a) an example of a current map showing dc current versus gate voltage and bias voltage in the positive part of a stability diagram. For every point in (a) a complete spectrum of noise is acquired and saved into a file. For every spectrum the procedure mentioned above is performed and the noise amplitude is extracted (b). The noise amplitude values are again arranged into a matrix resulting in a noise map for this area (c). A similar map for the Fano factor can be calculated similar to equation 2.34 using the matrices for the current noise M_{S_I} and dc current M_I instead of single values and the elementary charge e:

$$M_{Fano} = \frac{M_{S_I}}{2\times M_I \times e}. \tag{3.5}$$

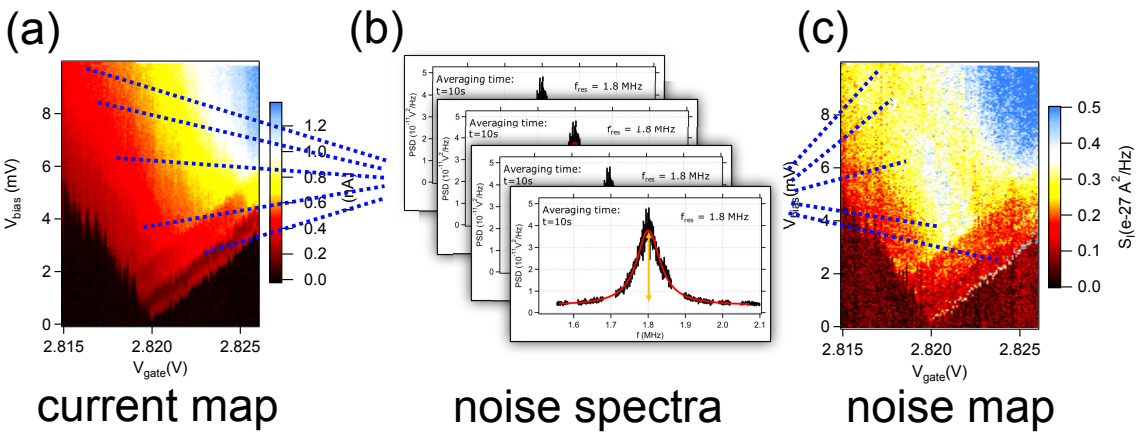

Figure 3.9: From current map to noise map: for every transport data point in the stability diagram also one full noise spectrum is acquired, processed and its amplitude is extracted. A matrix of these values in the correct order results in a map of noise across the Coulomb diamond area.

3.6 System Calibration

In a noise measurement it is necessary to have very accurate values for the current noise in the sample in order to calculate the Fano factor later. Small deviations in the measured noise can have a huge impact on the outcome and the evaluation of the experiment. For that reason a careful calibration of the entire setup is crucial.
In this section first the calibration of the high frequency circuit exploiting the known Fano factor in a quantum point contact is presented. After that also the calibration of

the low frequency part is described, which can be performed in situ directly before the measurement with the actual sample already mounted in the setup.

3.6.1 High Frequency Part

For calibration of the high frequency part of the setup a quantum point contact sample (QPC) was fabricated in a two dimensional electron gas (2DEG). On an AlGaAs/GaAs based heterostructure chip[3] a split gate pattern of gold was defined by e-beam lithography and a lift-off process[4] (see figure 3.10).

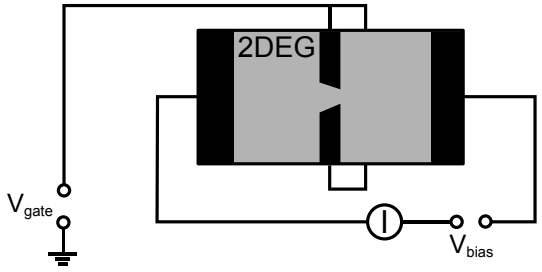

Figure 3.10: Schematic of the calibration setup: an AlGaAs/GaAs based two dimensional electron gas with gold contacts and gates was mounted into the noise setup as a sample. The gate voltage V_{gate} controls the conductance G through the 2DEG by depleting the area between the two fingers of the split gate electrodes resulting in a quantum point contact (QPC) behavior.

After mounting the QPC-chip in the RLC circuit of our nose amplifier setup as a sample resistance R_S, the setup was cooled down to base temperature (T = 25 mK).
By applying a negative voltage to the split gate, the 2DEG area between the gate fingers can be depleted which allows for controlling the width of the conducting channel. The conductance decreases stepwise by units of the quantum of conductance ($G_0 = e^2/h$) until the pinch off point is reached, the QPC is then completely closed and conductance is $G = 0$ [64].
To determine the overall amplification factor of our setup it is necessary to measure noise on a test sample with well known properties. As mentioned in section 2.32 the Fano factors of a quantum point contact close to the pinch off point where $t \to 0$ is supposed to be $F = 1.0$ [76].

[3] Heterostructure: courtesy of Imke Gronwald, Prof. Dr. D. Bougeard.
[4] Patterning done by Dr. Nicola Paradiso.

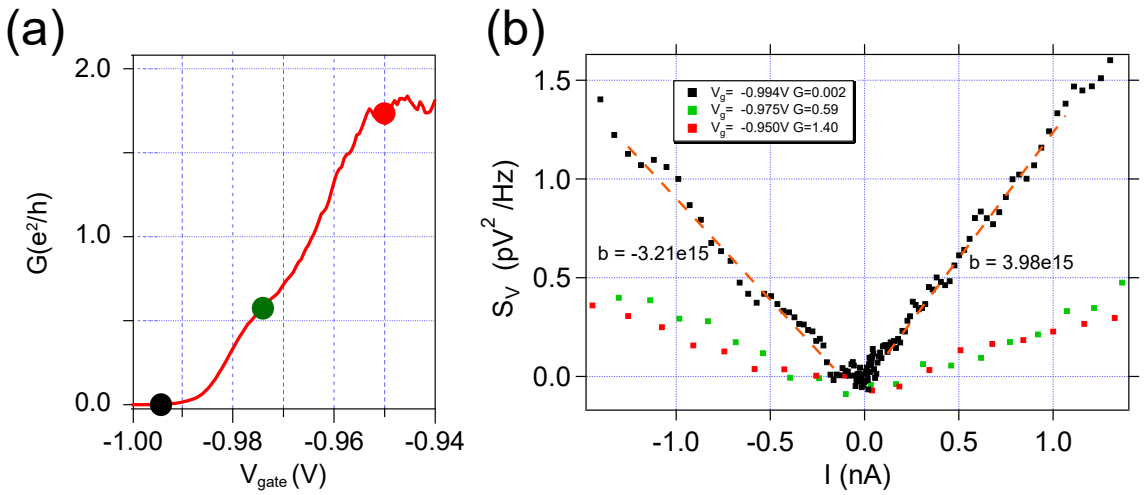

Figure 3.11: (a) Conductance of the quantum point contact vs gate voltage. (b) S_I vs I for three different conductance values marked in (a). Tuning the QPC close to the pinch off point ($G \approx 0.002\,e^2/h$, black curve) and assuming a Fano Factor of $F = 1.0$ [76] allows us to use the linear slope of this dependence as conversion factor to directly convert S_V to S_I according to equation 3.6.

After characterizing the QPC by means of a gate-trace according to [64] (figure 3.11 (a)), voltage noise (S_V) versus current (I) was measured for different transmissions of the QPC[5]. As expected the maximum slope is observed close to the pinch off point. Assuming a Fano factor $F = 1.0$ in this region one can directly deduce [79]

$$S_I = \frac{S_V}{\alpha^2 g^2} = 2e\langle I\rangle \cdot F \tag{3.6}$$

with g being the gain of the amplifier chain and α being the impedance of the RLC circuit at resonance. It is not necessary to know these two values independently, $g^2\alpha^2$ is the conversion factor from S_V to S_I.
As a mean value for the conversion factor one can extract from the calibration measurements the conversion factor for the amplifier chain used in the later experiment:

$$g^2\alpha^2 = 3.6 \times 10^{15}\,\Omega^2. \tag{3.7}$$

Noise was detectable down to a threshold current of $I_t \approx 100\,\mathrm{pA}$. From the linear fits in figure 3.11 we can extract the resolution of the entire amplifier chain which accounts for $S_{V_{min}} \approx 7.5 \times 10^{-14}\,\mathrm{V^2/Hz}$ or $S_{I_{min}} \approx 2.9 \times 10^{-29}\,\mathrm{A^2/Hz}$ converted to current noise.

3.6.2 Low Frequency Part

In a multi terminal measurement sometimes two or more independent bias voltages have to be applied to the sample. For instance in reference [18] where two parallel quantum

[5] Calibration data acquired by Michael Schafberger.

dots are investigated. If only one common terminal for the ground is available, the currents through such a sample can not be detected independently, it is therefore necessary to detect current and conductance at the same side of the sample where also the signal is injected. An example for such an experiment would be a carbon nanotube based double dot where only one additional center contact between the two bias contacts is available (see figure 3.1). For a scenario like the above mentioned, we incorporated a low frequency part in our setup which is used to directly detect the injected signals.
The fact that the signal is detected at the same side as it is applied to the sample makes a calibration of the low frequency circuit relatively straightforward: when no sample is connected the measured signal has to be exactly the same as the injected one. The same is true for a situation where the sample is mounted into the setup but is in blockade and no voltage drop occurs at the sample.
To obtain the amplification factor g_{LF} in situ, the actual sample, a CNT quantum dot in our case, is set to a non-conductive state by changing the gate voltage accordingly. Then a signal of known amplitude V_{ac} from the lock-in amplifier is applied to the sample. The signal is amplified by the p-HEMT in the cryostat (see section 4.2) and returned to the lock-in amplifier via the room temperature frequency splitter (section 3.3). The amplification factor is then defined as

$$g_{LF} = \frac{V_{FET}}{V_{ac}} \tag{3.8}$$

with the measured voltage V_{FET}.

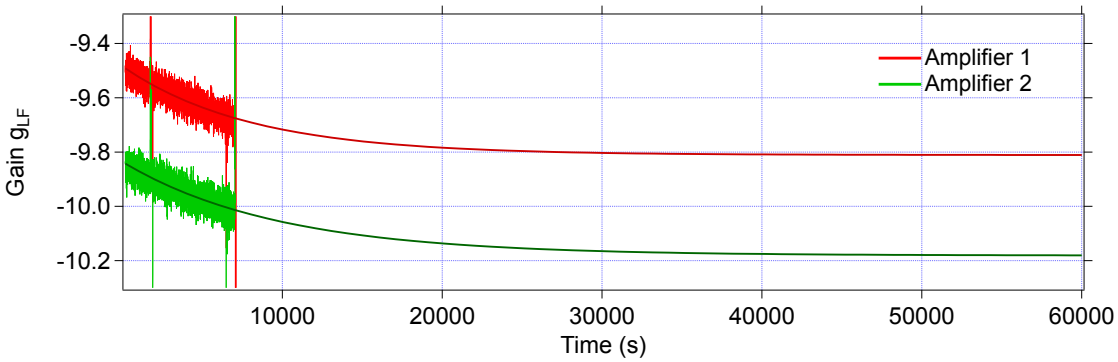

Figure 3.12: Low frequency gain g_{LF} for amplifiers 1 and 2 as a function of time since activating the p-HEMT transistors. The gain values are negative which means the signal is inverted, the absolute amplitudes increase with time and stabilize after $\Delta t \gtrapprox 50,000\,s$.

In figure 3.12 the measured gain g_{LF} for both amplifiers is plotted versus time directly after turning on the p-HEMT by applying a bias voltage to the transistors. The gain was measured for a time period of $\Delta t = 7,000\,s$. Fitting the time evolution using an exponential decay exhibits that the gain reaches a stable value after a relatively long time of $\Delta t \gtrapprox 50,000\,s$ which equals roughly 14 hours. For that reason it is recommended to

apply the FET-bias in a very early stage of the experiment, directly after reaching base temperature or even before, during the cool down process.
For our setup we obtained the following values for the low frequency gain for the two amplifier chains:

	Amp 1	**Amp 2**
g_{LF}	-9.8	-10.2

Both values being negative means that the cryo amplifiers are inverting the signal, this should be taken into account when acquiring and further processing the data.
The aforementioned values for the gain were reproducible after several cool-down cycles of the cryostat with the same p-HEMTs. However to be sure that the gain is still correct this calibration can be performed prior to every measurement. After replacing the transistors a recalibration is mandatory.

3.7 Chapter Summary

In this chapter we have described the planning and construction of our noise measurement setup. The basic idea was that the system should be capable of measuring cross correlation data and also include an RLC circuit to enhance the signal in a given frequency range (see section 2.3.2) and thus increase the measurement bandwidth which is otherwise limited by the cabling of the cryostat which was originally not designed for high frequency measurements. At the same time the circuit had to be planned such that also the low frequency signal, the ac-bias, can pass the circuit. To keep the bandwidth as high as possible while also improving the signal-to-noise ratio, a printed circuit board was developed which incorporates two RLC circuits, all the pre-resistors needed for filtering as well as the sample chip itself which is glued and wire bonded directly to the board. At the T = 4.2 K stage two independently biased p-HEMT transistors, connected to the RLC circuit via coax cables, amplify the signals which are then transferred through the existing cabling to a frequency splitter box on top on the cryostat. There the signals are split into a low- and a high frequency part which then go back to the lock-in amplifier and a commercial RF amplifier respectively. The high frequency signals are then fed into a spectrum analyzer for further analysis. The complete setup as described in section 3.4 is therefore capable of dealing with many different types of samples and experiments with flexible biasing schemes. For very special demands the filtering, cabling and even the RLC circuit can be altered comfortably on the printed circuit board. The idea is that one can design custom boards (sample holders) for the particular experiments.
To complete the picture, a software routine developed in the scripting language Perl (Lab::Measurement) was designed to control the measurement, acquire all data and save it into data files which can then be further processed using a second software routine implemented in IGOR Pro. The latter one directly produces color plots or “maps” of the

measured noise data. All the software components can of course be customized for various types of measurements.
With having implemented a complete noise measurement setup into our dilution refrigerator, including a corresponding software solution for analysis, we now have a very powerful tool on hand which will serve numerous investigations and experiments to come.

4 Sample Fabrication and Experimental Methods

After the construction and calibration of our noise amplifiers as described in chapter 3, carbon nanotube based quantum dot chips should be mounted for performing the first noise investigations in such devices. In this chapter the experimental methods used in our studies are presented, it should give a basis for the experiments described in the next chapter. First the device itself, its design and preparation process, later the measurement setup including the cryogenic environment, transport measurements and the actual noise detection circuit as it was employed in the experiment is presented.

4.1 Sample Fabrication

The following section is intended to give a brief description of the process of sample preparation. It contains the preparation of the substrate material including defining and deposition of the alignment markers by electron beam lithography (EBL) and dc sputtering, the growth of carbon nanotubes (CNT) by chemical vapor deposition (CVD), and the location of CNTs and deposition of metallic contacts to the tubes. Detailed recipes of the entire process can be found in the appendix C.

4.1.1 Substrate Material

The material used in our experiments was boron-doped (p++) silicon assuring conductivity also at low temperatures. The wafers are covered by a 300 nm thick layer of SiO_2 grown by thermal oxidation. This type of substrate allows us to use the entire chip as a global backgate. To establish electrical contact to the substrate the chip has to be glued into the chip carrier using silver paint to contact the gate from the backside of the chip. Another possibility is to use a diamond scraper to open a small hole in the oxide layer and connect the substrate directly from top via bond wires. As we were using a special printed circuit board without a conductive bottom plate below the sample, we chose the latter of these possibilities.

4.1.2 CVD Catalysis

From wafers of the substrate material mentioned in section 4.1.1, chips of 16 mm x 16 mm were cleaved after diamond scraping. On these chips an array of alignment mark-

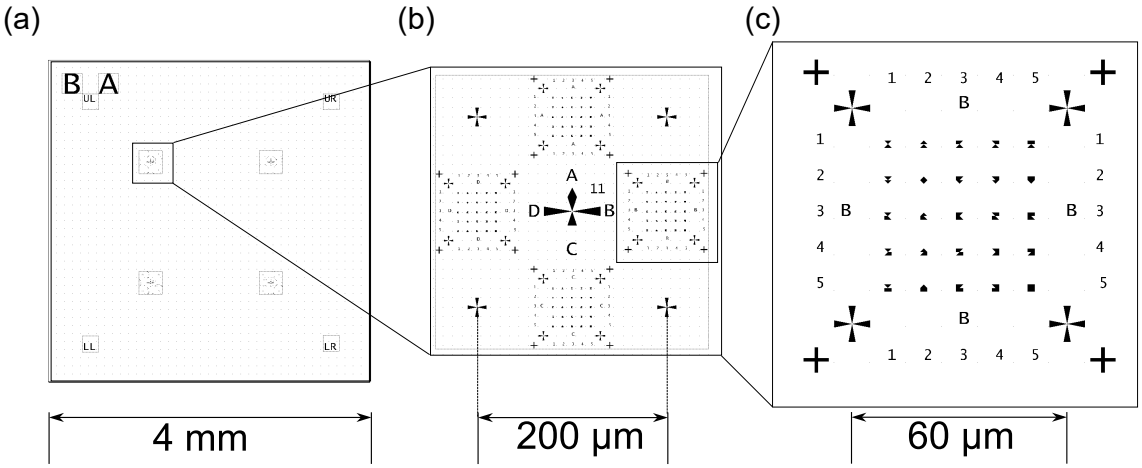

Figure 4.1: Alignment markers on the substrate chip: (a) one chip of 4 mm x 4 mm in size containing four 200 µm x 200 µm areas (b). Such a smaller area again consists of four coordinate fields of 60 µm x 60 µm where the nanotube growth takes place.

ers is defined by means of electron beam lithography (see figure 4.1). All of them contain markers for 16 smaller chips (4 mm x 4 mm). Each of those smaller chips again contains four arrays holding coordinate fields each. Therefore theoretically 16 devices can be fabricated on one 4 mm x 4 mm chip. For the alignment markers several conditions have to be fulfilled: the pattern has to be unique, so that certain areas on the chip can be found again later when it comes to repositioning and lithography of actual leads to the carbon nanotubes. Furthermore, a material has to be used which survives the rough conditions inside the CVD system, i.e., a temperature of 700–900 °C and an atmosphere containing H_2 and CH_4 (see appendix C.2). The material also has to be visible under the electron microscope to allow for repositioning in the later EBL process.

After testing several materials like Cr, Ti, Pd, Pt it turned out that rhenium (Re) is most suitable for this application.

After sputtering of a 30 nm thick layer of Re followed by a lift of process the substrate chip is ready for catalyst deposition.

In the center of each of the 60 µm coordinate fields (see figure 4.1 c) a dot or sometimes star shaped area of diameter ~ 2 µm is defined by EBL in a two layer PMMA resist system, to assure a large undercut. After developing the exposed areas 25 µl of catalyst solution are deposited on the sample using a pipette. The sample is then immediately blown dry with N_2 and baked out for 5 min on a hotplate at 150 °C. The exact catalyst composition can be found in C.2. For the lift of process the chip is then dipped upside down into a bath of acetone at a temperature of 60 °C. The PMMA dissolves and only the catalyst dots remain on the chip. Now a layer of PMMA is spun onto the chip as a protecting layer and the 16 mm x 16 mm chip is cleaved into 16 smaller pieces which then are further processed separately.

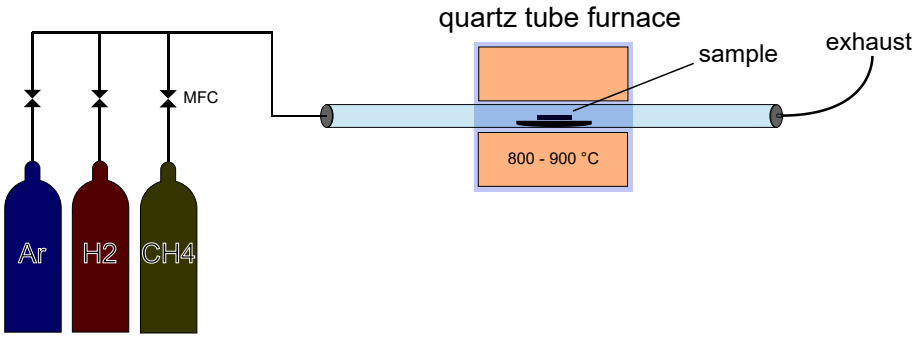

Figure 4.2: Sketch of the CVD system used for the growth of carbon nanotubes (CNTs). A quartz glass reactor sits inside a tube furnace. Process gases (Ar, H_2, CH_4 or C_2H_4) are fed into the tube via manual flow regulators (for Argon and C_2H_4) or computer controlled mass flow controllers (MFCs) for very low gas flows (used for H_2 and CH_4).

The actual CVD process (based on [96]) takes place in a fused quartz tube reactor which is located inside of a tube furnace (see figure 4.2). The sample chip is placed on a fused quartz plate in the center of the tube reactor. On one side of the tube the process gases are fed in via computer controllable mass flow controllers (MFCs) which allow for exactly controlling the flow of each gas and thus the composition of the process atmosphere. In a chemically inert atmosphere of pure argon (Ar) the furnace is heated up to reach the desired process temperatures between 800 °C and 900 °C. The argon flow is then stopped and a mixture of methane (CH_4) and hydrogen (H_2) is injected into the quartz tube where the decomposition of methane starts and carbon atoms form CNTs at the molybdenum particles deposited with the catalyst solution. Typically after 10-20 min this process is stopped by closing the stream of CH_4 and H_2 and continuously flushing the quartz tube again with Argon to remove residual process gases. The furnace is then turned off and it cools down to room temperature within ~ 30 min, the sample can be taken out of the reactor.

4.1.3 Lithography and Metalization

After the CVD process (see section 4.1.2) it has to be checked whether the growth of CNTs was successful. This can be done either by means of a scanning electron microscope (SEM) or atomic force microscopy (AFM). Since the SEM is much faster and therefore more convenient for a large number of chips, this was the method of choice for us. The drawback of SEM imaging is that the electron beam scanning over the sample can deposit amorphous carbon from residual gases in the SEM chamber on the sample which could affect the quality of the CNTs. To keep this effect small the acceleration voltage of the electron beam has to be kept as low as possible. As a good compromise values of $0.5\,\mathrm{kV} \leq V_{acc} \leq 2\,\mathrm{kV}$ offer low contamination, sufficient contrast to see the tubes and at the same time image distortions at the edges of the image are negligible. Figure 4.3

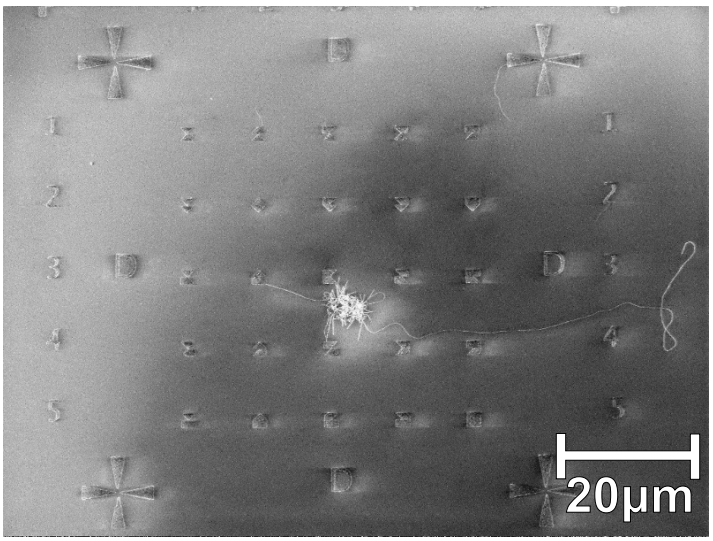

Figure 4.3: SEM image of one coordinate array on the sample chip after a successful growth process. From the catalyst dot in the center of the image carbon nanotubes grow in random directions within a stream of process gas and eventually lie on the substrate.

shows a typical SEM image of a successful CNT growth. Two relatively long tubes were growing out of the catalyst dot in the center of the image. The density of tubes around the catalyst dot is sufficiently low so that contacts, gates, as well as the corresponding leads can be designed around them without the risk of creating shortcuts between the leads by other tubes.

SEM images like the one in figure 4.3 can be imported into the software eDraw which is part of the eLitho[1] package, an e-beam lithography control software. Within this software all kinds of shapes can be drawn directly onto the imported SEM micrographs. Figure 4.4 shows screen shots of eDraw including the designed contacts, leads and gates. Typically the devices are fabricated in a two step process since different materials are needed as contacts to the same tube. In our case one of the contacts (blue in figure 4.4) was made of rhenium (Re), while in a second step all the other structures made of palladium (Pd) were fabricated (red in figure 4.4).

For the first step the chip was covered with PMMA resist of type 200 k/3.5 % (typical thickness $\sim$ 100 nm) for the rhenium contacts. After the exposure of the desired structures the exposed areas are developed using a mixture of isopropanol (IPA) and water (H_2O). This developer solution shows superior to the standard MIBK/IPA mixture in terms of contrast and edge roughness and also exhibits lower undercuts [97]. This is important as the sputtering process explained later is an isotropic process and therefore tends to cover the walls of free standing resist and the undercut areas with metal, which makes the lift-off difficult and may compromise the overall quality of the metallic struc-

[1] eLitho and eDraw are part of the nanonic eLitho package (www.nanonic.de).

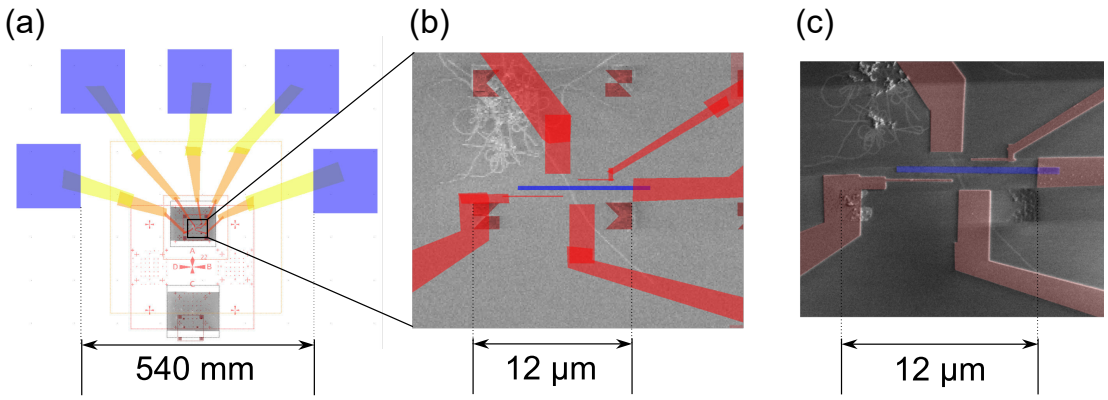

Figure 4.4: This figure shows an example for a sample design created with the software package eDraw/eLitho. In (a) one entire structure including the bonding pads is shown. (b) Zoom into the contact electrodes and leads which have been designed directly on an SEM micrograph of the carbon nanotube grown on the substrate chip. c) Colorized SEM picture of the metalized structures on the nanotube after the lift-off. The superconducting rhenium contact (blue) has been defined as a first step, followed by the palladium gates and leads (red) as a second step.

tures. For similar reasons the resist thickness was chosen only slightly higher than the metal layer thickness to reduce the area of free standing resist. Rhenium is deposited by means of dc sputtering, i.e., argon ions are being accelerated onto a massive rhenium disk, the target. Particles from the target are ejected by the impact of argon ions and projected onto the sample chip where they form a continuous metal film. After the lift-off process only the rhenium contact strips remain on the chip. Together with the contacts, also additional alignment crosses are deposited in their vicinity to allow for repositioning in the following lithography step.
In a second step the outer contacts to the tube, gates and all the leads including the bond pads are written onto the sample by EBL. Therefore exact repositioning is required to avoid shortcuts, e.g., gates touching the tube or contacts. For this step a different type of PMMA is used: 200 k/7 % (typical thickness $\sim$ 300 nm) developed using the standard solution MIBK/IPA which provides an undercut in the resist. Metalization of these structures is realized by thermal or e-gun evaporation. In both cases the material is heated above its boiling point in high or ultra high vacuum (UHV) conditions. The metal vapor condenses on the sample forming a continuous layer. After another lift-off step the chip is finished (see colorized SEM image: figure 4.4 c) and ready for bonding.

4.2 Measurement Setup and Procedure

As explained in sections 2.7 and 2.3, for quantum dots and shot noise experiments low temperatures are necessary to enable Coulomb blockade ($k_B T \ll e^2/C_\Sigma$) as well as to suppress thermal noise as effectively as possible ($k_B T \ll eV$).

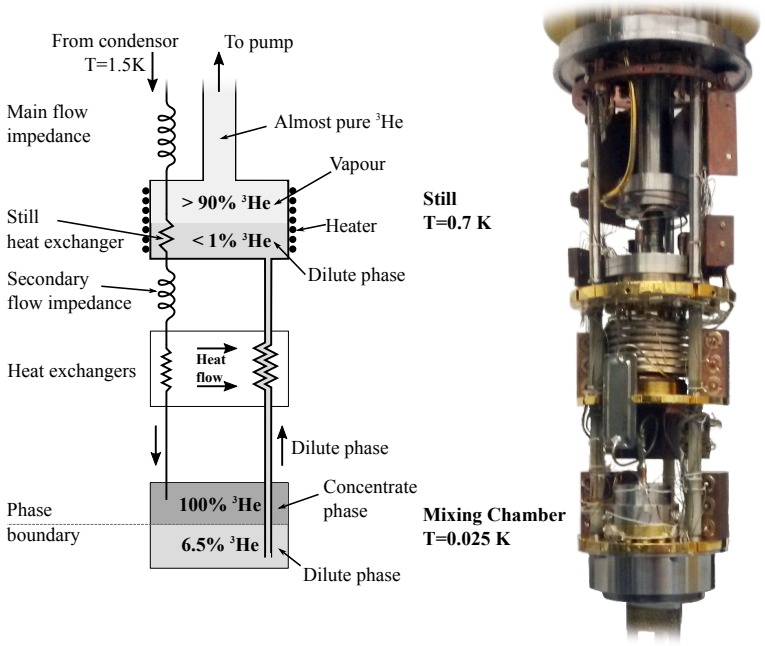

Figure 4.5: Left: dilution refrigerator after [98]. Right: photograph of the dilution system actually used in this work.

4.2.1 Cryogenics

For generating low temperatures in our experiments a ^{3}He/^{4}He dilution refrigerator built by cryoconcept[2] was used. Figure 4.5 shows a schematic of the dilution refrigerator circuit together with a picture of the actual apparatus used for this work. The cooling mechanism in this kind of refrigerator is based on an incomplete phase separation between liquid ^{3}He and ^{4}He below $T \approx 870\,\mathrm{mK}$ in a mixture of these two isotopes. While there is a pure ^{3}He or ^{3}He-rich phase, the fraction of ^{3}He in the ^{4}He in equilibrium can never come below 6.6% (^{3}He-poor phase). If now the concentration of ^{3}He is artificially decreased by removing ^{3}He atoms and adding them to the ^{3}He-rich phase, ^{3}He atoms have to undergo a phase transition in the mixing chamber from the ^{3}He-rich to the ^{3}He-poor phase to maintain the concentration of 6.6 %. This process is endothermic, i.e., it absorbs energy from its surroundings which leads to a further cooling of the mixing chamber and the sample. In the system used in our experiments the lowest reachable temperature (*base temperature*) is $T \approx 25\,\mathrm{mK}$ which corresponds to a thermal energy of $E_{th} = k_B T \approx 0.002\,\mathrm{meV}$. A more detailed description of many kinds of cooling techniques including ^{3}He/^{4}He dilution refrigeration can be found in references [93, 98].

[2] http://www.cryoconcept.com

All dc cabling from room temperature down to the sample holder including filtering (copper powder filters) was done by our group.
Recently the system was equipped with a noise measurement setup (see chapter 3).

4.2.2 Actual Measurement Setup

Our device is fabricated as described in section 4.1: three contact leads are defined on top of a CVD grown carbon nanotube by electron beam lithography. Two outer electrodes of palladium (Pd) and one inner rhenium (Re) contact were intended to define a double quantum dot (DQD) in the tube which then can be used as a Cooper pair beam splitter device, similar to the devices used in [19, 20].
The chip is glued onto a PCB board (see section 3.1) instead of using a standard chip carrier which makes wire bonding rather difficult. The PCB has to be clamped onto a custom holder to fit into the wire bonder, also the bonding is limited with respect to the wire direction as the lever arm which holds the bonding tool may touch some of the passive components on the board, especially the inductors which prevent the tool from reaching the sample. An additional difficulty is the fact that the used aluminum wire hardly sticks on the conducting paths of the PCB. To avoid any unnecessary damage to the samples, the chips were not tested in a probe station prior to wire bonding. After bonding the PCB was mounted directly in the cryostat (see section 4.1) where a quick test at room temperature was performed. This test includes applying a source-drain voltage and measuring the current through the tube. A second important test is to check if one or more gate electrodes are leaking to the tube or to one of the contact electrodes. All gates together are connected to a voltage source which performs a sweep from -1 V to +1 V while a current amplifier connected to both source and drain leads detects a possible current. Only samples with a reasonable resistance at room temperature in the range of

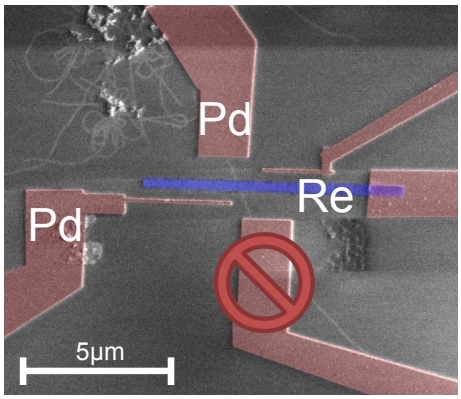

Figure 4.6: SEM micrograph of one of the samples used in this experiment. A carbon nanotube with three contacts on top (2x Pd, 1x Re). Two palladium sidegates are deposited close to the tube. In addition the chip itself acts as a global back gate to the sample. One of the Pd contacts (or the lower CNT segment) was not working (indicated red)

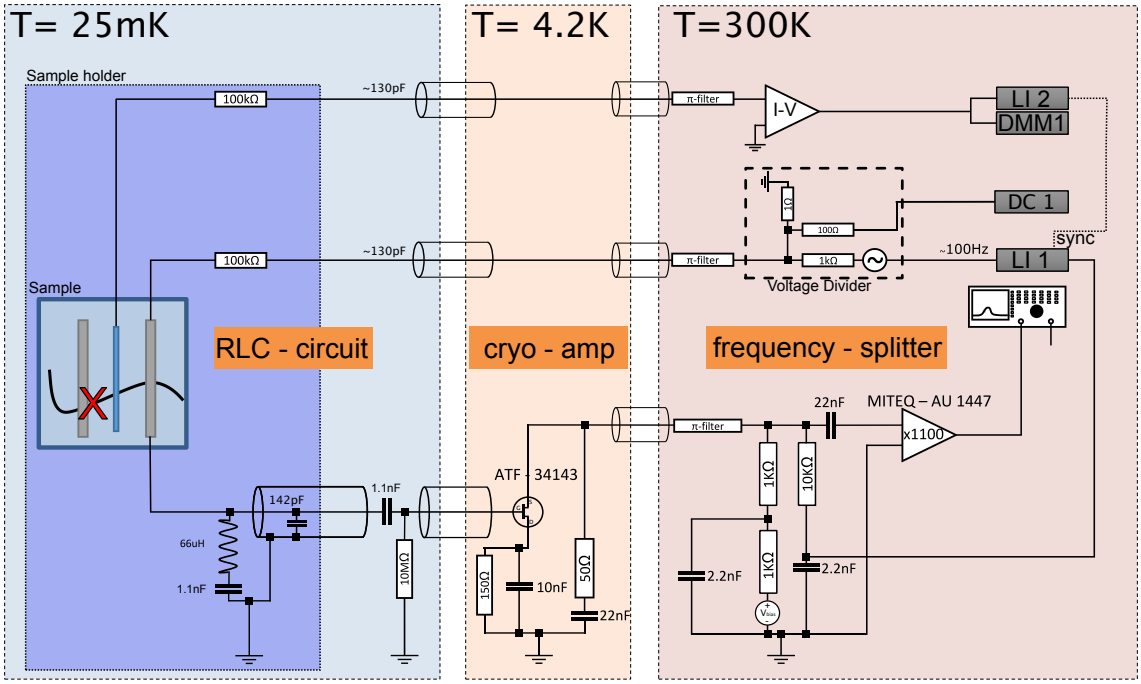

Figure 4.7: Schematic of the actual circuit used in the experiment. One amplifier chain is connected to the sample at the biased source contact. The sample ground is provided via a current to voltage converter at room temperature. Dc current, differential conductance and voltage noise at the source contact can be measured simultaneously.

$50\,\mathrm{k\Omega} \leq R_S \leq 500\,\mathrm{k\Omega}$ that show no gate leakage were cooled down to base temperature after repeating the aforementioned tests at helium bath temperature T = 4.2 K after the cryostat is inserted into the dewar. After preparing more than 100 chips one can conclude that only less than 10% of all the devices which survived the wire bonding fulfilled the conditions to be cooled down to base temperature. As it turned out after the cool-down procedure of the sample we used in this work, one of the two outer contact leads on our chip, or one segment of the nanotube was not functional. It was not possible to pass current from one side contact to the other but only from the center contact to one of the side contacts. This situation is depicted in figure 4.6.

For the actual experiment we still were able to operate the device as a single quantum dot (see section 2.2) with one sidegate and a global backgate available to change the electrical potential.

With the reduced device complexity the actual amplifier setup simplifies as only about half of the full setup (see section 3.4) was needed for the measurement. The actual circuit used in the experiment is shown in figure 4.7.

The quantum dot is biased via one of the side contacts which from now on will be called the *source* contact. A small ac excitation ($\approx 10\,\mu\mathrm{V}$) from the signal output of a lock-in amplifier is added on a dc bias voltage from a dc source by a double voltage divider

which is connected to the sample contacts through π-filters and a pre-resistor. One cryo-amplifier chain (see chapter 3) is connected to the same contact.
The sample ground is provided to the *drain* contact by a current to voltage converter at room temperature which is connected to the sample stage via the very same filtering as the source line. For reasons of clarity the gate lines are not included in figure 4.7. Apart from the global backgate, also one of the two sidegates to the tube could be used to manipulate the chemical potential in the quantum dot. In the later measurement it turned out that the side gate was more stable than the backgate.
All measurement devices (dc sources, multimeters, lock-in amplifiers and the spectrum analyzer) were connected to a measurement PC via GPIB interface and controlled by *Lab::Measurement*[3], a stack of software based on the programming language *Perl*[4] which allows for the easy control of our measurements using simple scripts written in Perl. The measurement procedure can be constructed using loops and other control structures within the Perl syntax. Data can be acquired and processed and eventually written into files on the PC.

4.2.3 Measurement Procedure

The noise measurement procedure is very similar to a bias spectroscopy measurement on a quantum dot system. First after cooling down the sample to base temperature the gate of the QD is varied at zero bias to find a region of the gate voltage where the differential conductance shows peaks with a regular behavior, i.e., equidistant spacing, similar height (as in figure 2.8 b). After such a region was found and turned out to be stable, which means that the pattern is similar upon sweeping the gate voltage in both directions and does not show a strong gate hysteresis, one can start to also vary the bias voltage.
The gate voltage is then changed stepwise, after each step the bias voltage is swept in one direction and back to the starting value. Current and differential conductance are acquired only in one direction to account for the hysteresis in bias voltage which is distorting the measurement otherwise.
The data points are arranged in matrix form which can be plotted as a stability diagram with Coulomb diamonds as in figure 2.9.
To include noise into such a measurement one has to take into account the fact that the spectrum analyzer has to perform integration over many noise spectra and that during this time it is crucial to avoid any communication of measurement devices with each other or with the PC via GPIB interface (see section 3.5). The following list briefly describes the measurement loop:

1. sweep gate voltage to starting value
2. sweep bias voltage to starting value

[3] http://www.labmeasurement.de
[4] http://www.perl.org

3. acquire dc current and dIdV from multimeter / lock-in and write to file
4. start averaging of spectrum analyzer
5. **waiting time** till averaging is finished (**no GPIB communication** during this time)
6. acquire complete noise spectrum from spectrum analyzer and write to file
7. increment bias voltage by one step (step size determines the resolution)
8. go back to step 3 unless bias end value is reached
9. if bias end value is reached ⇒ increment gate voltage by one step (step size determines the resolution)
10. go to step 2 unless gate end value is reached.
11. if gate end value is reached ⇒ **measurement is finished**

An exemplary Perl script for such a simultaneous transport and noise measurement can be found in appendix D.
The measurement time is set by the resolution of gate and bias voltage as well as the integration time of the spectrum analyzer which in turn sets the sensitivity of the noise setup. The measurement time can be estimated roughly by

$$t_{meas} = N_{gate} \cdot N_{bias} \cdot t_{int}$$

with $N_{gate/bias}$ the number of points on the $V_{gate/bias}$-axes, and t_{int} the integration time of the spectrum analyzer, neglecting the time for sweeping the bias back to start value. For instance a measurement with a resolution of 200 x 200 points in the $V_{gate/bias}$-plane using an integration time of $t_{int} = 10\,\mathrm{s}$ can easily take more than 100 hours. During this time artifacts in the measurement can occur caused by refilling helium or by temperature changes in the room etc. Again it is advisable to find a compromise to not extend the measurement time too long while maintaining a reasonable resolution.
After the measurement, the file is imported into IGOR Pro and the data is treated as described in section 3.5.

5 New Signatures of the Franck-Condon Effect in the Noise

This main chapter contains measurement results of a carbon nanotube based quantum dot sample we investigated within our noise setup. Before coming to the actual measurement of current fluctuations an extensive characterization of the device is performed and will be presented in the first section.
In the subsequent section noise data obtained from a low transparency regime in our device is shown which exhibits interesting new signatures of Franck-Condon physics visible in the Fano factor. To the best of our knowledge this is the first time these features were observed in such a configuration. Our results will be discussed and compared with numerical model calculations[1] supporting our theses.

5.1 Electronic Sample Characterization

The device we were investigating in this work is shown in a colorized SEM micrograph in figure 5.1: a carbon nanotube, presumably single walled, CVD-grown on a SiO_2-covered p++-doped silicon chip is connected from top to metallic source (S) and drain (D) electrodes. A bias or source-drain voltage can be applied to alter the chemical potentials of source and drain μ_s and μ_d. To manipulate the chemical potential of the quantum dot itself, a gate voltage can be applied to the device via a global backgate. Additionally another gate electrode (G) is realized by depositing a metal finger close to the nanotube. The tube segment between the two metal contact electrodes, marked in figure 5.1 is the area where the quantum dot emerges. The separation between the electrodes is $L \sim 990\,\mathrm{nm}$, this sets the theoretically expected mean level spacing $\Delta\varepsilon$ of the dot according to [22, 36, 99] to

$$\Delta\varepsilon = \frac{h v_F}{2L} \sim 1.7\mathrm{meV} \tag{5.1}$$

with the Planck constant h and $v_F = 8.1 \times 10^5$ m/s, the estimated Fermi velocity for carbon nanotubes.

[1] Code provided by Michael Niklas, chair Prof. Dr. Milena Grifoni.

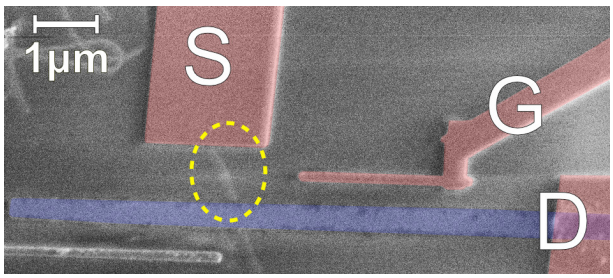

Figure 5.1: Colorized SEM micrograph of the device: a carbon nanotube with two metal contacts, source (S) and drain (D) deposited on top. The quantum dot emerges in a tube segment of length $L \sim 990\,\text{nm}$ between the S and D contact (yellow circle). A gate electrode (G) was defined in the vicinity of the tube.

5.1.1 Electronic Level Spectrum

For a first rough sample characterization at base temperature of T = 25 mK a fast wide range sweep of the gate voltage at zero dc bias while applying a small ac excitation of $V_{ac} \sim 10\,\mu V$ was performed. In this case the gate voltage was varied from -20 V to +20 V within a time of several minutes. This first test usually brings out the band gap (if any) and lets us roughly recognize the gate regimes which are interesting for us and are worth reviewing in detail.
In figure 5.2 such a wide range gate scan of our device is shown. The sample conductance reaches peak values up to $G \sim 0.13\,e^2/h$ and also features large areas with seemingly zero conductance along the gate axis. Note that in this plot one can not distinguish the real Coulomb peaks as the resolution is too low. The "peaks" visible here are regions with many Coulomb oscillations integrated by the fast measurement. Normally after such a first gate-trace one would focus on a smaller region and repeat the measurement with

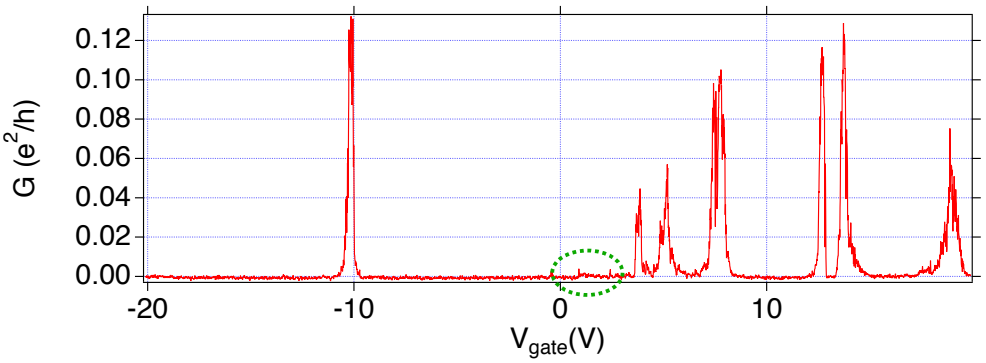

Figure 5.2: An initial fast gate-trace yields a first overview of the device's electronic properties. Peaks of high conductance as well as areas where the current is blocked are present in the large gate range $-20\,\text{V} \leq V_{gate} \leq +20\,\text{V}$. The region of interest for the following measurements is highlighted in green.

higher resolution and much slower, to really catch the sharp Coulomb peaks. In this case however we wanted to focus on a region close to the large blockage in the center in order to possibly capture the first few electrons after the potential band gap. In this region of interest (green circle in figure 5.2) the overall conductance was so small that most of the peaks at zero bias were hidden in the background noise. At that point we decided to directly acquire a full stability diagram around $V_{gate} = 2\,\mathrm{V}$.

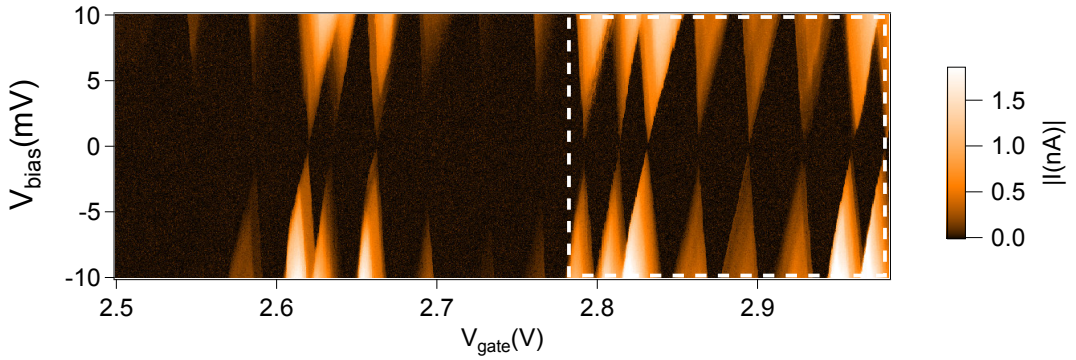

Figure 5.3: Stability diagram of current versus gate and bias voltage recorded in the low conductive region around $V_{gate} = 2.75\,\mathrm{V}$ (green in figure 5.2). The white dashed area will be investigated in detail in the following.

The stability diagram taken in this gate range (figure 5.3) showing the absolute value of the current versus gate voltage and bias, confirms that indeed Coulomb diamonds are visible in this area of very low conductance. The first clearly observable diamond edge coming from the left is located at around $V_{gate} = 2.6\,\mathrm{V}$ however faintly conductive areas still exist down to $V_{gate} = 2.5\,\mathrm{V}$. The pattern of diamonds looks far from regular at a first glance. For instance the slopes of the diamond edges are not parallel within a larger gate range and some diamonds seem to overlap at higher bias voltages. Also it appears that a superimposed modulation of the overall conductance leads to an alternating pattern of dark (low conductance) and brighter (higher conductance) areas along the gate voltage axis.
To learn more about this peculiar pattern we will now focus on the white dashed area in figure 5.3 where the conductance is high enough to resolve all diamonds also inside the darker sections in the diagram. Figure 5.4 shows a zoom into the white dashed section of the stability diagram in figure 5.3.

5.1.2 Energy Scales

A closer analysis of the diamond slopes in this range reveals that one can clearly distinguish two sets of Coulomb diamonds with different slopes and therefore two different energy scales. This observation indicates that two quantum dots are involved in the

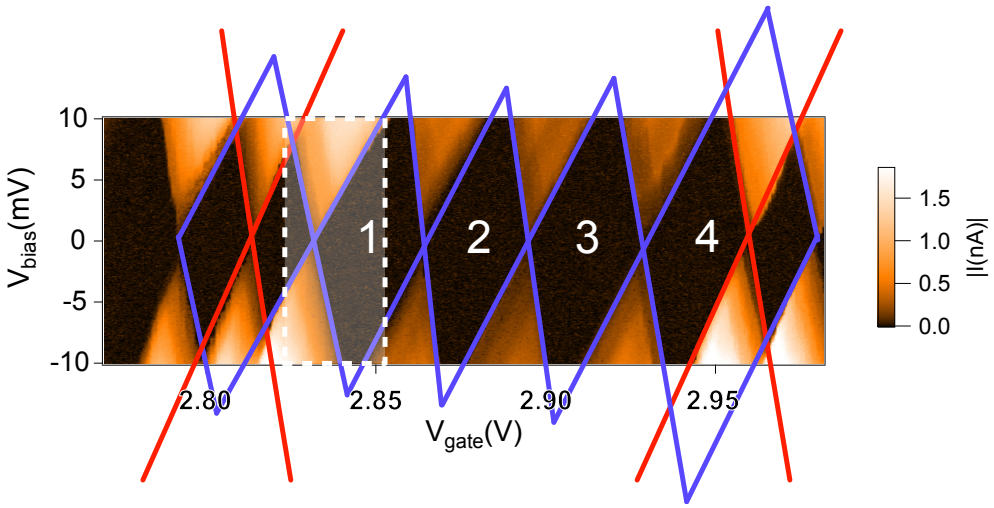

Figure 5.4: Zoom into the white marked area in figure 5.3. An analysis reveals two sets of different diamond slopes apparent in our device: a large dot highlighted in blue and a smaller dot (red). For later reference the four states in this area are labeled 1-4.

transport in our device exhibiting different energy scales which also means different geometrical dot sizes. In figure 5.4 these slopes are highlighted by blue and red lines. The blue lines trace the diamonds of a large dot, the edges and crossing points of the small dot are drawn in red. The energies of the red diamonds are roughly one order of magnitude higher than the blue ones, the measurement did not fully capture the entire red diamonds.

For that reason in figure 5.5 (a) the full size of the small dot is displayed as an overlay to the very same stability diagram of figure 5.3. The red lines have been extended to the point where the diamonds close. This image gives an idea of the different energy scales present in our device. A possible explanation for the presence of two quantum dots could be that the carbon nanotube on our is chip is not just one single CNT but a bundle of two (or more) tubes. Such a bundle is hard to discriminate from a single tube by means of electron beam microscopy alone which was the method of choice in the sample fabrication process.

If the size of the electronic dots L_{QD1} or L_{QD2} or even both are different than the geometric length of the tube L_{CNT} (see figure 5.5 (b)), a bias spectroscopy can produce such a pattern. However in our data the two quantum dots do not influence the electronic states of each other which would give rise to avoided crossings in the areas where the different species of Coulomb diamonds intersect as observed by Abulizi et al. [100] in a strongly coupled parallel double quantum dot. This lets us think of another possibility which is depicted in figure 5.5 (c): the two dots originate from the same tube induced

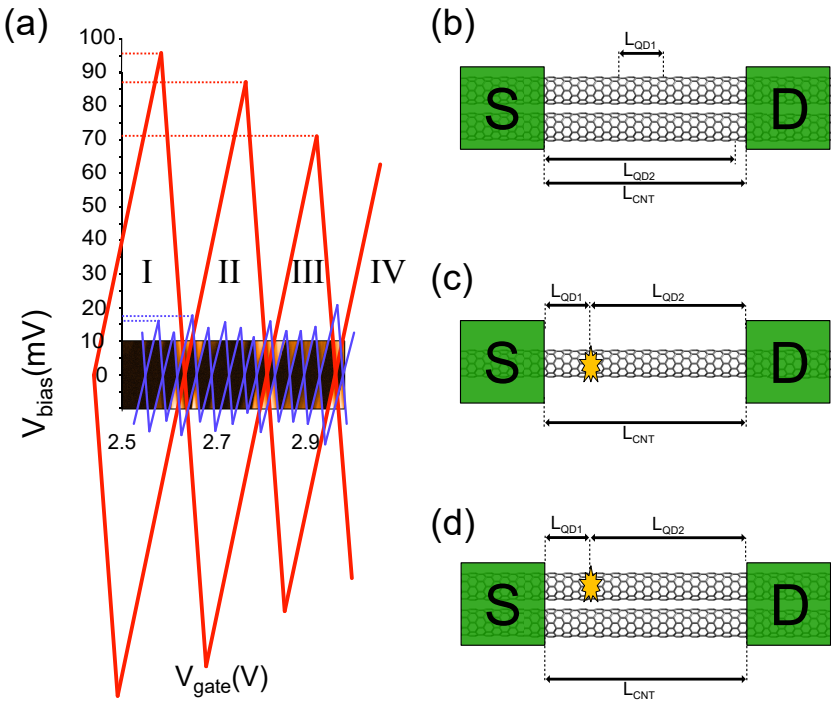

Figure 5.5: (a) Bias spectroscopy reveals two sets of Coulomb diamonds, i.e., two Coulomb diamonds on different energy scales, highlighted in red and blue. In the large dot (blue) the addition energies lie in the range of $10\,\text{meV} \leq E_{add} \leq 20\,\text{meV}$ while for the small dot (red) energies of almost one order of magnitude higher are observed. (b) One possible origin of the two quantum dots is that two carbon nanotubes are connected in parallel where on one (or both) of them the electronic dot size L_{DQ1} (L_{DQ2}) does not coincide with the geometric length of the dot L_{CNT}. (c) Another possibility is that impurities in the CNT split the dot into two smaller dots by introducing a local potential barrier. (d) A combination of scenarios (b) and (c). Two nanotubes in parallel where one of the tubes is divided into two serial quantum dots. The parallel tube is providing an additional transport channel which can enable residual conductance when the dot is blocked.

by a local doping[2] in the tube creating a potential landscape along the tube which splits the quantum dot into two dots of different geometrical size L_{QD1} and L_{QD2}, similar to applying a gate voltage via a central gate electrode in double dot experiments. Also the smaller dot (red) does influence the overall conductance through the device on a larger scale on the V_{gate}-axis, which is also an argument for two dots in series. An analogous serial configuration, but created on purpose in a semiconductor device, has been investigated for instance in [103] where a similar pattern of superimposed Coulomb peaks was observed. However our device is never blocked completely, a serial double dot configuration would allow conductance only at the so called triple points where the two dots

[2] A local doping in carbon nanotubes can for instance be caused by defects in the lattice structure, chemical impurities (adsorbates) or mechanical deformations like kinks [99, 101, 102].

are in resonance [19, 104]. Most probably the actual situation is a combination of the two scenarios mentioned before: two (or more) tubes in parallel with additional doping in one (or more) tubes, as in figure 5.5 (d). This explanation would fit to the missing avoided crossings and also explain the residual background conductance in the data.
Nevertheless, as for the upcoming analysis we will only focus on a very small section of the diagram (white dashed area in figure 5.4), we can assume that the serial resistance originating from the second dot is constant within this area and we can therefore ignore the small (red) dot and assume the large dot (blue) to be independent.
Though there is no clear fourfold symmetry apparent in the stability diagram, we label four states in the blue diamonds in figure 5.4 with numbers 1 to 4 for later reference and extract the slopes of the diamonds to be able to determine the gate conversion factor α_{gate} according to equations 2.21 and 2.23.
The slopes were extracted in the four charge states labeled in figure 5.4 and collected in table 5.1.

Charge state N	λ_s	λ_d	$\alpha_{gate} = (\lvert\lambda_s\rvert + \lvert\lambda_d\rvert)^{-1}$	Δ_{gate}	$E_C = \Delta_{gate} \times \alpha_{gate}$
1	1.92	0.625	0.39	0.0315 V	12.3 meV
2	1.92	0.470	0.42	0.0325 V	13.6 meV
3	1.96	0.560	0.40	0.0340 V	13.6 meV
4	1.94	0.635	0.39	0.0505 V	19.7 meV

Table 5.1: In this table the slopes of source- and drain SET lines, λ_s/d of the large dot (blue diamonds), are displayed for the four charge states 1-4 as labeled in figure 5.4. From these slopes the gate conversion factor α_{gate} is determined. From the distance of the Coulomb diamonds' crossing points on the V_{gate}-axis the addition energy for each state can be calculated by multiplying each value Δ_{gate}

As an average value for the gate conversion factor in the large dot we obtain

$$\overline{\alpha}_{gate} = 0.4.$$

We are now able to calculate the height of the corresponding Coulomb diamonds, the charging energy for the particular state E_C (see table 5.1). From the charging energy and the diamond slopes we can also give an estimate of the capacitances in our quantum dot. From the total capacitance of the dot, which is defined as $C_\Sigma = C_{gate} + C_s + C_d = e^2/E_C$ and the diamond slopes, given by $+\frac{C_{gate}}{C_\Sigma - C_s}$ and $-\frac{C_{gate}}{C_s}$ we calculate the following values for the capacitances:

$$C_\Sigma = 13.0\,\text{aF}, \qquad C_{gate} = 5.10\,\text{aF}, \qquad C_s = 3.19\,\text{aF}, \qquad C_d = 4.71\,\text{aF}.$$

Unfortunately due to the lack of a fourfold symmetry, it is hard to determine all the energies mentioned in section 2.2.4. One can give however an estimate of the level separation

regarding the differences of E_C for the neighboring diamonds:

$$1\,\text{meV} \leq \Delta\varepsilon \leq 7\,\text{meV}.$$

This energy span is in agreement with the expected shell spacing of $\Delta\varepsilon \sim 1.7\,\text{meV}$ for a quantum dot of length $L \sim 990\,\text{nm}$ (see equation 5.1).

As a comparison we want to show also the slopes $\lambda_{s,d}$ and the corresponding charging energies E_C for the small quantum dot in our device (red lines in figure 5.5). For the two states II and III indicated in figure 5.5 we were able to determine Δ_{gate} and calculate E_C:

Charge state N	λ_s	λ_d	$\alpha_{gate} = (\lvert\lambda_s\rvert + \lvert\lambda_d\rvert)^{-1}$	Δ_{gate}	$E_C = \Delta_{gate} \times \alpha_{gate}$
I	1.22	0.4	0.62	-	-
II	1.55	0.66	0.45	0.179 V	80.5 meV
III	1.52	0.58	0.48	0.145 V	69.6 meV
IV	1.7	0.83	0.35	-	-

Table 5.2: The slopes of source and drain SET lines, $\lambda_{s,d}$ for the charge states I-IV of the small dot (red diamonds) as labeled in figure 5.5. Only for II and III we were also able to determine Δ_{gate} and E_C.

The charging energies for the (geometrically) smaller dot are larger by approximately a factor of 6 to 7 compared to the small dot. Due to the lack of values for the crossing points of I and IV we were not able to determine Δ_{gate} and E_C for these states.

5.1.3 Coupling Asymmetry

Figure 5.6 shows a zoom into the positive bias part of the white dashed area in figure 5.4. Here the color scale represents the differential conductance dI/dV_{bias} instead of the current I. A step in current manifests as a line in dI/dV_{bias}, while a constant current leads to a vanishing differential conductance. Differential conductance can be either obtained by numerical differentiation of the current signal, or directly by means of a lock-in measurement. In our case dI/dV_{bias} was measured directly simultaneously with the current (see section 4.2). The amplitude of source and drain lines in the differential conductance are a measure for the coupling of the source and drain leads to the quantum dot. Extracting the peak heights on the source and drain lines in multiple cuts along the bias axis in intervals of $\Delta V_{sd} = 500\,\text{mV}$ allows us to give an estimate of the coupling asymmetry Γ_s/Γ_d by calculating the ratio of right/left peak heights. The lower panel of figure 5.6 shows one example of such a line cut where the left and right peaks were highlighted in green. The values which were obtained for the peak heights are presented in table 5.3. All values show consistent coupling ratios of $\Gamma_s/\Gamma_d \sim 0.3$ with two exceptions. These values are used later in the discussion as input for model calculations successfully reproducing our

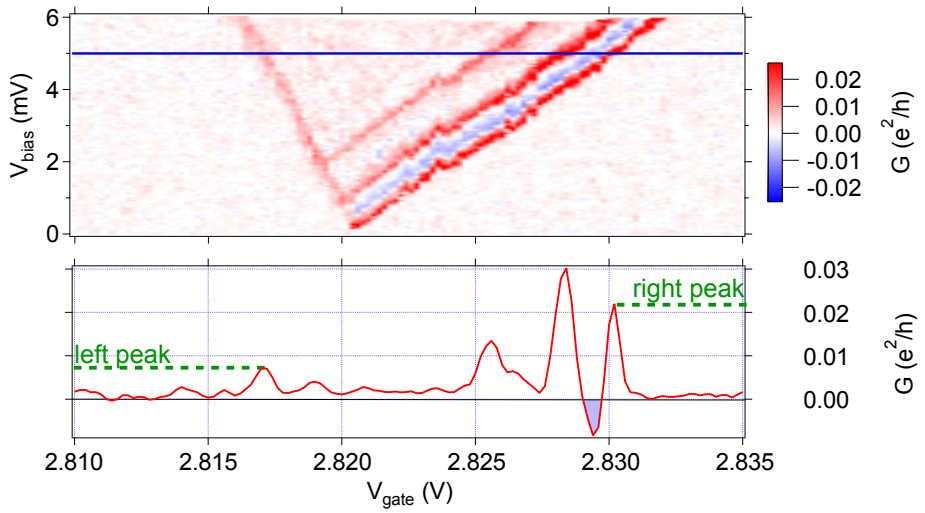

Figure 5.6: Upper panel: stability diagram of the white dashed area in figure 5.4 for positive bias, the color scale corresponds to the differential conductance in units of e^2/h. Several cuts along the gate axis for different bias voltages were analyzed with respect to the amplitudes of the left and right SET lines (source- and drain lines). The lower panel shows an example of such a cut for $V_{sd} = 5\,\text{mV}$. The values of the peak amplitudes for all cuts for $0.5\,\text{meV} \leq V_{sd} \leq 5\,\text{meV}$ with $\Delta V_{sd} = 0.5\,\text{meV}$ are shown in table 5.3.

measurement results. A determination of the total coupling strength $\Gamma = \Gamma_L + \Gamma_R$ would require an analysis of Coulomb peaks at zero bias which were not resolvable due to the low overall conductance in this gate regime.

V_{gate} (mV)	left peak (e^2/h)	right peak (e^2/h)	left/right
5.0	0.0072	0.022	0.327
4.5	0.0076	0.024	0.317
4.0	0.0067	0.025	0.268
3.5	0.0044	0.013	0.338
3.0	0.0064	0.020	0.320
2.5	0.0030	0.023	0.130
2.0	0.0030	0.020	0.150
1.5	0.0062	0.019	0.326
0.5	0.0056	0.018	0.311

Table 5.3: This table shows the extracted peak amplitudes for several cuts for $0.5\,\text{meV} \leq V_{sd} \leq 5\,\text{meV}$ through the stability diagram in figure 5.6. The conductance ratio of left and right peak corresponds to the coupling asymmetry Γ_s/Γ_d of left and right (or source and drain) leads to the dot. In our case this ratio is more or less constant around $\Gamma_s/\Gamma_d \sim 0.3$.

5.2 Excited States: Electronic vs Bosonic Modes

The following section will concentrate on excited states that we observed in the investigated regions in more detail.
As described in sections 2.2.3 and 2.2.4, excited states entering the bias windows in a quantum dot appear as steps in current or lines in the differential conductance. The dI/dV-plot in figure 5.6, which was discussed in the previous section exhibits peculiar features regarding excitations on the dot that also become important later in the noise analysis. On the right side of the plot very prominent excitations lines (drain lines) alternate between positive and negative differential conductance whereas the source lines are almost invisible. In the cut in the lower panel of figure 5.6 the region of negative differential conductance (NDC) is highlighted in blue. The fact that these excitation lines only occur in one direction is in agreement with the coupling asymmetry of $\Gamma_s/\Gamma_d \sim 0.3$ described in the previous section [105]. A complete conductance plot including the negative bias can be found in figure 5.7 (a). Due to the very low overall conductance in the region the contrast of the higher excitations is very weak and was therefore highlighted in (b). The energy difference between those lines projected on the bias axis is constant

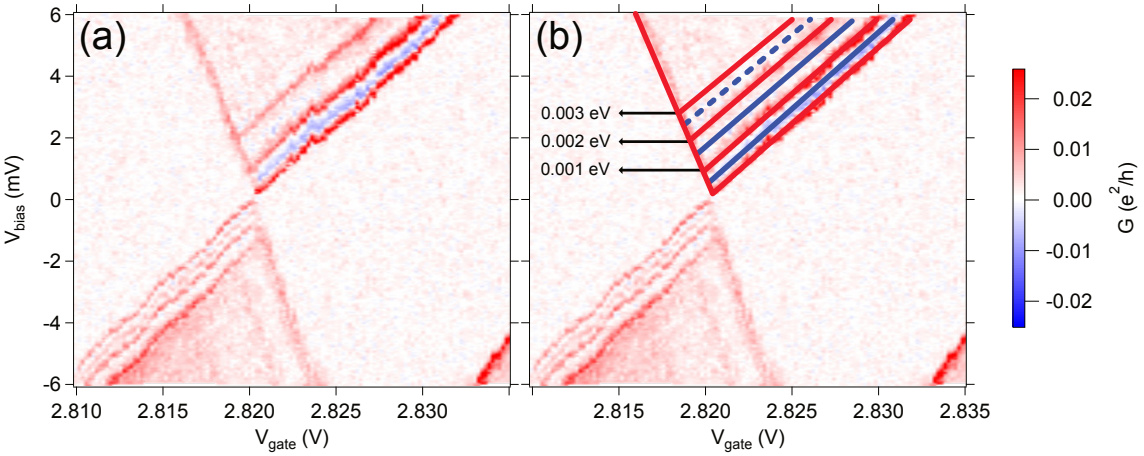

Figure 5.7: (a) The full stability diagram of conductance versus bias voltage and gate voltage taken in the white dashed area of figure 5.4. Several excitation lines running along the same direction, parallel to the drain SET lines, are visible already in this plot. Additionally a very prominent line of negative differential conductance (NDC) shows after the first drain line followed by a very faint area of NDC after the second drain line. In panel (b) the same plot is shown with additionally highlighted excitation lines (red) and NDC lines (blue). The excitation energies exhibit integer multiples of the first electronic excitation with $\Delta_{ES} \sim 1\,\text{meV}$.

and accounts for $\Delta E_{ES} \sim 1$ meV (see black arrows in figure 5.7). Compared to the energy scales present in this dot, ΔE_{ES} lies well within the range of $\Delta\varepsilon$, it is therefore possible that these excitations are of electronic nature. Compared to other works clearly showing electronic states [57, 106] the periodic pattern of excitation lines in our experiment looks

quite different. Also the appearance of negative differential conductance (NDC) between the positive (PDC) lines is unusual in these cases. It is therefore more likely that modes of bosonic origin in the tube are coupling to the electronic quantum dot giving rise to a harmonic spectrum in the conductance. In the work of Park et al. [81] such patterns were observed for a C_{60} molecule between two electrodes where vibrational modes in the molecule are visible in the transport. Later Sapmaz et al. [88] and Leturq et al. [80, 107] discovered similar features in suspended carbon nanotubes. Theoretical modeling by Yar et al. [89] showed that for very asymmetric coupling to the left and right lead in combination with the orbital asymmetry such spectra can be successfully reproduced for a carbon nanotube based quantum dot. Negative differential conductance can be caused by states on the dot which exhibit a longer relaxation time so that current is blocked for a certain time while the bias voltage is still increasing, leading to a step down in current as a function of bias voltage, and therefore negative differential conductance. Regarding the different vibrational modes accessible in a carbon nanotube, the energy scale where $\Delta E_{ES} \sim 1$ meV lies within the range of the longitudinal stretching mode of a suspended carbon nanotube. The stretching mode in a carbon nanotube can be expressed as

$$E_{stretching} = (nh/L)\sqrt{Y/\rho_m} \tag{5.2}$$

using the Young's modulus of a CNT $Y = 1$ TPa and $\rho_M = 1.3\,\mathrm{g/cm^3}$, the nanotube mass density. The radial breathing mode (RBM) is independent of the length and scales inversely with the tube diameter $E_{RBM} \sim 28\,\mathrm{meV}/d$. The bending mode energy is proportional to $\sim L^{-2}$ and much smaller than the excitations measured in our experiment [88, 108–111]. Figure 5.8 shows an energy comparison of RBM (green) and stretching mode (red) together with the mean electronic level spacing $\Delta\varepsilon$ (black) according to equation 5.1. The energy spacing $\Delta E_{ES} \sim 1$ meV would therefore correspond to the longitudinal stretching mode of a CNT with length $L \sim 110$ nm which does not fit to the geometrical length of our CNT ($L \sim 1\,\mu m$). Note that all these considerations were made for a suspended tube, in our case however the tube is lying directly on the substrate chip which should prevent the tube from moving. Yet it can not be excluded that parts of the CNT are suspended and not touching the substrate, and that only vibrations of a small section of $L \sim 100$ nm are coupling to the electronic dot. Differences in the size or spacial location of a vibrational dot and the coupled electronic dot are known and have been reported in [107, 112]. Harmonic excitation spectra can also originate from other configurations which give rise to bosonic modes. Photonic excitations, observed for instance in reference [113] can result in discrete resonance sidebands as well. Reference [114] reports on replicas of Andreev tunneling processes which are observed within the induced superconducting gap in a CNT based quantum dot where a superconducting contact is involved. In our device indeed one of the electrodes is made of rhenium which is superconducting up to a critical temperature of $T_C \sim 1.7$ K, however an induced gap was not found in our experiments. Another possible candidate could be plasma modes which have been discovered in superconducting millimeter size thin wires [115]. Standing wave

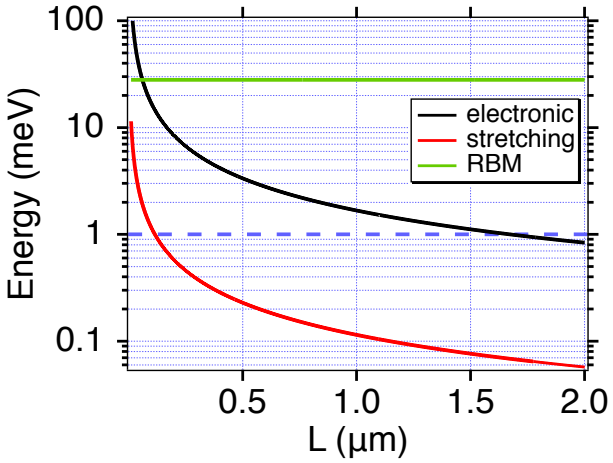

Figure 5.8: A comparison of the possible phononic excitation energies in a suspended carbon nanotube in dependence of the length of the suspended part. While the radial breathing mode (RBM) in green is constant with respect to the tube length and only proportional to the inverse of the diameter ($E_{RBM} \propto 28\,\text{meV}/d$), the longitudinal stretching mode (red) lies well within our experimental findings of Δ_{ES} with $E_{stretching} \propto 1/L$ (see equation 5.2). In black the mean electronic level spacing $\Delta\varepsilon$ according to equation 5.1 is plotted.

resonances of 1D plasma modes in a superconducting electrode of $L \sim 10\,\mu\text{m}$ (see figure 5.1), with resonance frequencies in the THz range could be compatible with our excitation energy of $\Delta E_{ES} \sim 1\,\text{meV}$. To further investigate possible plasma modes, an extensive analysis of micron scale rhenium wires with respect to their superconducting properties would be necessary, which is not subject of this work. The exact mechanism behind our observations of presumably bosonic modes remains unclear to date.

In the following an analysis of the excitations in our data regarding the Franck-Condon model (see section 2.4) will be presented which provides additional arguments for a bosonic scenario in our experiment and at the same time allows us to extract a value for the electron-boson coupling g from our measurement, which we will call electron-phonon coupling to stay consistent with other literature [88].

In figure 5.9 we present an analysis of the current versus bias characteristics in our device. In the stability diagram in (a) the equidistant steps in current are already visible. In (b) a line cut at $V_{gate} = 2.8214\,\text{V}$ is plotted as an example to demonstrate the step progression in the *I-V* curve. From this plot we were able to extract the normalized step heights in energy, labeled P_{1-4} for the four steps which were still resolvable. The green dashed line in figure 5.9 (b) represents a fit, as introduced in section 2.4 for the step height according to the Poissonian distribution

$$P_n = \frac{e^{-g} g^n}{n!} \tag{5.3}$$

for an electron-phonon coupling of $g = 1.8$. The extracted values for P_n as well as the calculated P_n for $g = 1.8$ are shown in table 5.4.

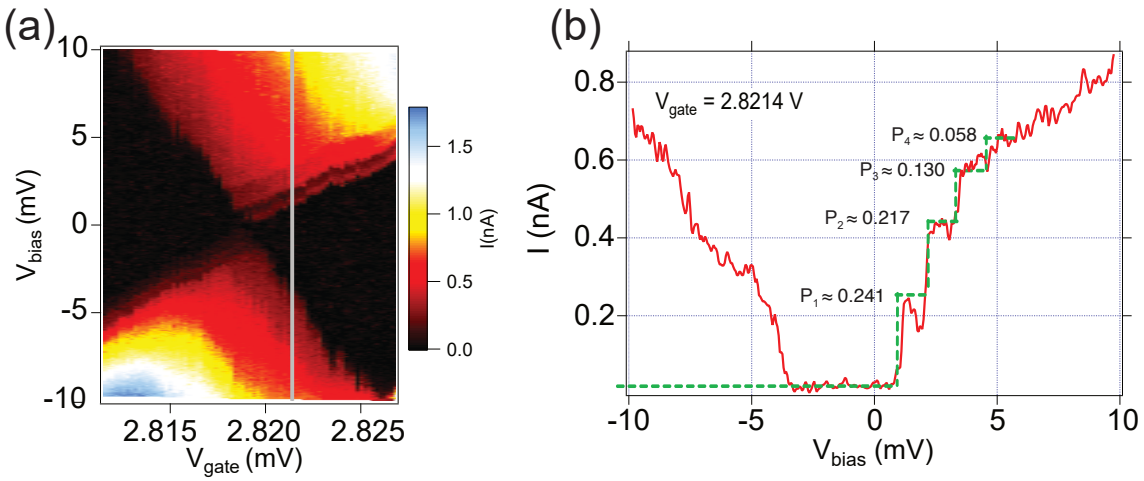

Figure 5.9: (a) Current versus gate and bias voltage of the same region as in figure 5.7. Current steps are clearly visible at positive bias. A line cut along the gray line in (a) at $V_{gate} = 2.8214$V is shown in (b). The current step heights fit the Poissonian distribution (equation 5.3) according to the Franck-Condon model for an electron-phonon coupling of $g = 1.8$ (green dashed line).

n	$P_n(g = 1.8)$	experiment
1	≈ 0.241	≈ 0.241
2	≈ 0.217	≈ 0.192
3	≈ 0.130	≈ 0.158
4	≈ 0.058	≈ 0.052

Table 5.4: Comparison of the calculated current step heights according to equation 5.3 for an electron-phonon coupling of $g = 1.8$. These values are in good agreement with the step heights extracted from the line cut in figure 5.9 (b).

An electron-phonon coupling of $g = 1.8$ is still reasonable when compared to other experiments [80, 88, 116, 117] and theoretical works [89, 118] and can be used as a starting point for model calculations later.

If the electron-phonon coupling is strong ($g \gg 1$), a suppression of the lower excitations is the consequence. Already for $g = 2$ the first and second step have the same height ($P_1 = P_2$), for even higher g the the first steps are suppressed even more. This effect can lead to a blockade in the transport at low bias voltages which is known as *Franck-Condon blockade* and was observed for instance in references [80, 82, 83, 107].

In the forthcoming section we will present noise data taken at the very same region as shown in this section. The goal is to be able to use noise measurements as an independent method to probe the mechanisms behind the transport in our system.

5.3 Shot Noise Measurements

So far we have only concentrated on the transport characterization of our device. Also the data presented so far was only recorded without capturing additional noise data since the main objective at the beginning of an experiment on quantum dots is to characterize the device to such an extent that one can decide if the sample is worth further investigations.
Our transport data shows interesting features, that is two quantum dots in the same device in very different energy scales, equidistant, harmonic excitations which obey the Poissonian progression of step heights in current which we analyzed within the Franck-Condon model. Together with strong signatures of a negative differential conductance between the excitation lines we attributed these features to boson assisted processes in our device giving rise to multiple replicas of electronic excitation features. Possible explanations are standing wave resonances of 1D plasmon modes in the superconducting contact on our nanotube or the hypothesis that only a short segment of our tube is suspended and therefore able to oscillate, providing an electron-phonon coupling large enough to be detectable in our measurements.
Since our measurement setup is capable of detecting current fluctuations (noise) as well as transport data in the same run (see chapter 3), we now want to acquire noise data in addition to the current in the same regions as before and use this data as a complementary tool to confirm our previous assumptions and learn more about the mechanisms behind our observations. We expect that boson assisted processes which cause channel blocking and give rise to negative differential conductance are also visible in the shot noise as super Poissonian noise [82]. Due to the long integration time per pixel needed in the noise measurement, a compromise between resolution and measurement time has to be found. Acquiring the corresponding current fluctuations for all the diagrams seen before would be too time consuming. We have to focus on the most interesting sections of our stability diagrams, which is the positive part of the region shown in figure 5.7. With an image size limited to 120 x 200 pixels and an averaging time of t = 10 s per pixel including additional breaks and the time required for sweeping the measurement devices back to the start values after finishing one bias trace, such a measurement run can already take up to 100 hours.
Note that because of this significantly longer time required by the noise averaging during the measurements, the quantum dot is more prone to gate shifts caused by spontaneous charge fluctuations. For that reason the V_{gate}-axis in the following data may sometimes not exactly correspond to the previous data which was recorded faster and also days or weeks before the data shown in this section. In addition, smaller gate fluctuations during the measurement can lead to distortions like “fringes” visible for instance at the edges of the Coulomb diamonds.
Figure 5.10 shows an example of one of the first sets of data obtained in a our setup (see section 4.2.2) in the same low transparency regime around $V_{gate} = 2\,\mathrm{V}$ discussed in the

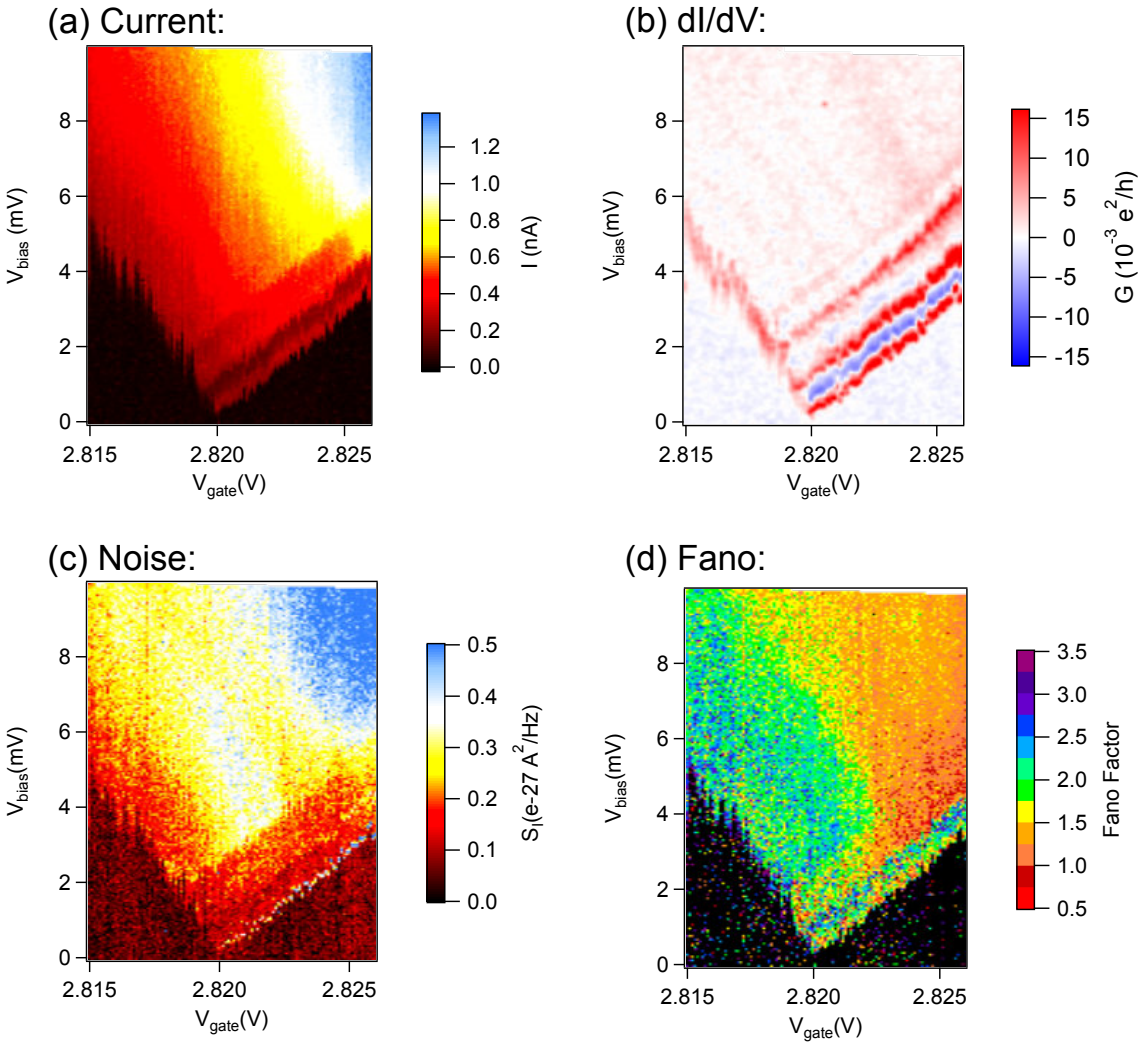

Figure 5.10: A comparison of different data obtained simultaneously in a single measurement. The plots show dc current (a), differential conductance (b), voltage noise (c) and the calculated Fano factor (d) stability diagram segment. Super Poissonian noise is present all over the plot, especially enhanced along a line of negative differential conductance.

previous sections. The data was acquired and processed as described in section 4.2. Dc current I (a), differential conductance dI/dV (b), current noise S_I (c) and the Fano factor $F = S_I/2eI$ calculated from S_I and I (d) is plotted as a function of gate and bias voltage. Already in panel (a), similar to figure 5.9, excited states are visible as steps in the current including a darker line in the lower right corner of the plot, a step down in current indicates a region with negative differential conductance, which is also very prominent in panel (b) as a blue, negative line. The current noise S_I in panel (c) however does not follow this behavior, it remains flat. This means that the calculated Fano factors in the "Fano map" (d) have increased in this area. The Fano factors in this regime reach su-

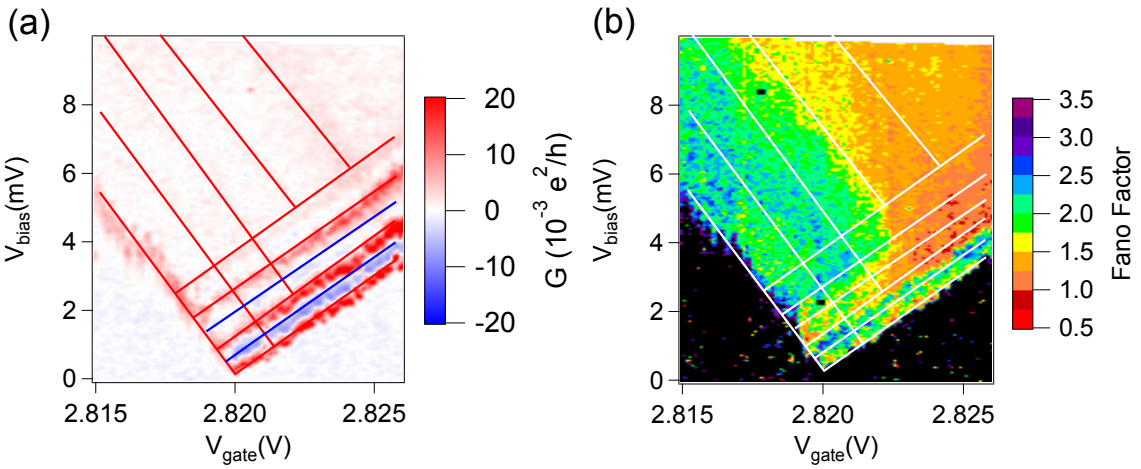

Figure 5.11: Differential conductance (a) and Fano map (b) of the same region as shown in figure 5.10. An overlay of red and blue lines in (a) emphasizes the location of excited states with positive (red) and negative (blue) differential conductance. The same lines superimposed on the Fano map (b) mark the borders of regions of discrete Fano factors.

per Poissonian values of $F \geq 1.0$ all over the diagram. To illustrate the areas of different Fano factors and to compare the noise data with the conductance, in figure 5.11 (a) blue and red lines are displayed on top of the original conductance plot as a guide to the eye. Exactly the same (but white) lines are shown as an overlay to the Fano map in (b). The map also points out that the white lines which correspond to the excited states in many areas of the plot act as "borders" between areas of different Fano factors. On the first NDC line a ridge in the Fano map emerges which is clearly higher than in the surrounding areas. On this ridge the Fano factor can reach values up to $F \approx 3.0$. In addition we observe increased noise in the area at the left side of figure 5.11 (b) parallel to the source lines. This area also shows an internal structure: coming from the source side the noise remains constant at $F \approx 2.0$, before it drops down to $1.0 \leq F \leq 1.5$.
Apart from calculating a map for the Fano factor by matrix division as it is done in figure 5.10 (d), there is also a different way of visualizing noise data. It can be realized by rescaling a noise plot as in figure 5.10 (c) such that instead of the bias voltage, the ordinate is representing the current through the dot. In this way, a line cut parallel to the current axis directly shows the function

$$S_I = F \cdot 2e\langle I \rangle$$

with the Fano factor F as the slope, the well known *Schottky formula*. Local changes of the slope along the line plot represent a local Fano factor in the data. Sometimes a plot like this may reveal features which are hidden in a Fano map like in figure 5.10 (d). Such a representation of noise data is shown in figure 5.12. On the left side current noise S_I is plotted as a function of the gate voltage and the current through the dot. The image is not complete as certain areas are not defined due to the lack of data when the matrix

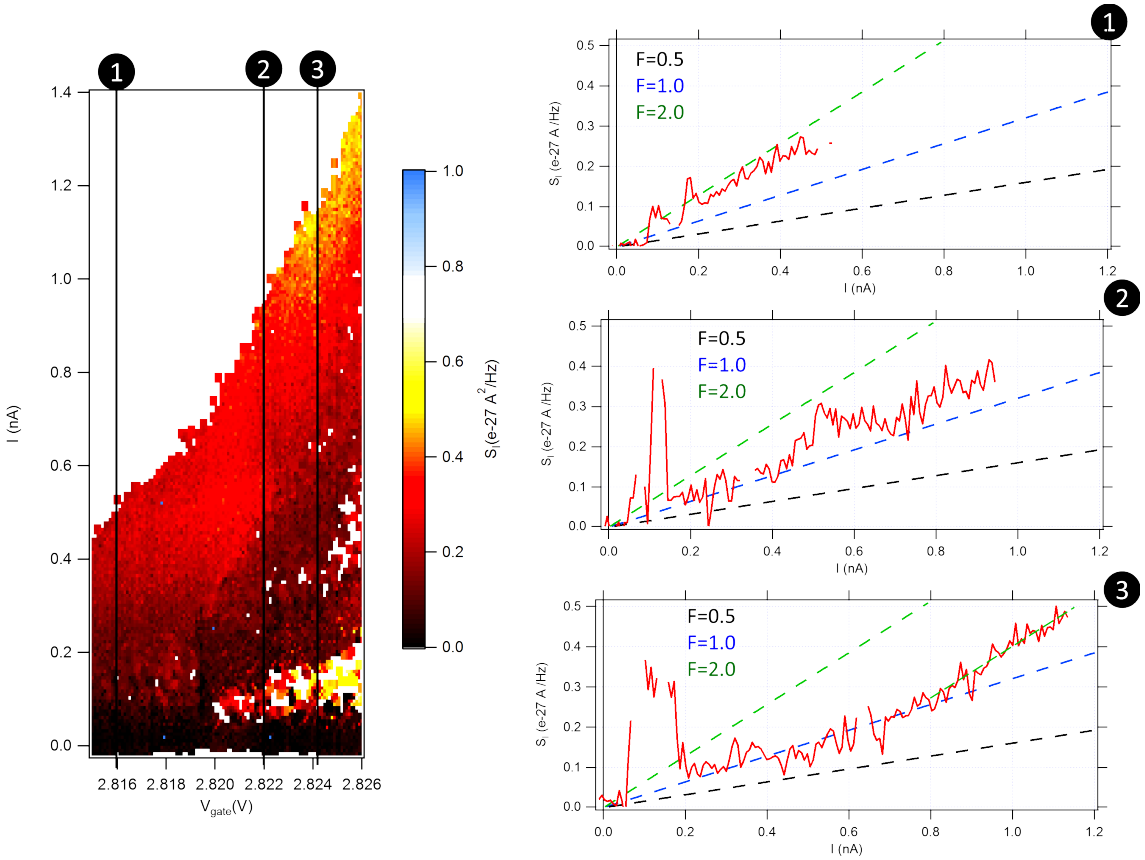

Figure 5.12: A different representation of noise data: on the left side current noise S_I is plotted versus gate voltage V_{gate} and current through the system. The right panels display three line cuts along the black lines indicated by 1,2,3 in the left panel. The slope of the line cuts directly show the Fano factor according to the Schottky-formula. Changes of the slopes along the cut correspond to local changes of the Fano factor. As a guide to the eye dashed lines in the right panels visualize $F = 0.5$, $F = 1.0$ and $F = 2.0$.

is rescaled to current. In other words, for some of the noise values there is no data for the corresponding current, which leads to such truncated image plots. On the right side of figure 5.12 line cuts labeled 1, 2 and 3 through the corresponding black lines in the left panel are shown. All three line plots exhibit discrete values for the slopes $F = 1.0$ or $F = 2.0$ and some peaks at lower bias which correspond to the ridge of increased Fano factor along the NDC line in the "Fano maps" in figures 5.10 (d) and 5.11 (b). The local slopes here largely exceed the calculated Fano factors in these regions seen in the previous graph. The number of data points however is not large enough to further evaluate the local slopes. For this particular gate regime the latter way of displaying the Fano factor does not bring much more information than the usual Fano maps. However it is a nice way of expressing the Schottky formula in a graphical way and a proof that our noise detection setup is working correctly and the calibration was done properly since S_I

increases linearly with the current through the sample while the slope approaches distinct values for the Fano factor throughout the map.
In the following we want to compare our data with theoretical model calculations similar to reference [89], considering phonon assisted tunneling processes in a suspended carbon nanotube. In addition to current and conductance, noise calculations according to reference [90] were included. The code which is implemented in Matlab was provided by Michael Niklas from the theory group of Prof. Dr. Milena Grifoni, a brief explanation of its underlying theoretical model can be found in section 2.5. The program is able to calculate the populations on the quantum dot, as well as the current and the corresponding shot noise or Fano factor. From the electronic characterization of our device and the fitting to the Franck-Condon model in sections 5.1 and 5.2, we were able to determine various values which we can now use as initial parameters for the numerical calculations: the temperature $T = 25\,\mathrm{mK}$, the phonon energy of $E_{ph} \sim 1\,\mathrm{meV}$, the coupling asymmetry $b = \Gamma_s/\Gamma_d \sim 0.3$ and the electron-phonon coupling of $g \sim 1.8$, actually the code is using two separate parameters for the electron-phonon coupling to the source and drain leads called λ_L and λ_R. Free parameters are the relaxation times for electrons and phonons τ_{el} and τ_{ph} respectively, the sub-band mismatch Δ and the orbital asymmetry a which, according to [89], needs to be large to achieve the NDC/PDC pattern observed in our transport data. Due to the many free parameters the simulation process was very time consuming, the calculation itself as well as the manual adjustment of many parameters before each simulation was quite challenging. In the end the parameters listed in table 5.5 turned out to give the best results in terms of matching our experimental data.

parameter	T (K)	λ_L	λ_R	a	b	τ_{ph}	τ_{el}	E_{ph} (meV)	Δ (meV)
value	0.025	1.8	2.0	10	0.34	0.7	5	0.85	0.36

Table 5.5: The parameter set used for the simulations shown in figures 5.13, 5.14 and 5.15.

In figure 5.13 a comparison of experimental data and the results of our simulation using the parameters in table 5.5 is shown. The experimental data for current and Fano factor in panels (a) and (b) is the same as in the previous section. The simulation data for the current in panel (c) nicely reproduces the steps in the current as well as some of the areas with negative differential conductance. The corresponding Fano map in panel (d) shows the highly enhanced noise in on the left side parallel to the drain line as well as the block of high Fano factor on the right side. Even the internal structure of this areas resembles the experiment. Additionally the strip of lower Fano factor separating these regions could be achieved quite well (green dashed areas in figure 5.13 (b) and (d)) including the lower bias part where the current is slightly suppressed, here the Fano factor is again higher. Of course image plots like figure 5.13 are often not suitable for a quantitative comparison as small deviations are not visible in the color scale. Therefore we want to present also line cuts through the image plots seen before taken at several gate voltage values in figure 5.14. Experimental data is plotted in red, simulations in blue. The left

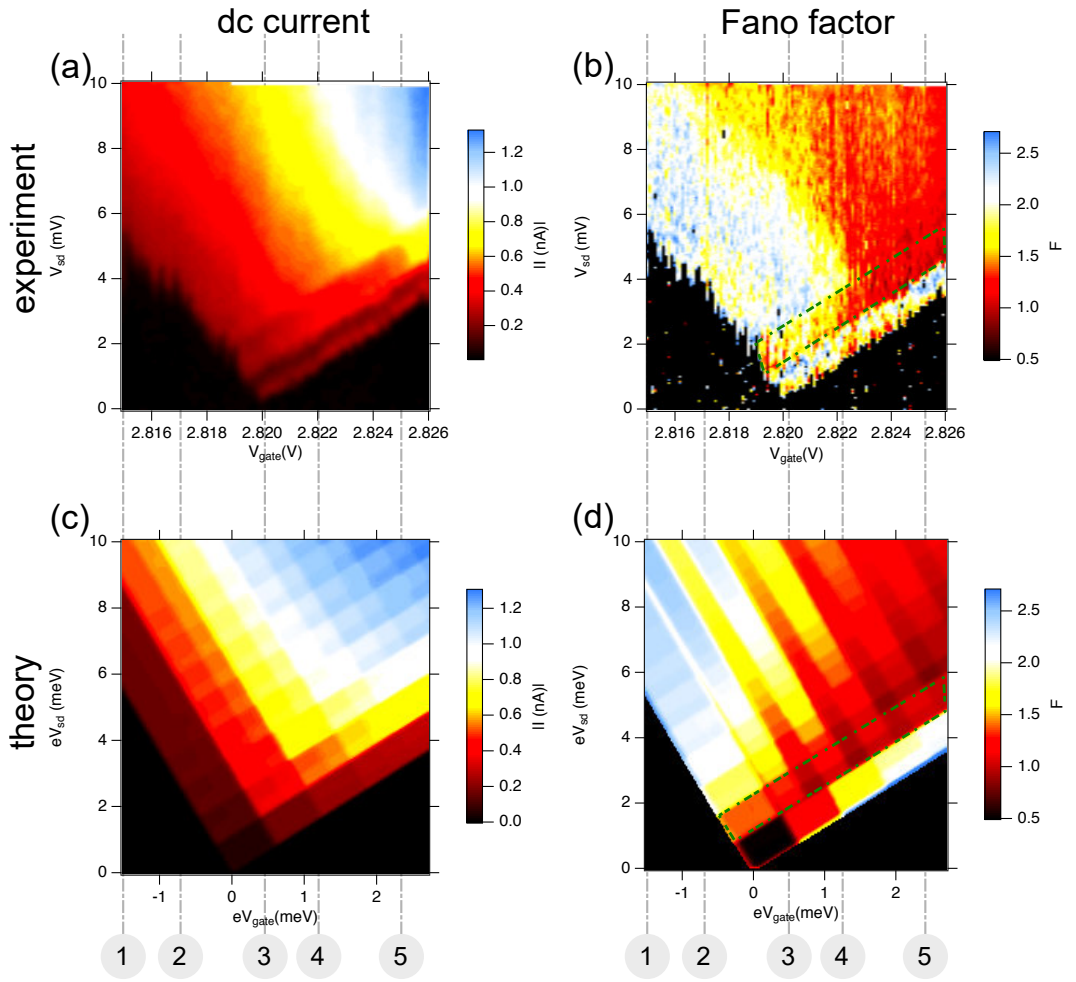

Figure 5.13: Comparison of experimental data and numerical simulations for dc current and the Fano factor. The model is capable of reproducing current steps and magnitude (a,c) and also the Fano factor (b,d). Two areas of enhanced Fano factor including their internal structure could be successfully simulated by the underlying model. The numbers on the bottom indicate the positions where we produced the line cuts presented in figure 5.14.

panel compares the dc current at the gate voltages indicated in the plots. A comparison of the Fano factor can be found in the right panels. The third cut at $V_{gate} = 2.820\,\mathrm{V}$ is taken at the crossing point of the Coulomb diamonds which corresponds to $eV_{gate} = 0\,\mathrm{meV}$ in the image plots of the simulations. Hence the plots labeled 1 and 2 are taken at the left side of the map, plot 4 and 5 on the right side. It is noticeable that the fitting on the center and right side of the stability diagram (plot 3 to 5) seems to work much better than on the left side, especially the noise plots are on top of each other.

Plots 3,4 and 5 exhibit a similar progression of step heights in the experimental data (red) as shown in section 5.2. Compared to image 5.9 the plot is slightly different since the data does dot originate from the same measurement run therefore the positions of

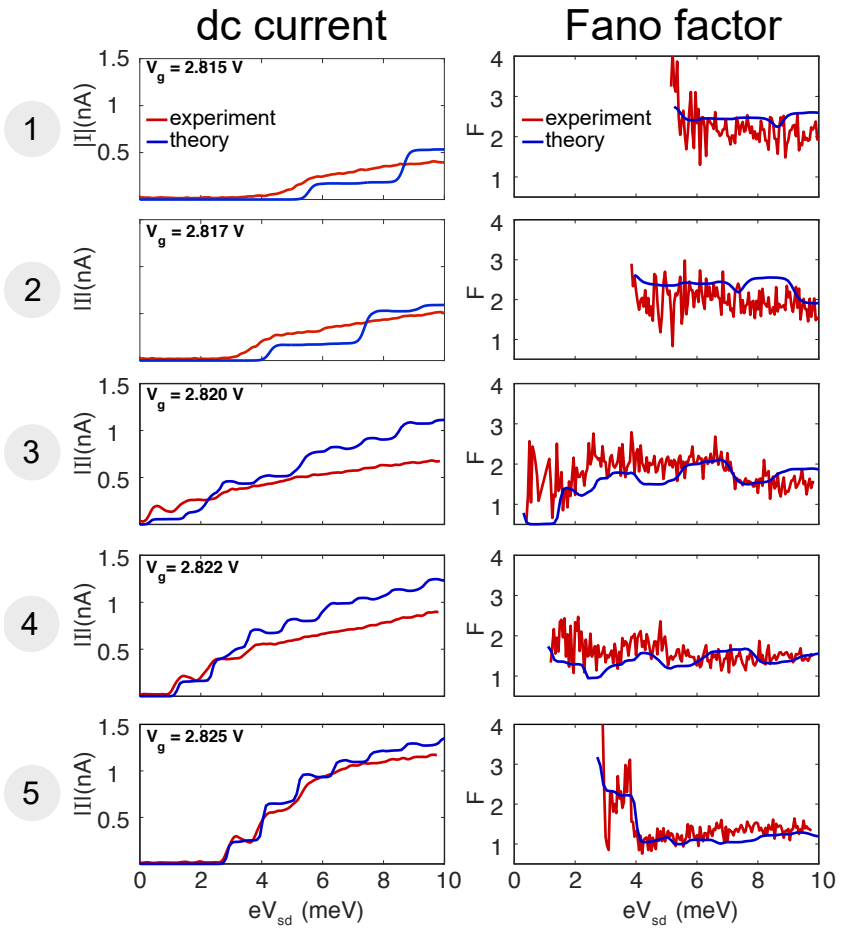

Figure 5.14: Comparison of theory (blue) and experimental data (red): several line cuts for dc current and Fano factor along the stability diagram and Fano map of figure 5.13. The numbers on the left side correspond to the numbers in figure 5.13 which indicate the position where the cuts have been taken.

the diamond with respect to the absolute gate voltage is shifted. However also in this measurement the step heights in the cuts 3, 4 and 5 are compatible with an electron-phonon coupling of $g \sim 1.8$. Whereas the current traces in plots 1 and 2 exhibit much sharper steps than seen in the experimental data where basically only the first step is visible and then the current increases smoothly. Since only the first current step was observable the Franck-Condon model can not be applied here. Deviations between the simulations and our measurement data become also apparent when we look at the comparison of the differential conductance data versus calculations in figure 5.15. In the experimental data the damping of higher oscillations is much faster than in the simulations. For the drain lines we only observe the first three lines, at the source side only very faint excitations are visible, as opposed to the simulations which exhibit a rich pattern of excitations along the entire bias range. Of course one can further increase the phonon

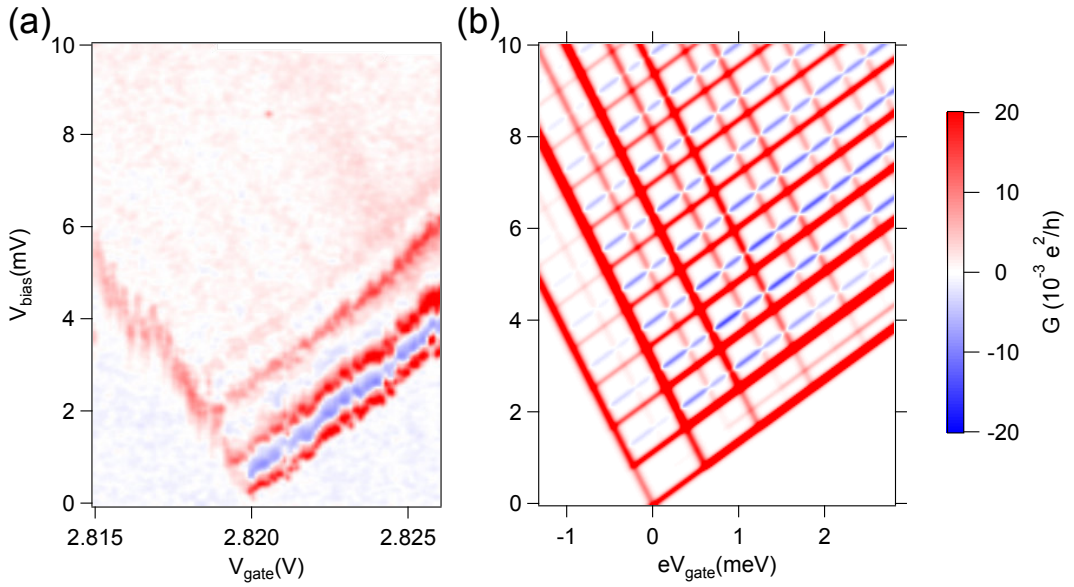

Figure 5.15: Experimental data (a) and numerical simulations (b) of the differential conductance in the same region as the data shown in figure 5.13 and 5.14. The overall pattern of excitation lines could be well reproduced. However the lowest line of negative differential conductance is not present in the simulations, also the damping in the simulation is much lower, giving rise to a richer structure at higher energies compared to the experimental data.

damping in the code, but then the noise in the Fano map becomes completely flat without any internal structure. Furthermore we were not able to reproduce the first NDC line in our simulations without losing the consistency in noise, which indicates that there are mechanisms behind this feature which are not covered by our model at this point. Negative differential conductance is a well known phenomenon in quantum dots in general and does not necessarily depend on bosonic modes but can also be caused by asymmetric coupling alone [119, 120]. Nevertheless it should be pointed out that the noise structure and magnitude in figures 5.13 and 5.14 cannot be reproduced without including electron-phonon coupling into the model. Excluding phonons renders the Fano factor completely flat and sub-Poissonian throughout the entire diagram. The areas of strongly super Poissonian Fano factors, which are linked to negative differential conductance and which we were able to successfully reproduce within our simulations can be associated with channel blocking in the quantum dot: one or more lower states on the dot can feature a longer lifetime ($\tau_1 > \tau_0$) than energetically higher states (see figure 5.16), transport through the dot is blocked. After $t = \tau_1$ charges can tunnel out of this state again followed by a release of a series of tunneling events from the higher states out of the dot. Then again the slow channel is blocked for a time period of $t = \tau_1$. This alternating pattern of blocked current followed by an avalanche like release of charge carriers (figure 5.16) leads to a high variance in the current $I(t)$, and thus an increase of noise and Fano factor.

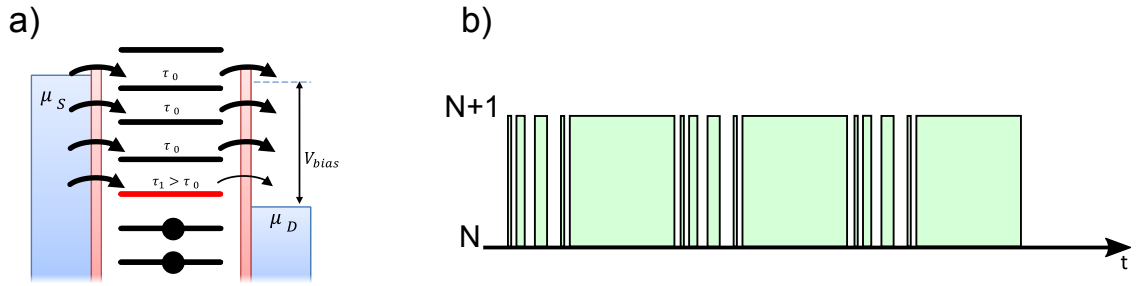

Figure 5.16: Channel blocking in a quantum dot: a state on the dot with a longer lifetime $\tau_1 > \tau_0$ (indicated in red) is preventing other electrons from tunneling off the dot. The population is blocked at N+1 which results in a blocking of current followed by a series of tunneling events after the break and so on. This sequence leads to an increase of variance in the current thus an increase of noise.

In our device probably a combination of very asymmetric coupling of the different orbital states [65–67,89,121] and Franck-Condon blockade can be held responsible for slow channels (see section 2.4): when the bosonic ground state wave functions for two consecutive electronic energy levels exhibit smaller overlap than higher excited phonon states, the tunneling rates for these transitions can be reduced. Current is suppressed, even when the energy provided to the dot (bias and/or gate voltage) does increase, resulting in negative differential conductance. In these regions electrons are released in bunches with periods of no current in between (see figure 5.16), leading to a high variance in the current and thus a high Fano factor [82]. When the bias voltage is increased and matches an integer multiple of the phonon energy $E_{ph} = \hbar\omega$, conductance through the dot is enhanced leading to an equidistant spectrum of excitation lines. Such a scenario is in agreement with our numerical simulations and consistent with the Franck-Condon model (equation 5.3).

We can therefore conclude that we have strong evidence for the existence of bosonic modes in our device which give rise to the harmonic spectrum we observed in our data. Not only is the step height analysis based on the Franck-Condon model in good agreement with our observations, but also our noise data combined with theoretical calculations as an independent means supports our hypothesis. Since our model, which is considering phononic modes in carbon nanotubes clearly does not reproduce all features in our experiments, additional mechanisms which are not covered by our simulations, like for instance the 1D plasma modes [115] already mentioned in section 5.2 may also play a role. However, since most of the features in our simulation, especially in the shot noise are closely tied to phononic modes and cannot be achieved without them, we can comfortably exclude a purely electronic configuration in our quantum dot. Shot noise analysis has therefore proven a very useful means to study charge transport independently from standard transport measurements.

5.4 Chapter Summary

In this chapter we have demonstrated a new method to identify the origin of a peculiar excitation spectrum we observed in a non-suspended carbon nanotube based quantum dot. In a first bias spectroscopy measurement we found a regular sequence of Coulomb diamonds which were superimposed by a second set of much larger diamonds which act as a modulation of the background conductance for the smaller diamonds. We attributed this observation to a second, much smaller quantum dot formed in series to the first dot. As a possible reason impurities in the tube can be suspected. Due to the minor influence of the second dot, only the first dot was investigated further as it was considered independent. Higher resolution bias spectroscopy in the large dot revealed a series of excitations which are equidistant in terms of energy with a spacing of $\Delta E \sim 1$ meV. In addition an alternating sequence of positive- and negative differential conductance occurred in the stability diagram. These energy scales however hardly fit the geometrical size of the dot which we know from scanning electron microscopy. We therefore attributed these excitation to boson assisted tunneling in our carbon nanotube. Because the tube is non-suspended and lying on the substrate chip, a vibronic scenario might seem counterintuitive, but a detailed analysis of the current steps employing the Franck-Condon model (see section 5.2) gives a strong argument in favor of bosonic modes. Additionally other boson assisted processes are thinkable as for instance standing wave resonances of 1D plasmon modes in one of our contact electrodes.
We were then using our noise setup to acquire noise data at the same charge states investigated before in the transport. In the shot noise data we found areas of highly enhanced Fano factors which is unusual for a purely electronic single quantum dot. These areas are often connected to the lines of negative differential conductance already seen in the transport data. Numerical simulations including vibronic excitations succeeded in reproducing most of the features observed in the experiment. These features are dependent of the vibronic excitations and can not be achieved in the simulations with electronic excitations alone. This means that additionally to the Franck-Condon analysis in section 5.2, we have an independent proof of vibronic or generic bosonic excitations existing in our device. With the help of numerical model calculations by the theory group of Prof. Milena Grifoni we were able to identify bosonic excitations in a carbon nanotube based quantum dot by means of noise analysis along a stability diagram of a quantum dot as a complementary method.

6 Summary and Outlook

The present work was aiming at the establishment of a state-of-the-art setup for shot noise detection at low temperatures. The system should be included in our already working cryostat system with base temperatures down to $T \approx 25\,\mathrm{mK}$. Additionally first measurements with the system using sophisticated on chip quantum dot devices based on carbon nanotubes should both prove the functionality of our system and also help us to understand more about the charge carrier kinetics in these devices.

The noise detection setup we planned as a twofold amplifier setup based on resonant enhancement of current fluctuations using a passive RLC circuit directly at the sample holder, a distributed two stage amplifier chain with pre-amplification at $T = 4.2\,\mathrm{K}$ and a second amplifier at room temperature amplifies the signal. The sensitivity of our setup is in the range of $S_I \approx 10^{-30}\,\mathrm{A}^2/\mathrm{Hz}$. Our newly developed measurement software in Perl (Lab::Measurement) together with the data processing routines implemented in IGOR Pro allows for automated unattended long-term measurement runs of several days or even weeks.

The system was designed with interchangeable custom-built printed circuit boards as sample holders which also include the RLC circuits and is therefore capable of dealing with many different types of experiments. With the twofold amplifier configuration it is possible to either increase the noise resolution by canceling out spurious noise coming from the amplifiers, but also cross correlation experiments with multi-terminal devices are applicable.

After accomplishing the construction of our setup, a calibration procedure by means of examining a quantum point contact device (QPC) revealed the functionality as well as the overall gain we can achieve with it, which was highly satisfying. The noise detection setup was ready for real measurements.

The first device which we investigated within the aforementioned system was a carbon nanotube based quantum dot: a CVD-grown carbon nanotube lying on a substrate chip with metallic contacts deposited on top of it, forming a quantum dot in a tube segment. A metallic side gate was deposited in the vicinity of the tube to apply an electric field and thus shift the energy levels on the dot. First an extensive sample characterization at low temperatures by means of bias spectroscopy was performed. From modulations in the overall conductance we found that two serial quantum dots of different energy scales were present in our device. In the transport data we also encountered a peculiar

excitation spectrum which we supposed to be of non purely electronic nature. A further analysis with respect to Franck-Condon blockade substantiated our conjectures.
After the transport characterization we started to acquire noise data which we processed and evaluated after the experiment. We found super Poissonian noise enhancements which are obviously connected to the excitation pattern we observed in the transport. With the help of numerical model calculations by the theory group of Prof. Milena Grifoni, including vibrational modes in a carbon nanotube, we were able to identify bosonic excitations in a carbon nanotube based quantum dot by means of noise analysis along a stability diagram of the dot, as a complementary method next to standard transport investigations. So far we associate these excitations with a segment of our nanotube being suspended and can therefore be prone to mechanical modes or other bosonic mechanisms. This is to the best of our knowledge the first time that bosonic excitations in a carbon nanotube quantum dot were revealed in the shot noise.
For the future, further improvements of the noise setup are planned. Rather than mounting and wire bonding sample chips directly onto a printed circuit board, a redesign of the sample holder is planned which makes the setup compatible with the standard 20 pin LCC chip carrier we are using in other setups. We will then be able to investigate samples which have been pre-characterized in a different system. Also the problems with background noise (spikes) we observed in our measurements (see section 3.5) could already be eliminated by moving the setup into a new lab.

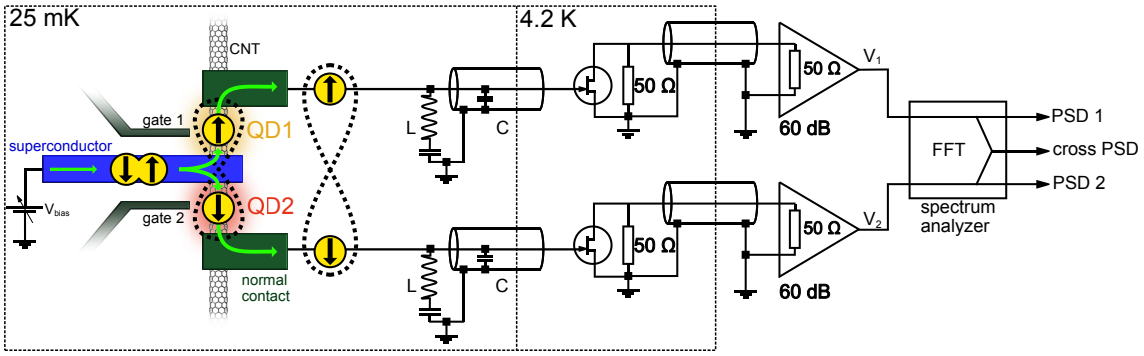

Figure 6.1: Carbon nanotube based Cooper pair splitter device: supercurrent is injected via a superconducting central contact (blue) into a CNT double quantum dot, which when in resonance is able to split incoming Cooper pairs into two electrons with opposite spin. The electrons are entangled as a superconducting electrode acts as a natural source of entangled electrons. Measuring cross correlation at the two outer normal leads (green) using a twofold amplifier setup can prove electron entanglement.

As a main future perspective cross correlation experiments on superconductor-hybrid devices like carbon nanotube based *Cooper pair splitters* are in the planning stage. Such measurements are proposed for instance in [122]. The measurement technique would be related to references [18, 21] but using carbon nanotubes with a superconducting con-

tact electrode forming a double quantum dot to split Cooper pairs into two electrons of opposite spin. The electrons' quantum mechanical entanglement is sustained and can be detected by means of positive cross correlations in a twofold amplifier setup. Such a setup is shown in figure 6.1: a carbon nanotube with two outer normal metallic contacts and one central superconducting electrode acting as a Cooper pair injector. When the two dots are in resonance the Cooper pair can be split into two entangled electrons with a certain probability. Such experiments have been already performed in the past [19]. However a certain prove of the entanglement is still challenging. By using our setup to detect noise at the two outer contact electrodes and directly compute the cross correlation, a prove of electron entanglement lies within the bounds of possibility.
In the end we can conclude that our newly developed and constructed noise detection setup together with numerical simulations has already proven to be capable of providing an additional tool for investigating specific transport mechanisms. For the first time we were able to detect vibronic excitations in a carbon nanotube by means of shot noise detection. With this setup, our low temperature system is now equipped with state-of-the art technology for investigations of current fluctuations, which opens up new possibilities for a large diversity of noise experiments in the future.

A Additional Data

In this chapter of the appendix additional data which was acquired in the course of our experiments should be briefly discussed. We were investigating a highly conductive gate regime around $V_{gate} \approx 7\,\mathrm{V}$ and a regime with intermediate conductance at $V_{gate} \approx 5\,\mathrm{V}$, both featuring a higher number of electrons involved in the transport and therefore enhanced transparency. As the data is not yet fully understood and theoretical calculations are most probably much more complex than for a few-electron system, the data should only be shown for the sake of completeness. As opposed to the data presented in chapter 5 for $V_{gate} \approx 2\,\mathrm{V}$ the conductance now is higher by roughly one order of magnitude. Also the structure of the excitation spectrum is much different.

A.1 7 V Gate Range

In figure A.1 similar data as in chapter 5 but now in a gate regime around $V_{gate} \approx 7\,\mathrm{V}$ is shown. In the conductance plot in figure A.1 (b) one very pronounced excitation line is visible for positive bias, followed by a second, more faint line. In the negative bias range the lines are again more faint and at $V_{gate} \approx 7.188\,\mathrm{V}$ they bend towards the direction parallel to the gate axis. This can be an onset of a co-tunneling line, which would be reasonable as the coupling is higher that in the measurements shown in chapter 5. The Fano map exhibits overall lower values than we have seen in 5.10. As normally expected for a quantum dot [13], the Fano factor remains below $F = 1.0$ (sub Poissonian) almost everywhere in the map. At negative bias a super Poissonian (green) area with $F = 2.0$ is visible right where the excitation line is located in (b). Strong noise enhancement ($F \gtrapprox 4$) takes place along a ridge in (c) which coincides with a ridge of high differential conductance in (b). After this ridge the noise is suppressed. The suppressed region coincides with the area between the two excitation lines in (b). However coming from higher positive bias, the ridge of high noise stops exactly where in dI/dV (b) an excitation line from the left arrives. Due to the higher overall current in this gate regime also the current noise S_I is higher compared to the background noise which makes the data cleaner than in the previous measurements. Figure A.2 (a) displays a map of S_I versus the current I, similar to figure 5.12 for the 2 V gate regime. Again such a plot allows us to take cuts along the current axis which then directly represent the shot noise formula $S_I = 2e\langle I\rangle \cdot F$ where the local slope of these curves corresponds to the Fano factor. One

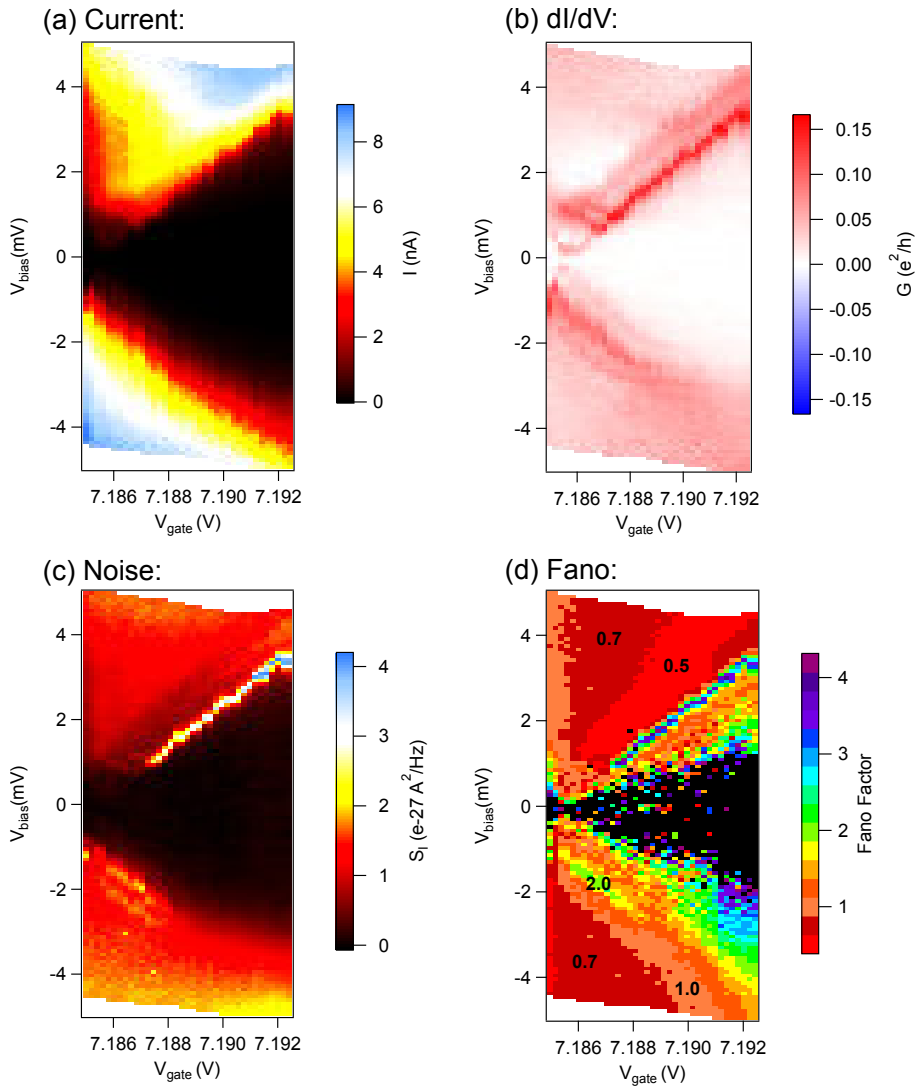

Figure A.1: Dc current (a), differential conductance (b), voltage noise (c) and the calculated Fano factor (d) for the $V_{gate} \approx 7\,\mathrm{V}$ regime featuring higher transparency. Noise is strongly enhanced along a ridge in (c) leading to Fano factors $F \approx 4$ while for the rest of the the map sub Poissonian noise ($F \lessapprox 1$) is dominant.

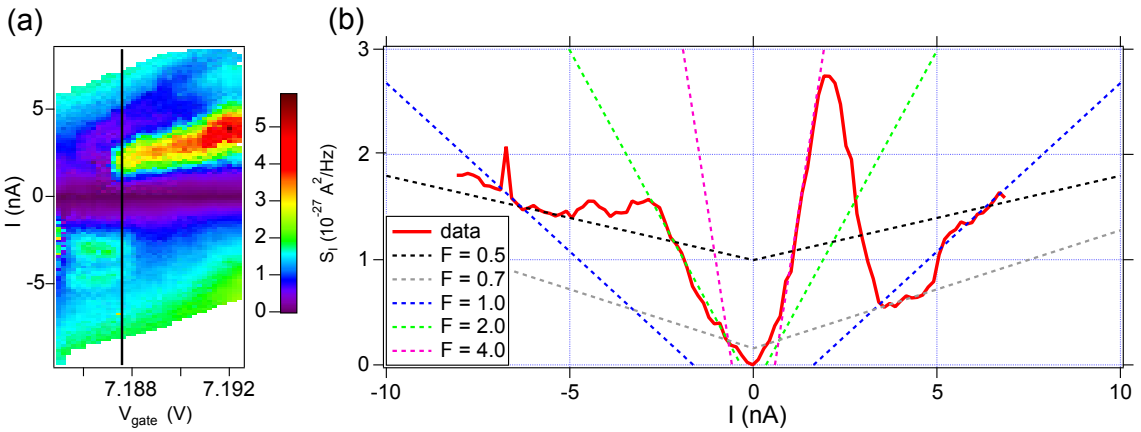

Figure A.2: (a) current noise S_I as a function of absolute current $|I|$ and gate voltage V_{gate}. (b) a line cut along the black line in (a) compared to several discrete slopes of several Fano factors shows the local change of slopes of our noise data, similar to figure 5.12.

example of such a cut along the black line in figure A.2 (a) is shown in A.2 (b). The local slopes of noise vs current arrive to discrete values such as $F \in \{0.5, 0.7, 1.0, 2.0, 4.0\}$. The dashed colored lines represent the calculated noise values for certain fixed Fano factors as indicated in the figure legend. Super Poissonian noise with F up to 4.0 is only present for lower bias voltages, at higher bias the noise approaches the Poissonian limit ($F = 1.0$) or the expected sub Poissonian value $F = 0.5$ for a quantum dot.
So far we can not state any more than that there has to be also a process of channel blocking apparent in this gate regime. Most likely similar bosonic modes play a role in the transport since it is the very same device as in section 5.3.

A.2 5 V Gate Range

The data taken around $V_{gate} \approx 5\,\mathrm{V}$ represents an intermediate coupling regime between the 2 V and the 7 V range with overall conductance values of roughly half the magnitude as in the previous section. Figure A.3 shows again an overview of all the relevant data acquired in this gate regime. The excitation spectrum in (b) is much more complex than in the low transparency data. As opposed to the $V_{gate} \approx 7\,\mathrm{V}$ range NDC is still present and clearly visible in A.3 (a) and (b). Noise enhancement in (c) coincides with the onset and the end of the NDC area. In the Fano map (d) again noise is sub Poissonian except several smaller areas at lower and one relatively large domain with super Poissonian noise. At negative bias around $3\,\mathrm{V} \leq V_{bias} \leq 4\,\mathrm{V}$ a smaller ridge featuring extraordinary large Fano factors is present. As the color scale in A.3 (d) is limited to $F \leq 3.0$ we look again at a line cut of a S_I vs $|I|$ and V_{gate} diagram in figure A.4. For high bias voltages the slope of noise versus current again approaches the Poissonian limit ($F = 1.0$) or $F = 0.5$, while at lower bias current the slope and thus the Fano factor can reach a value of $F = 8.0$ on this area

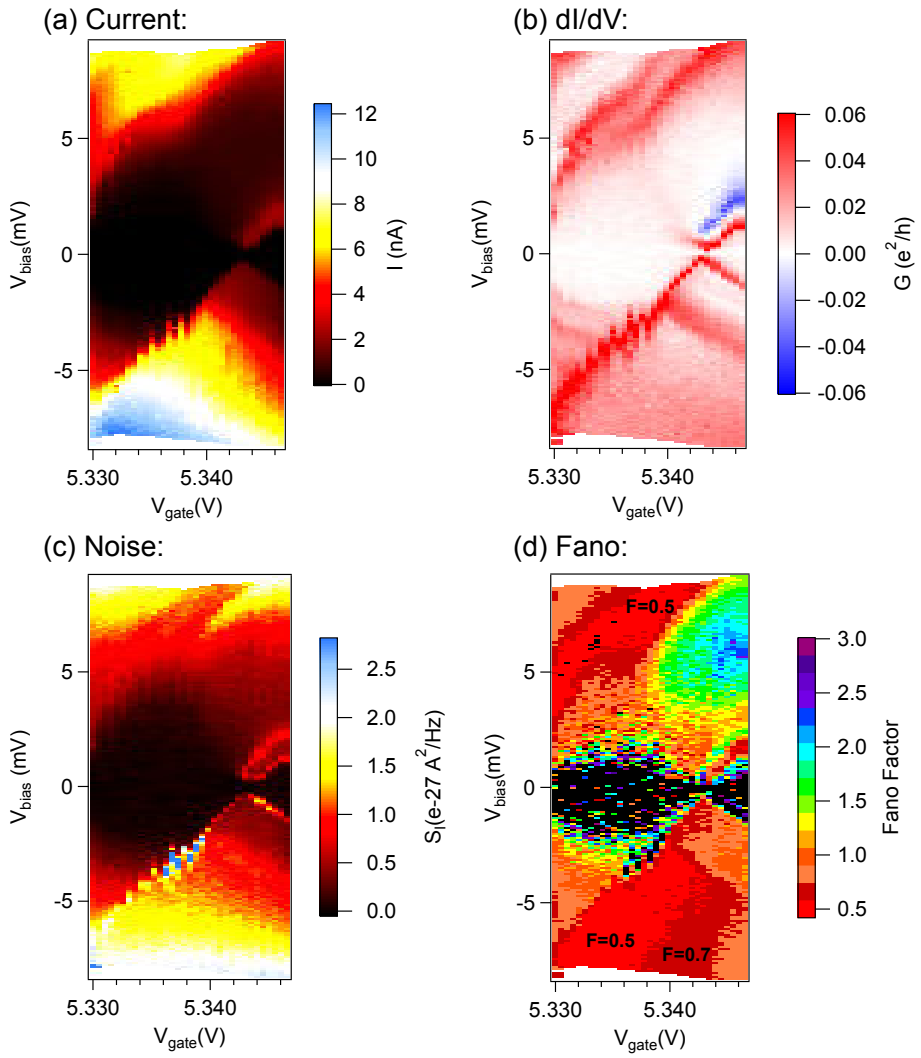

Figure A.3: Dc current (a), differential conductance (b), voltage noise (c) and the calculated Fano factor (d) for the $V_{gate} \approx 5$ V with intermediate transparency. Negative differential conductance is still present in (b) and is connected with noise enhancement in (c) and (d).

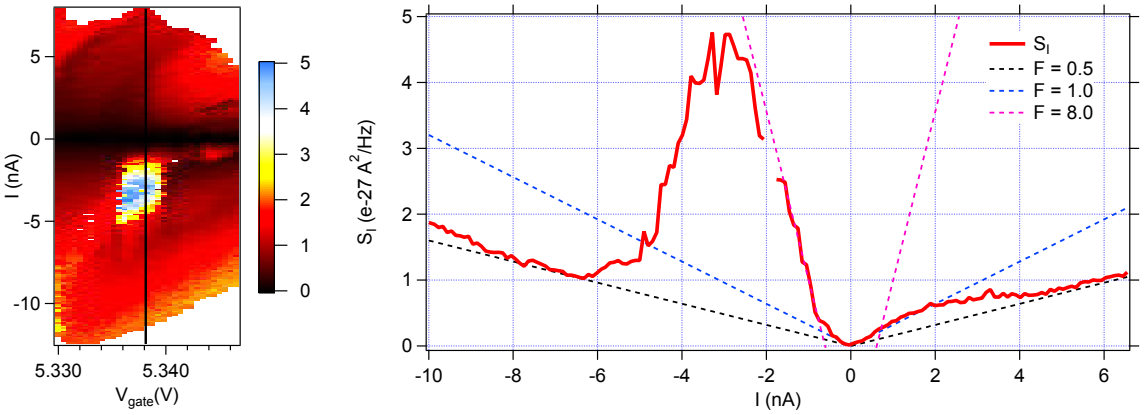

Figure A.4: (a) Current noise S_I as a function of absolute current $|I|$ and gate voltage V_{gate}. (b) a line cut along the black line in (a) compared to three different calculated Fano factors. The Fano factor can reach values up to $F = 8.0$.

at negative bias. We can at the moment not identify any features in the current witch can be linked to this high Fano values, but most probably also this large noise here is closely connected to bosonic excitations.

B Circuit Analysis

In this chapter we present a detailed analysis of our low noise amplifier circuit based on notes by Dr. Nicola Paradiso [123]. First we will give the definitions as a simplification which are helpful for the later understanding of the circuit. Later all sources of noise present in our setup, as for instance additional resistors, are considered and a theoretical expectation for the background noise is calculated. In section B.3 the quality factor of the used RLC circuit is determined and compared with the measured values. The last section deals with different calibration attempts which ultimately resulted in the QPC method scheme described in section 3.6.

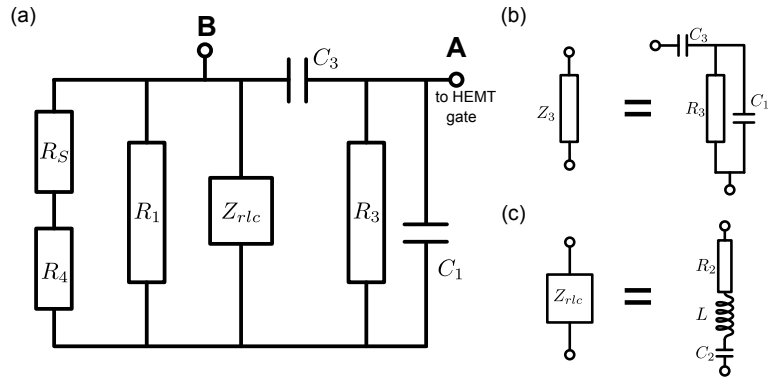

Figure B.1: (a) Sketch of the circuit we are going to study. R_s is the sample, R_1 is given by the parallel connection of two resistors with 106 kΩ, Z_{RLC} is the series of R_2, L, and C_2. R_3 and C_3 are used to properly decouple the HEMT from the sample. R_4 is a 106 kΩ resistor placed after the sample drain contact. (b) The circuit impedance Z_{RLC} consists of a series of an inductor with inductance L, its intrinsic resistance R_2, and a decoupling capacitor C_2. The C_2 capacitor is used to avoid a short to ground for low frequencies. (c) For convenience, the value of C_3 in series to the parallel of R_3 and C_1 will be called Z_3 for now. C_1 represents the coax cable capacitance. Indeed this must be treated as a distributed resistor (see figure B.5 (b)) shunted to ground via a distributed capacitor. In the mK regime, the values for the components are: $R_1 = 0.5 \cdot R_4 = 53\,\text{k}\Omega$, $L = 66\,\mu\text{H}$, and $C_2 = 2\,\text{nF}$, $R_3 = 10\,\text{M}\Omega$ and $C_3 = 1.1\,\text{nF}$.

B.1 The Circuit: Definitions

The circuit we are going to analyze is depicted in figure B.1. R_s represents the sample, R_1 the parallel of two 106 kΩ resistors placed at the PCB board[1], Z_{RLC} is the series of R_2, L and C_2,[2] R_2 corresponds to the finite resistance of the inductor L, R_3 is a resistor which keeps the dc voltage of the HEMT gate to a well defined (0 V) value[3], C_3 decouples the sample from the transistor for low frequencies. The resistor R_4 is a 106 kΩ resistor placed after the sample drain contact. The values for the components are: $R_1 = 53\,\text{k}\Omega$ (parallel of two 106 kΩ resistors), $R_4 = 106\,\text{k}\Omega$, $R_2 = 0.25\,\Omega$ ($\approx 25\,\Omega$ at room temperature), $R_3 = 10\,\text{M}\Omega$, $C_2 = 2\,\text{nF}$, $C_3 = 1.1\,\text{nF}$, $L = 2 \times 33 = 66\,\mu\text{H}$. At low temperatures the resistors show a resistance increase of $\approx 6\%$ compared to the nominal values of 100 kΩ (thus $R_4 = 106\,\text{k}\Omega$, $R_1 = 53\,\text{k}\Omega$ as stated above). The resistance of the inductors saturates at temperatures around $T = 4\,\text{K}$ to a value around $R_2 = 0.25\,\Omega$, which implies a residual resistance ratio of 100, which is typical for clean copper. The value of the cable capacitance, which provides C_1, can be determined empirically by means of the resonance frequency of the RLC circuit. This is found to be 1.80 MHz, which implies $C_1 = 142\,\text{pF}$[4]. This value was confirmed by a measurement of the cable capacitance using a LCR-meter ($C_1^{meas} \approx 140\,\text{pF}$). Another known parameter is the resonance full width at half maximum (FWHM) Δf for the voltage power spectral density measured at the gate. The measured values is $\Delta f \approx 74\,\text{kHz}$. The Q factor is then around $Q \sim 24$. This will be discussed in section B.3. In the following section the sources of noise in our circuit will be discussed in detail.

B.2 The Sources of Noise

Our goal is to compute the voltage fluctuations at the point A (see figure B.1(a)) in terms of the current fluctuations in the sample and in the other resistors. Using the superposition principle, i.e., the noise sources are considered statistically independent, we have that the mean square voltage fluctuation in A is the sum of the individual mean square voltage fluctuations induced by each source of *current* fluctuations. More precisely, the voltage power spectral density (PSD) in A is given by:

$$S_{\mathsf{A}}^V = S_s^V + S_1^V + S_2^V + S_3^V + S_4^V, \tag{B.1}$$

where S_s^V is the voltage PSD in A generated by the current fluctuations in the sample, S_1^V is the voltage PSD in A generated by the current fluctuations of the resistor R_1, S_2^V is the voltage PSD in A generated by the current fluctuations of the resistor R_2, and so on.

[1] A more detailed sketch of the circuit is provided in sections B.4 and B.A.

[2] Without C_2 the circuit is just a short to ground at low frequencies. The expression for the circuit impedance is $Z_{RLC} = R_2 + j\omega L + 1/(j\omega C2)$.

[3] The presence of the decoupling capacitor C_3 makes the resistor R_3 necessary. The gate of the transistor is otherwise floating for low frequencies.

[4] The capacitor C_2 and C_3 must be considered in series with C_1 within the resonator.

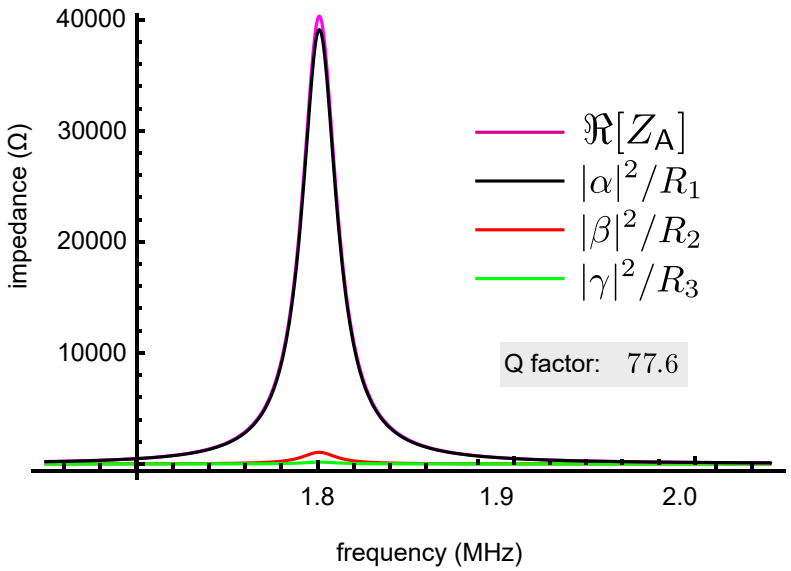

Figure B.2: Plot of $|\alpha|^2/R_1$ (black), $|\beta|^2/R_2$ (red), $|\gamma|^2/R_3$ (green) as a function of the frequency. If the sample is very resistive ($R_s \gg R_1$), then the terms $|\alpha|^2/R_s$ and $|\delta|^2/R_4$ are completely negligible in this scale. The first term $|\alpha|^2/R_1$ is the only relevant term. The function $\Re\mathfrak{e}[Z_A]$ is plotted in magenta. From the fluctuation-dissipation theorem it follows that $\Re\mathfrak{e}[Z_A]$ equals the sum of all the other terms $|\alpha|^2/R_1 + |\beta|^2/R_2 + |\gamma|^2/R_3 \ldots$.

It is possible to write the sum in equation B.1 in the following way:

$$S_A^V = |\alpha|^2 S_1^I + |\alpha|^2 S_s^I + |\beta|^2 S_2^I + |\gamma|^2 S_3^I + |\delta|^2 S_4^I, \tag{B.2}$$

where α, β, γ, δ are complex functions of ω which connect the voltage induced in A by the current fluctuation in each component, e.g., $v_{A,1} = \alpha \tilde{i}_1$, $v_{A,2} = \beta \tilde{i}_2$, $v_{A,3} = \gamma \tilde{i}_3$, $v_{A,4} = \delta \tilde{i}_4$. These functions are derived in the sub-appendix B.A. The power spectral density of the current fluctuation in the j-component is $S_j^I = 4k_B T/R_j$, with $j = 1, 2, 3, 4, s$. For the moment we assume that only equilibrium (Johnson) noise is present. **It turns out that in equation B.2 only the first term in the right hand is relevant, as shown in figure B.2.** The circuit analysis and the calculation of the α, β, etc., is shown in the appendix of this section B.A. A remarkable result of the circuit theory [60] states that a network of (linear) passive elements with complex impedance Z presents a thermal noise voltage with power spectrum $S_V = 4k_B T \Re\mathfrak{e}(Z)$. That means that fluctuations are originated only by the dissipative part of the circuit, which is represented by the real part of the impedance. Therefore this result can be regarded a particular case of the fluctuation-dissipation theorem [124]. Using the fluctuation-dissipation theorem one can write the Johnson noise generated in A by the whole passive circuit as $4k_B T$ times the real part of the impedance Z_A from A to ground. Therefore from equation B.2 we have

$$4k_B T \Re\mathfrak{e}[Z_A] = |\alpha|^2 S_1^I + |\alpha|^2 S_s^I + |\beta|^2 S_2^I + |\gamma|^2 S_3^I + |\delta|^2 S_4^I. \tag{B.3}$$

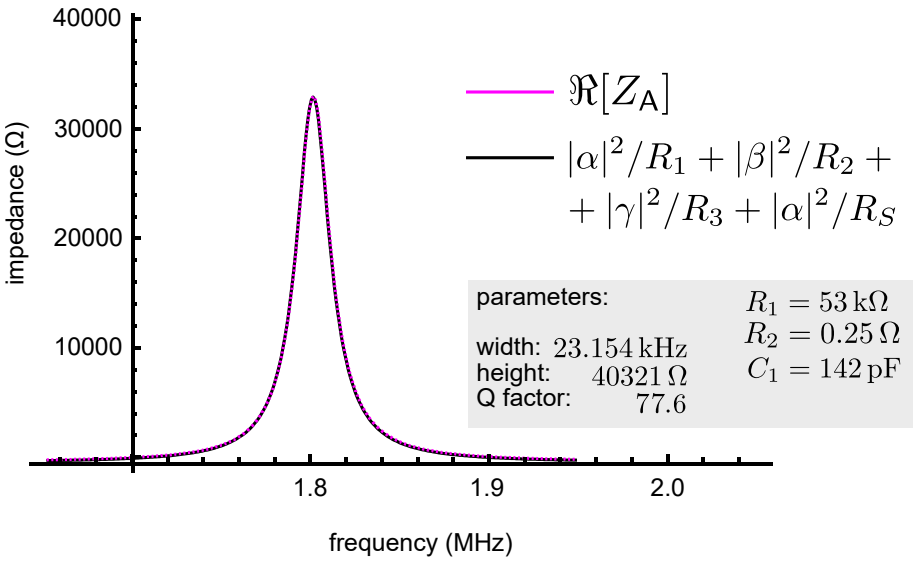

Figure B.3: Plot of $|\alpha|^2/R_1 + |\beta|^2/R_2 + |\gamma|^2/R_3 + |\delta|^2/R_4 + |\alpha|^2/R_s$ (black) and $\Re\mathfrak{e}[Z_A]$ (magenta). The two functions are identical.

Figure B.3 shows the plot of both hands of equation B.3 (divided by $4k_BT$). The two functions are identical.

B.3 The Q Factor

Using the above mentioned values for R_1, R_s, R_2, R_3, R_4, C_1, C_2, C_3 and L one obtains a theoretical Q factor of $Q_{th} = f_0/\Delta f = 1800\,\mathrm{kHz}/23.2\,\mathrm{kHz} = 77.6$. This is higher than the value we actually measure ($Q_{exp} = f_0/\Delta f = 1800\,\mathrm{kHz}/74.5\,\mathrm{kHz} = 24.2$). In figure B.4 the equivalent of figure B.2 for $Q = 24$ is shown. Notice that the ratio between $|\alpha|^2/R_1$ and $\Re\mathfrak{e}[Z_A]$ is reduced from nearly 1 (see figure B.2) to less than 1/3. This ratio will be discussed below.

A possible reason for the broadening is the fact that the coax cable from the gate to the gate of the HEMT cannot simply be approximated as a simple capacitance (C_1). Indeed, it must be treated as a distributed resistor shunted with a distributed capacitor as depicted in figure B.5 (b). Numerical circuit simulations confirm that a distributed resistance of $\approx 40\,\Omega$ is sufficient to broaden the resonance such that $Q \approx 31$. The $40\,\Omega$ resistance is a realistic estimate for the coax cable which is specified as $\rho = 50 \pm 3.0\,\Omega/\mathrm{m}$ and the cable length is in the range of 1 m. The scheme of our simulation is depicted in the panel (a) of figure B.5. In panel (b) we show the $\Re\mathfrak{e}[Z_A]$ and $|\alpha|^2/R_1$ functions. The ratio $|\alpha|^2/\Re\mathfrak{e}[Z_A]$ is 20.5 kΩ, slightly more than the value for $Q = 24$.

The simulation indicates that the coax between R_1 and ground plays no role. Since the Q factor is still higher than the observed one, probably the cable resistance is slightly higher than $40\,\Omega$. It seems therefore that we have found the reason for the broadening.

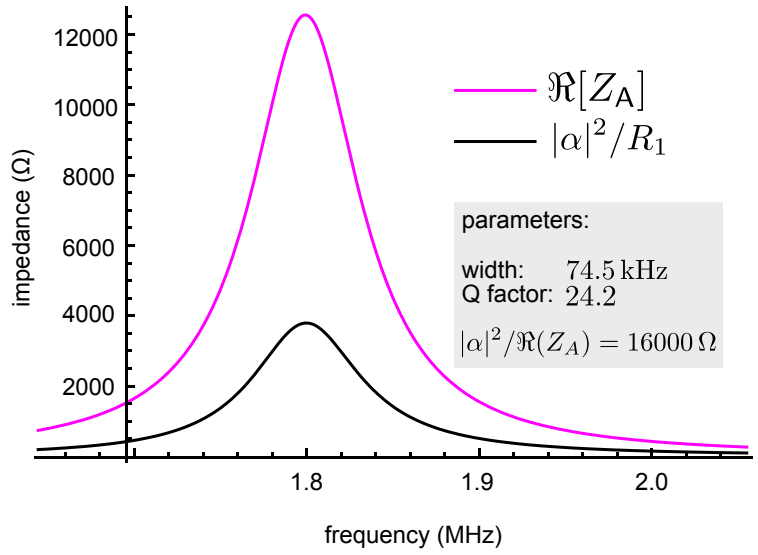

Figure B.4: Plot of $\Re\mathfrak{e}[Z_A]$ (magenta) and $|\alpha|^2/R_1$ (black) as functions of the frequency for $Q = 24$. Compare these curves with corresponding ones in figure B.2. To reduce the Q factor one can alternatively increase R_2 to 21.5 Ω (keeping $R_1 = 53\,\text{k}\Omega$) or reduce R_1 to 16.2 kΩ (keeping $R_2 = 0.25\,\Omega$): the effect is the same. The width is 74.5 kHz. The ratio $|\alpha|^2/\Re\mathfrak{e}[Z_A]$ is 16 kΩ (it was nearly 53 kΩ in figure B.2).

However, as explained in the next section, this is not sufficient to explain the results of the Johnson noise tests.

B.4 Noise Calibration

B.4.1 Shot Noise of a Quantum Point Contact

Measuring a quantum point contact (QPC) (see figure 3.10) we can find the voltage noise as a function of the current

$$S_A^V = g^2|\alpha|^2 S_s^I = 2g^2|\alpha|^2 eI, \tag{B.4}$$

where the S_s^I is the excess current noise generated by the sample and g is the total amplification factor from the HEMT gate up to the spectrum analyzer. From the slope $2eg^2|\alpha|^2$ of the linear relation we can deduce $g^2|\alpha|^2$ which is $3.6{\times}10^{15}\,\Omega^2$. This factor simply converts the value measured on the spectrum analyzer to the current fluctuation in the sample. The great advantage of this calibration is that there is no assumption about the passive circuit (that is, on α). We just require that it is linear. Note that this slope is only correct for a Fano factor $F = 1$. We did the calibration close to the pinch off point of the QPC where $t \to 0$, we can therefore assume $F = 1$. More data on noise calibration using a QPC can be found in the main text in section 3.6.

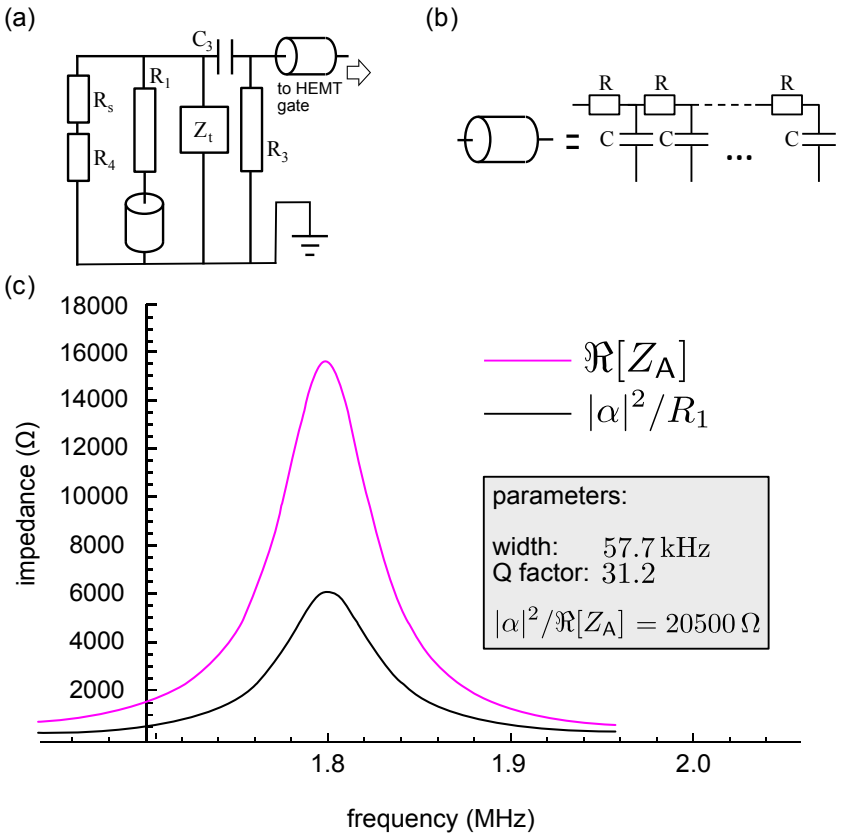

Figure B.5: (a) Scheme of the circuit simulated by *LTspice*. (b) The coax is indeed modeled as a stack of 20 resistors shunted by 20 capacitors such that the total capacitance is 142 pF and the total resistance is 40 Ω. (c) Plot of $\Re\mathfrak{e}[Z_\mathsf{A}]$ (magenta) and $|\alpha|^2/R_1$ (black) computed by the circuit simulator. It turns out that the coax connecting R_1 to ground plays no role. The Q factor is nearly 31, which implies that the coax cable resistance is probably slightly higher than the assumed 40 Ω. The ratio $|\alpha|^2/\Re\mathfrak{e}[Z_\mathsf{A}]$ here is 20.5 kΩ.

B.4.2 Johnson Noise Test

With a quantum dot sample in blockade or disconnected we can measure the temperature dependence of the thermal noise generated by the real part of the impedance from A to ground

$$S^V_{meas} = g^2 4k_B T \Re\mathfrak{e}[Z_\mathsf{A}] \equiv \kappa T, \tag{B.5}$$

where the experimental slope κ is found to be $\kappa = 4.4 \cdot 10^{-11}\,\mathrm{V^2\,Hz^{-1}\,K^{-1}}$ which implies that $g^2\Re\mathfrak{e}[Z_\mathsf{A}] = 7.97 \cdot 10^{11}\,\Omega$. From the value for $g^2\alpha^2$ obtained by the QPC calibration in the previous section we can determine the ratio $|\alpha|^2/\Re\mathfrak{e}[Z_\mathsf{A}]$

$$\frac{g^2|\alpha|^2}{g^2\Re\mathfrak{e}[Z_\mathsf{A}]} = \frac{3.6 \cdot 10^{15}}{7.97 \cdot 10^{11}} = 4517\,\Omega, \tag{B.6}$$

We notice that this ratio is much smaller than the value from the experimental Q factor scenario (16 kΩ for $Q = 24$, figure B.4). From our circuit model we find that in order to

obtain such a low value of $|\alpha|^2/\Re\mathfrak{e}[Z_\mathsf{A}]$, the Q factor must be much worse than the effective one (that is $Q \sim 10$). In other words, the Johnson noise test provided inconsistent results. We suspect that there is an additional temperature dependent source of noise which is not covered by our model and is negligible at very low temperatures. Possible candidates are the resistance of the coax cables running from the HEMT down to the sample holder or the ohmic resistance of the inductors in the RLC circuit.

B.A Calculation of $\alpha, \beta, \gamma, \delta$

This sub-appendix will demonstrate the calculation of the functions $\alpha, \beta, \gamma, \delta$ which were used in the sections before.
Let us start with R_1. Current fluctuation $\tilde{i}_1$ generated by R_1 can be modeled as injected by a current generator in parallel to R_1 (see figure B.6(a)). The voltage fluctuation in **B** is $\tilde{v}_{\mathsf{B}} = \tilde{i}_1 Z_B$. The voltage fluctuation is given by $\tilde{v}_{\mathsf{A}} = \eta \tilde{v}_{\mathsf{B}} = \eta \tilde{i}_1 Z_B$. If we take the PSD we deduce that:

$$S_1^V = |\eta Z_B|^2 S_1^I \equiv |\alpha|^2 S_1^I, \tag{B.7}$$

which defines

$$\boxed{\alpha \equiv \eta Z_B.} \tag{B.8}$$

Since R_1 is a resistor, $S_1^I = 4k_B T/R_1$.

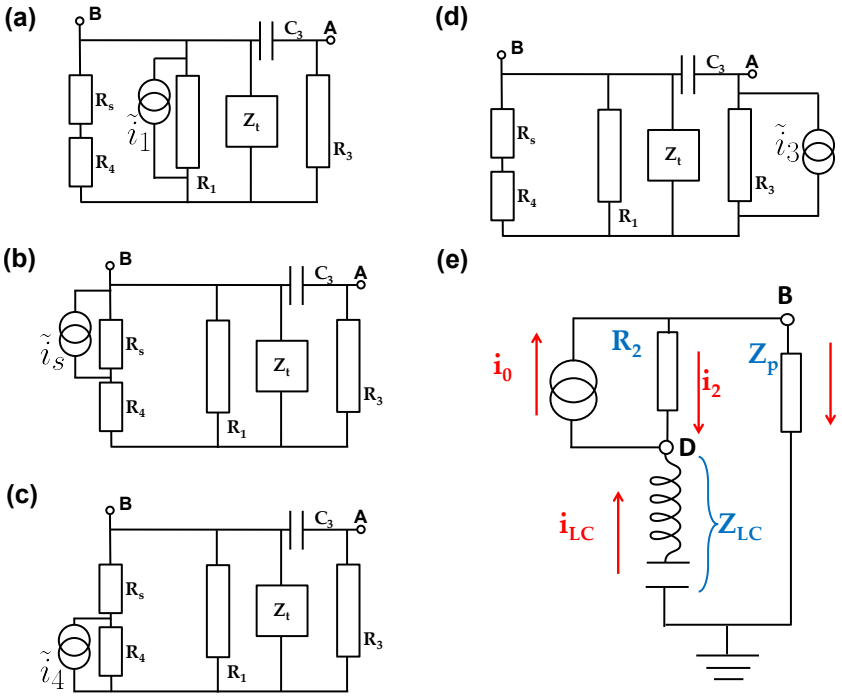

Figure B.6: To find the voltage fluctuation induced in **A** by the current fluctuation $\tilde{i}_j$ of the circuit element j one has to model $\tilde{i}_j$ as produced by an ideal current source in parallel to that circuit element. The circuit is linear, therefore $\tilde{v}_{\mathsf{A}} = \tilde{i}_j f(\omega)$, where f is a complex function. $f = \alpha$ for panel (a) and (b), $f = \delta$ in panel (c), $f = \gamma$ in panel (d), $f = \beta$ in panel (e). Once the function f is found, $S_j^V = |f|^2 S_j^I$. The total PSD is given by the sum of the individual contributions.

In a similar way (see figure B.6(b)) one finds that

$$S_s^V = |\eta Z_B|^2 S_s^I \equiv |\alpha|^2 S_s^I, \tag{B.9}$$

for the voltage fluctuations generated by the sample. If we only have thermal noise, then $S_s^I = 4k_BT/R_s$.
The resistor R_3 generates noise directly in **A** (see figure B.6(d)). $\tilde{v}_{\mathsf{A}} = \tilde{i}_3 Z_{\mathsf{A}}$.

$$S_3^V = |\gamma|^2 S_3^I, \tag{B.10}$$

where

$$\boxed{\gamma \equiv Z_{\mathsf{A}}} \tag{B.11}$$

and $S_3^I = 4k_BT/R_3$.
The same trick is used for R_4. Given a current fluctuation $\tilde{i}_4$ the voltage in **B** is (see figure B.6(c))

$$\tilde{v}_{\mathsf{B}} = \tilde{i}_4 \left(\frac{1}{\frac{1}{R_4} + \frac{1}{R_s + Z_q}} \frac{1}{R_s + Z_q} Z_q \right). \tag{B.12}$$

To obtain $\tilde{v}_{\mathsf{A}}$ we simply have to multiply by η. Thus

$$S_4^V = S_4^I |\delta|^2, \tag{B.13}$$

where

$$\boxed{\delta \equiv \left(\frac{1}{\frac{1}{R_4} + \frac{1}{R_s + Z_q}} \frac{1}{R_s + Z_q} Z_q \right) \eta.} \tag{B.14}$$

The R_2 case requires more care. For convenience we can redefine the circuit as shown in figure B.6(e). We define Z_P as:

$$Z_p \equiv (R_s + R_4) \parallel R_1 \parallel Z_3 = \frac{1}{\frac{1}{R_1} + \frac{1}{R_s + R_4} + \frac{1}{Z_3}}$$

and Z_{LC} as:

$$Z_{LC} \equiv j\omega L + \frac{1}{j\omega C_2}$$

as shown in figure B.7.
Using the Kirchhoff law for the currents in the nodes **B** and **D** (see figure B.6(e)) we have $i_0 = i_2 + i_p$ and $i_0 = i_2 + i_{LC}$ respectively, therefore $i_{LC} = i_p$. We use this in the Kirchhoff law for the voltages, thus we obtain:

$$Z_p i_p + Z_{LC} i_p - R_2 i_2 = 0,$$

$$i_p = \frac{R_2}{Z_p + Z_{LC}} i_2 = \frac{R_2}{Z_p + Z_{LC}} (i_0 - i_p),$$

$$(Z_p + Z_{LC}) i_p + R_2 i_p = R_2 i_0,$$

$Z_{LC} = j\omega L + \frac{1}{j\omega C_2}$ 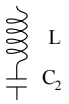	$\eta \equiv \frac{v_A}{v_B} = \frac{\left(\frac{1}{\frac{1}{R_3}+j\omega C_1}\right)}{Z_3}$
$Z_q = \frac{1}{\frac{1}{R_1}+\frac{1}{Z_{rlc}}+\frac{1}{Z_3}}$ 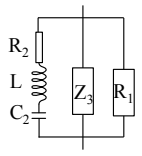	$Z_B = \frac{1}{\frac{1}{R_1}+\frac{1}{R_S+R_4}+\frac{1}{Z_3}+\frac{1}{Z_{rlc}}}$
$Z_p = \frac{1}{\frac{1}{R_1}+\frac{1}{R_S+R_4}+\frac{1}{Z_3}}$ 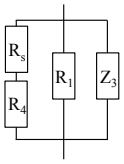	$Z_A = \frac{1}{j\omega C_1 + \frac{1}{R_3} + \frac{1}{\frac{1}{j\omega C_3}+\left(\frac{1}{\frac{1}{Z_{rlc}}+\frac{1}{R_S+R_4}+\frac{1}{R_1}}\right)}}$

Figure B.7: Some of the definitions used in these notes. In particular Z_B and Z_A is the impedance from B and from A to ground, respectively. η is the transfer function from B to A, i.e., the ratio between the voltage in A and the voltage in B. Notice that the definitions of Z_{RLC} and Z_3 have been provided in figure B.1(b,c).

$$i_p = \frac{R_2}{Z_p + Z_{LC} + R_2} i_0.$$

The voltage in B is then

$$\tilde{v}_\mathsf{B} = Z_p i_p = \frac{Z_p R_2}{Z_p + Z_{LC} + R_2} i_0.$$

From the voltage in B one obtains the voltage in A by multiplying it by η. Therefore:

$$S_2^V = |\beta|^2 S_2^I, \tag{B.15}$$

where

$$\boxed{\beta \equiv Z_p i_p = \frac{Z_p R_2}{Z_p + Z_{LC} + R_2}\eta.} \tag{B.16}$$

C Recipes

C.1 Preparation of the Substrate Chips

For all our experiments boron-doped silicon (p++) was used as a substrate material which comes as wafers (typical diameter: 4"), already covered by a layer of silicon oxide (SiO_2) of thickness 300 nm. The wafers are cleaved after diamond scraping in 16 mm x 16 mm chips to use in an upscaled process. In this way alignment markers for 16 smaller chips (4 mm x 4 mm) can be fabricated at the same time.
Next the sample is spin coated with e-beam resist, alignment markers are the defined by e-beam lithography followed by a metalization process and lift off according to the following steps:

- Cleaning the chip:
  - 2x ultrasonic bath (acetone): 1 min
  - Rinse with isopropanol (IPA).
  - Blow dry with N_2.
- Spin coating:
  - PMMA 200 k/3.5 % (solvent: chlorobenzene) standard parameters (**Stage 1:** speed: 3000 rpm, acceleration time: 0 s, duration: 5 s; **Stage 2:** speed: 8000 rpm, acceleration time: 9 s, duration: 30 s)
  - Prebake: 8 min at 150 °C
- Lithography of alignment markers:
  - Acceleration voltage: V_{acc} = 25 kV
  - Area dose: 300 µC/cm^2
  - Aperture: 60 µm (small structures), 120 µm (big structures)
  - Development: MIBK:IPA (3:1): 90 s, IPA: 30 s
- Metalization (dc sputtering):

  - Material: rhenium (Re)
  - Sputtering power: 75 W
  - Rate: ~ 1.5 Å/s
  - Thickness: 30 nm

- Lift-off:
  - Acetone bath: 60 °C, until all unwanted metal is removed
  - Rinse with isopropanol (IPA).
  - Blow dry with N_2.

Now the chip with the alignment marker is finished, we can proceed with the CNT growth process.

C.2 CNT Synthesis (CVD)

C.2.1 Catalyst Dots

- Cleaning the chip:
  - 2x ultrasonic bath (acetone): 1 min
  - Rinse with isopropanol (IPA).
  - Blow dry with N_2.
- Spin coating:
  - Layer 1: PMMA 200 k/7 % (solvent: chlorobenzene) standard parameters (**Stage 1:** speed: 3000 rpm, acceleration time: 0 s, duration: 5 s; **Stage 2:** speed: 8000 rpm, acceleration time: 9 s, duration: 30 s)
  - Prebake: 8 min at 150 °C
  - Layer 2: PMMA 950 k/2 % (solvent: chlorobenzene) standard parameters (**Stage 1:** speed: 3000 rpm, acceleration time: 0 s, duration: 5 s; **Stage 2:** speed: 8000 rpm, acceleration time: 9 s, duration: 30 s)
  - Prebake: 8 min at 150 °C
- Lithography of the catalyst dots:
  - Acceleration voltage: $V_{acc} = 25$ kV
  - Area dose: 300 µC/cm^2
  - Aperture: 60 µm
  - Development: MIBK:IPA (3:1): 90 s, IPA: 30 s

  - Blow dry with N_2.

- Catalyst deposition:
  - Catalyst suspension:
    * $(Fe(NO_3)_3 \cdot 9H_2O$ (Sigma-Aldrich GmbH): 40 mg
    * Al_2O_3 (fine powder, particle size ~14 mm, Degussa GmbH): 30 mg
    * $[CH_3COCH = C(O-)CH_3]_2 MoO_2$ (Sigma-Aldrich GmbH): 4–15 mg

    The amount of the latter compound determines the density of CNTs growing on the chips later. All three components are mixed inside a glass flask which is then filled up with 30 ml of methanol (CH_3OH) and sonicated for at least one hour.
  - Deposition:
    * With a clean Pasteur pipette put some drops of the catalyst suspension on the chip, until it is fully covered (2–3 drops).
    * Blow dry with N_2.
    * Bake out the chip on a hot plate at 150 °C for 5 min.
  - Catalyst lift-off:
    * Heat a beaker with acetone to 60 °C, put a magnet stirrer inside.
    * Hold the chip upside-down in the the warm acetone while stirring slowly for 2 min.
    * Rinse with isopropanol (IPA).
    * Blow dry with N_2.
  - Cutting into smaller chips:
    * Spin-coat the chip again with a thick layer of PMMA (e.g. 200 k/7 %).
    * Bake for 8 min at 150 °C.
    * Diamond-scrape the chip into pieces of 4 mm x 4 mm and cleave it.

The single chips are now ready for the actual CVD growth process.

C.2.2 CVD Growth

The samples which are still covered by a protective layer of PMMA have to be cleaned again before putting it into the CVD furnace:

- 2x acetone bath: 1 min **(no ultrasonic bath!)**
- Rinse with isopropanol (IPA).

- Blow dry with N_2.

Now the CVD process can start:

- Put the sample inside the quartz glass tube, on a quartz glass crucible. The position of the sample should be in the center of the tube, right where the temperature sensor of the furnace sits.
- Close the flanges on either end of the tube.
- Open all three gas lines (Ar, CH_4,H_2) to the maximum scale on the manual controllers on the wall, bypass the computer controlled MFCs for CH_4 and H_2 for now. Flush all lines for ~ 2 min.
- Reduce the flow of Argon to 14 ($\triangleq 1.5$ l/min) on the manual scale.
- Turn the valves of CH_4 and H_2 back to the computer controlled MFCs and set the desired flow rates for these two gases in the software. Parameters used in our process:
  - Ar: 14 (manual scale)
  - CH_4: 20 sccm
  - H_2: 10 sccm
- As soon as the MFC shows the desired set values, the valves for CH_4 and H_2 can be closed completely at the fume hood.
- Turn on the furnace and set the temperature to 850 °C maintaining the Argon flow set before.
- When the desired temperature is reached, prepare a countdown timer set to the desired growth time of 20 min and close the valve for Argon at the fume hood while at the same time opening the valves for CH_4 and H_2. Start the timer.
- After the growth time (20 min) close again the valves for CH_4 and open the one for Argon. All methane is flushed out of the tube, the growth stops. The remaining flow of H_2 is used as a protection to prevent remaining oxygen in the quartz tube from reacting with the new grown CNTs.
- Open the hood of the furnace (**Attention! Hot!**), the heating will turn off but you still can watch the temperature going down. Let the furnace cool down while keeping the Argon and the H_2 flow.
- Once the temperature reaches 100 °C close the valves for argon and H_2, open the flange and remove the sample.
- Turn off the furnace, set all MFCs to zero and close all valves.

C.3 Lithography of the Contacts

SEM imaging after the growth:

- Aperture: 10 µm
- Acceleration voltage: 0.5–1 kV (start with higher values e.g. 5 kV and reduce voltage step by step with re adjusting stigmation etc in between)

Electron beam lithography was performed according to the following parameters:

- Cleaning the chip:
  - 2x acetone bath: 1 min **(no ultrasonic bath!)**
  - Rinse with isopropanol (IPA).
  - Blow dry with N_2 (carefully!).
- Spin coating for **sputtered** contacts:
  - PMMA 200 k/3.5 % (solvent: chlorobenzene) standard parameters (**Stage 1:** speed: 3000 rpm, acceleration time: 0 s, duration: 5 s; **Stage 2:** speed: 8000 rpm, acceleration time: 9 s, duration: 30 s)
  - Prebake: 8 min at 150 °C
- Lithography for **sputtered** contacts:
  - Acceleration voltage: V_{acc} = 25 kV
  - Area dose: 300 µC/cm^2
  - Aperture: 20 µm
  - Development: MIBK:IPA (3:1): 90 s, IPA: 30 s
  - Blow dry with N_2.
- Spin coating for **thermally evaporated** contacts:
  - PMMA 200 k/7 % (solvent: chlorobenzene) standard parameters (**Stage 1:** speed: 3000 rpm, acceleration time: 0 s, duration: 5 s; **Stage 2:** speed: 8000 rpm, acceleration time: 9 s, duration: 30 s)
  - Prebake: 8 min at 150 °C
- Lithography for **thermally evaporated** contacts:
  - Acceleration voltage: V_{acc} = 25 kV
  - Area dose: 300 µC/cm^2
  - Aperture: 20 µm
  - Development: IPA:H_2O (7:3): 90 s
  - Blow dry with N_2.

C.4 Metal Deposition

C.4.1 Dc Sputtering

- Material: rhenium (Re)
- Sputtering Power: 75 W
- Rate: ~ 1.5 Å/s
- Thickness: 30 nm

C.4.2 Electron Beam Evaporation (e-gun)

- Material: palladium (Pd)
  - Current: ~ 400 mA
  - Rate: ~ 1.5 Å/s
  - Thickness: 60 nm
- Material: aluminum (Al)
  - Current: ~ 150 mA
  - Rate: ~ 7–10 Å/s
  - Thickness: 30 nm

C.4.3 Effusion Cell Evaporation

- Material: palladium (Pd)
  - Voltage: ~ 40 V
  - Current: ~ 8 A
  - Rate: ~ 0.5 Å/s
  - Thickness: 60 nm

C.5 Bonding

Parameters used for bonding the chip to printed circuit board via Aluminum wires:

- First bond (on PCB):
  - Power: 200
  - Ultrasonic time: 100

- Second bond (on sample):
  - Power: 100
  - Ultrasonic time: 90

D Measurement Scripts

This chapter of the appendix gives a short example of a measurement script as it was used for a simultaneous current, differential conductance, and noise measurement. It is based on *Lab::Measurement*[1], a Perl package for measurement control.
The following example performs a 2D measurement where gate voltage and bias voltage are changed in two nested loops, the master loop (gate voltage) and the slave loop (bias voltage). The procedure follows the outline described in section 4.2.3.
Here the gate voltage is swept from 0 V to 1 V in steps of 5 mV, while the bias voltage runs from -5 mV to +5 mV in steps of 100 µV. The dc current, differential conductance, and a full noise spectrum are acquired from various measurement devices and saved into a file:

```
use Lab::Measurement;
use PDL;
use PDL::NiceSlice;
use PDL::IO::Misc;
```

In the header of the script all packages which are necessary are loaded by the command **use**. Apart from the aforementioned package *Lab::Measurement* also *PDL*, the Perl Data Language[2] is loaded which is used for simple in-script data manipulations (see later).
The next block initializes all the external devices used in the measurement, it includes the name of the driver which has to be loaded for the specific device (e.g. `Instrument('Yokogawa7651'...` for a voltage source type Yokogawa 7651) and its GPIB address (e.g. `gpib_address => 6`):

```
our $BACKGATE = Instrument('Yokogawa7651', {
connection_type => 'VISA_GPIB',
gpib_address => 6,
gate_protect => 0,
});

our $SOURCE = Instrument('Yokogawa7651', {
connection_type => 'VISA_GPIB',
gpib_address => 5,
gate_protect => 0,
});
```

[1] http://www.labmeasurement.de
[2] http://pdl.perl.org

```
my $srs1 = Instrument('SR830',{
connection_type=>'VISA_GPIB',
'gpib_address'  => 16
});

my $srs2 = Instrument('SR830',{
connection_type=>'VISA_GPIB',
'gpib_address'  => 12
});

my $DMM_Voltage = Instrument('HP34401A',
{
connection_type => 'VISA_GPIB',
gpib_address  => 22
});

my $VSA = Instrument('SpectrumSCPI',
{
connection_type => 'VISA_GPIB',
gpib_address  => 28
});
```

When all drivers are loaded the two sweeps are defined. First the outer loop or *master* for the backgate voltage $sweep_BG, subsequently the inner loop or *slave* defining the sweep of the bias voltage $sweep_bias. Here the start and end point of the sweeps as well as the sweep rates are set.

```
my $sweep_BG = Sweep('Voltage', {
instrument => $BACKGATE,
mode => 'step',
points => [0,1],
stepwidth => [0.005],
rate => [0.01,0.0001],
delay_before_loop => 1,
jump => 0,
});


my $sweep_bias = Sweep('Voltage', {
instrument => $SOURCE,
mode => 'step',
#interval => 1,
points => [-.5,.5],
stepwidth => [.01],
rate => [.05,.01],
delay_before_loop => 1,
jump => 0,
});
```

The next section takes care of the file which the acquired data is written into. In this example the file is called *data.dat*. Also the header and the columns for the different data are defined. In this case the header contains information about the scaling of the noise spectrum which is directly read from the spectrum analyzer as an array @range with **my** @range = $VSA->get_xrange(). Each column for data is then created using the add_column command.

```
my $file = DataFile("data.dat");

my @range =$VSA->get_xrange();
my $header = "VSA frequency range: f_start = @range[0], f_stop = @range[1]";

$file->add_header($header);
$file->add_column('Backgate');
$file->add_column('BiasRAW');
$file->add_column('DCCurrent');
$file->add_column('dI');
$file->add_column('dV');
$file->add_column('dIdV');
$file->add_column('PSDraw');
$file->add_column('PSD');
$file->add_column('fullPSD');
```

The following block determines the live plots which show up during the measurement to give a first overview of the results. Here two plots are created, $plot_G showing a conductance map and $plot_PSD for a noise map. Commands like e.g. 'x-axis' => 'Backgate' assign one column of data from the previous block to an axis in the live plot.

```
my $plot_G = {
'title' => 'ChD Dot1',
'type' => 'pm3d', #'lines', #'linetrace', #point
'autosave' =>  'last',
'x-axis' => 'Backgate',
'x-label' => 'Backgate Voltage (V)',
'y-axis' => 'BiasRAW',
'y-label' => 'Bias RAW',
'refresh' => 'block',
'cb-axis' => 'dIdV',
'cb-label' => 'dI/dV (e^2/h)'
};

my $plot_PSD = {
'title' => 'PSD Dot1',
'type' => 'pm3d', #'lines', #'linetrace', #point
'autosave' =>  'last',
'x-axis' => 'Backgate',
'x-label' => 'Backgate Voltage (V)',
'y-axis' => 'BiasRAW',
'y-label' => 'Bias RAW',
'refresh' => 'block',
```

```
'cb-axis' => 'PSD',
'cb-label' => 'PSD A^2/Hz'
};

$file->add_plot($plot_G);
$file->add_plot($plot_PSD);
```

After all the drivers, the sweeps and the live plots (optional) are set, the actual measurement $my_measurement can start. Before that the spectrum analyzer has to perform an *autozero* operation to minimize spurious offsets on the signal before the measurement, this is done by sending the corresponding command to the analyzer using $VSA->autozero();. After that the readout of all devices happens e.g. **my** ($acx2,$acy2)=$srs2->get_xy(); acquires the X and Y signal from the second lock-in amplifier $srs2 and assigns the two values to two variables $acx2 and $acy2. Similar operations are performed also for multimeters, voltage sources etc.

```
$VSA->autozero();
sleep (30);

my $my_measurement = sub {

        my $sweep = shift;

        my ($acx2,$acy2)=$srs2->get_xy();
        my $DC_Voltage_RAW = $DMM_Voltage->get_value();
        my $BG_Voltage = $BACKGATE->get_value({read_mode => 'cache'});
        my $VacRaw=$srs1->get_amplitude();
        my $biasRAW = @{$sweep->{config}->{points}}[$sweep->{iterator}];


        my $dV=$acx2/(-7.3)/100;
        my $dI=(($VacRaw/10000)-$dV)/100e3;

        my $realDCcurrent=$DC_Voltage_RAW*1e-7;
```

When all scalar values for the transport data is acquired, the actual noise measurement takes place. The command $VSA->abort(); restarts the averaging process inside the spectrum analyzer followed by a break of 12 s where the measurement loop is waiting for the averaging to finish.
To get a rough estimate of the noise amplitude during the running measurement the marker on the spectrum analyzer's screen is set manually to the tip of the resonance curve before the measurement. Now we are able to read out the y-position of the marker using **my** $PSD_raw = $VSA->get_marker_level(1); as well as the full spectrum (**my** $yPSD = $VSA->get_data_y(1);).
Now with the help of the aforementioned Perl Data Language (PDL) the right end of the spectrum outside the resonance bell is undergoing an averaging operation which gives us the background noise level which is then subtracted from the marker's y-position. The

resulting value $real_PSD can be used for the noise map in the live plot. For the actual data analysis however the full spectrum $yPSD is needed.

```
        $VSA->abort();

        sleep(12);

        my $PSD_raw = $VSA->get_marker_level(1);

        my $yPSD = $VSA->get_data_y(1);

        my @y_data = split(',', $yPSD);
        my $pdl_y = pdl(@y_data);

        my $pdl_x = zeroes($pdl_y->getdim(0))->xlinvals(@range[0], @range[1]);

        my $cut_x = $pdl_x->index(which($pdl_x > 1.72e6));
        my $cut_y = $pdl_y->index(which($pdl_x > 1.72e6));

        $aver = ( conv1d($cut_y, ones(25), {Boundary => 'reflect'}) / 25 );
        my $background = stats($aver->index(which($cut_x > ($range[1] - $range
            [1]*0.02))));

        my $real_PSD = ($PSD_raw-$background)*($PSD_raw-$background);

        my $dIdV = ($dI/$dV)/(7.7480917346e-5/2);
```

The following block assigns each column in the data file a variable from the acquired data above. The last column fullPSD contains an entire spectrum consisting of 1600 y-values in comma-separated form.

```
        $sweep->LOG({
        Backgate        => $BG_Voltage,
        BiasRAW         => $biasRAW/100,
        DCCurrent       => $realDCcurrent,
        dI              => $dI,
        dV              => $dV,
        dIdV            => $dIdV,
        PSDraw          => $PSD_raw,
        PSD             => $real_PSD,
        fullPSD         => $yPSD
        });
};
```

When everything is set the measurement is started by defining a so called Frame() structure in which the master and the slave sweeps are defined with $frame->add_master(...); and $frame->add_slave(...);.
The command $frame->start(); eventually launches the measurement.

```
$file->add_measurement($my_measurement);
```

```
$sweep_bias->add_DataFile($file);

my $frame = Frame();

$frame->add_master($sweep_BG);
$frame->add_slave($sweep_bias);

$frame->start();
```

After both nested loops come to an end the measurement is finished and the script stops.

Bibliography

[1] W. Schottky, "Über spontane Stromschwankungen in verschiedenen Elektrizitätsleitern," *Annalen der Physik*, vol. 362, no. 23, pp. 541–567, 1918.

[2] M. Büttiker, "Scattering theory of thermal and excess noise in open conductors," *Physical Review Letters*, vol. 65, pp. 2901–2904, dec 1990.

[3] C. D. Glattli, "Quantum shot noise of conductors and general noise measurement methods," *European Physical Journal: Special Topics*, vol. 172, no. 1, pp. 163–179, 2009.

[4] Y. Blanter and M. Büttiker, "Shot noise in mesoscopic conductors," *Physics Reports*, vol. 336, no. 1–2, pp. 1 – 166, 2000.

[5] Y. M. Blanter, "Recent Advances in Studies of Current Noise," in *CFN Lectures on Functional Nanostructures - Volume 2* (M. Vojta, C. Röthig, and G. Schön, eds.), vol. 820 of *Lecture Notes in Physics*, pp. 55–74, Springer Berlin Heidelberg, 2011.

[6] S. Oberholzer, M. Henny, C. Strunk, C. Schönenberger, T. Heinzel, K. Ensslin, and M. Holland, "The Hanbury Brown and Twiss experiment with fermions," *Physica E: Low-dimensional Systems and Nanostructures*, vol. 6, pp. 314–317, feb 2000.

[7] R. Landauer, "Condensed-matter physics: The noise is the signal," *Nature*, vol. 392, no. 6677, pp. 658–659, 1998.

[8] R. De-Picciotto, M. Reznikov, M. Heiblum, V. Umansky, G. Bunin, and D. Mahalu, "Direct observation of a fractional charge," *Nature*, vol. 389, pp. 162–164, sep 1997.

[9] R. De-Picciotto, M. Reznikov, M. Heiblum, V. Umansky, G. Bunin, and D. Mahalu, "Direct Observation of a Fractional Charge," *Physica B*, vol. 249-251, pp. 395–400, 1998.

[10] Y. Ronen, Y. Cohen, J.-H. Kang, A. Haim, M.-T. Rieder, M. Heiblum, D. Mahalu, and H. Shtrikman, "Charge of a quasiparticle in a superconductor," *Proceedings of the National Academy of Sciences*, vol. 113, pp. 1743–1748, feb 2016.

[11] M. Reznikov, M. Heiblum, H. Shtrikman, and D. Mahalu, "Temporal Correlation of Electrons: Suppression of Shot Noise in a Ballistic Quantum Point Contact," *Physical Review Letters*, vol. 75, no. 18, pp. 3340–3343, 1995.

[12] A. Kumar, L. Saminadayar, D. C. Glattli, Y. Jin, and B. Etienne, "Experimental Test of the Quantum Shot Noise Reduction Theory," *Physical Review Letters*, vol. 76, pp. 2778–2781, apr 1996.

[13] J. H. Davies, P. Hyldgaard, S. Hershfield, and J. W. Wilkins, "Classical theory for shot noise in resonant tunneling," *Physical Review B*, vol. 46, no. 15, pp. 9620–9633, 1992.

[14] C. W. J. Beenakker and M. Büttiker, "Suppression of shot noise in metallic diffusive conductors," *Physical Review B*, vol. 46, pp. 1889–1892, jul 1992.

[15] R. Schoelkopf, P. Burke, A. Kozhevnikov, D. Prober, and M. Rooks, "Frequency Dependence of Shot Noise in a Diffusive Mesoscopic Conductor," *Physical Review Letters*, vol. 78, no. 17, pp. 3370–3373, 1997.

[16] S. Oberholzer, E. V. Sukhorukov, and C. Schönenberger, "Crossover between classical and quantum shot noise in chaotic cavities," *Nature*, vol. 415, pp. 765–767, feb 2002.

[17] M. Henny, "The Fermionic Hanbury Brown and Twiss Experiment," *Science*, vol. 284, no. 5412, pp. 296–298, 1999.

[18] Y. Zhang, L. DiCarlo, D. T. McClure, M. Yamamoto, S. Tarucha, C. M. Marcus, M. P. Hanson, and a. C. Gossard, "Noise Correlations in a Coulomb-Blockaded Quantum Dot," *Physical Review Letters*, vol. 99, p. 036603, jul 2007.

[19] L. G. Herrmann, F. Portier, P. Roche, a. L. Yeyati, T. Kontos, and C. Strunk, "Carbon Nanotubes as Cooper-Pair Beam Splitters," *Physical Review Letters*, vol. 104, p. 026801, jan 2010.

[20] J. Schindele, A. Baumgartner, and C. Schönenberger, "Near-Unity Cooper Pair Splitting Efficiency," *Physical Review Letters*, vol. 109, p. 157002, oct 2012.

[21] A. Das, Y. Ronen, M. Heiblum, D. Mahalu, A. V. Kretinin, and H. Shtrikman, "High-efficiency Cooper pair splitting demonstrated by two-particle conductance resonance and positive noise cross-correlation," *Nature Communications*, vol. 3, p. 1165, nov 2012.

[22] R. Saito, G. Dresselhaus, and M. S. Dresselhaus, *Physical Properties of Carbon Nanotubes*. London: Imperial College Press, 1998.

[23] E. Thune and C. Strunk., "Quantum Transport in Carbon Nanotubes," in *Introducing Molecular Electronics* (G. Cuniberti, K. Richter, and G. Fagas, eds.), vol. 680 of *Lecture Notes in Physics*, pp. 153–153, Springer Berlin Heidelberg, 2006.

[24] S. Ilani and P. L. McEuen, "Electron Transport in Carbon Nanotubes," *Annual Review of Condensed Matter Physics, Vol 1*, vol. 1, pp. 1–25, 2010.

[25] C. W. J. Beenakker, "Theory of Coulomb-blockade oscillations in the conductance of a quantum dot," *Physical Review B*, vol. 44, no. 4, pp. 1646–1656, 1991.

[26] H. Van Houten, C. Beenakker, and A. Staring, "Coulomb-Blockade Oscillations in Semiconductor Nanostructures," in *Single Charge Tunneling* (H. Grabert and M. Devoret, eds.), vol. 294 of *NATO ASI Series*, pp. 167–216, Springer US, 1992.

[27] H. Grabert, "Single charge tunneling: A brief introduction," *Zeitschrift für Physik B - Condensed Matter*, vol. 85, pp. 319–325, oct 1991.

[28] S. Datta, *Electronic Transport in Mesoscopic Systems*. Cambridge University Press, 1995.

[29] J. Mintmire and C. White, "Universal Density of States for Carbon Nanotubes," *Physical Review Letters*, vol. 81, no. 12, pp. 2506–2509, 1998.

[30] W. Liang, M. Bockrath, D. Bozovic, J. H. Hafner, M. Tinkham, and H. Park, "Fabry - Perot interference in a nanotube electron waveguide," *Nature*, vol. 411, no. 6838, pp. 665–669, 2001.

[31] P. Jarillo-Herrero, S. Sapmaz, C. Dekker, L. P. Kouwenhoven, and H. S. J. Van der Zant, "Electron-hole symmetry in a semiconducting carbon nanotube quantum dot.," *Nature*, vol. 429, no. 6990, pp. 389–392, 2004.

[32] L. I. Glazman and R. I. Shekhter, "Coulomb oscillations of the conductance in a laterally confined heterostructure," *Journal of Physics: Condensed Matter*, vol. 1, no. 33, pp. 5811–5815, 1999.

[33] J.-C. Charlier and S. Roche, "Electronic and transport properties of nanotubes," *Reviews of Modern Physics*, vol. 79, pp. 677–732, may 2007.

[34] A. Loiseau, P. Launois, P. Petit, S. Roche, and J.-P. Salvetat, eds., *Understanding Carbon Nanotubes*, vol. 677 of *Lecture Notes in Physics*. Berlin, Heidelberg: Springer, dec 2006.

[35] A. Jorio, G. Dresselhaus, and M. S. Dresselhaus, eds., *Carbon Nanotubes*, vol. 111 of *Topics in Applied Physics*. Berlin, Heidelberg: Springer Berlin Heidelberg, mar 2008.

[36] S. J. Tans, M. H. Devoret, H. Dai, A. Thess, R. E. Smalley, L. J. Geerligs, and C. Dekker, "Individual single-wall carbon nanotubes as quantum wires," *Nature*, vol. 386, pp. 474–477, apr 1997.

[37] P. R. Wallace, "The band theory of graphite," *Physical Review*, vol. 71, no. 9, pp. 622–634, 1947.

[38] K. S. Novoselov, A. K. Geim, S. V. Morozov, D. Jiang, Y. Zhang, S. V. Dubonos, I. V. Grigorieva, and A. A. Firsov, "Electric field effect in atomically thin carbon films.," *Science*, vol. 306, no. 5696, pp. 666–669, 2004.

[39] L. V. Radushkevich and V. M. Lukyanovich, "The structure of carbon formed by thermal decomposition of carbon monoxide on iron contacts," *Russian Journal of Physical Chemistry*, vol. 26, p. 88, 1952.

[40] N. F. Kolesnik, "Gas-phase growth of carbon microfibers on metals of the iron group," *Soviet Powder Metallurgy and Metal Ceramics*, vol. 25, pp. 750–751, sep 1986.

[41] S. Iijima, "Helical microtubules of graphitic carbon," *Nature*, vol. 354, no. 6348, pp. 56–58, 1991.

[42] D. S. Bethune, C. H. Klang, M. S. de Vries, G. Gorman, R. Savoy, J. Vazquez, and R. Beyers, "Cobalt-catalysed growth of carbon nanotubes with single-atomic-layer walls," *Nature*, vol. 363, no. 6430, pp. 605–607, 1993.

[43] S. Iijima and T. Ichihashi, "Single-shell carbon nanotubes of 1-nm diameter," *Nature*, vol. 363, no. 6430, pp. 603–605, 1993.

[44] J.-P. Salvetat, G. Briggs, J.-M. Bonard, R. Bacsa, A. Kulik, T. Stöckli, N. Burnham, and L. Forró, "Elastic and Shear Moduli of Single-Walled Carbon Nanotube Ropes," *Physical Review Letters*, vol. 82, pp. 944–947, feb 1999.

[45] M. M. J. Treacy, T. W. Ebbesen, and J. M. Gibson, "Exceptionally high Young's modulus observed for individual carbon nanotubes," *Nature*, vol. 381, pp. 678–680, jun 1996.

[46] Z. Yao, C. L. Kane, and C. Dekker, "High-Field Electrical Transport in Single-Wall Carbon Nanotubes," *Physical Review Letters*, vol. 84, pp. 2941–2944, mar 2000.

[47] M. Büttiker, "Absence of backscattering in the quantum Hall effect in multiprobe conductors," *Physical Review B*, vol. 38, no. 14, pp. 9375–9389, 1988.

[48] A. Dirnaichner, M. del Valle, K. J. G. Götz, F. J. Schupp, N. Paradiso, M. Grifoni, C. Strunk, and A. K. Hüttel, "Secondary Electron Interference from Trigonal Warping in Clean Carbon Nanotubes," *Physical Review Letters*, vol. 117, p. 166804, oct 2016.

[49] L. P. Kouwenhoven, C. M. Marcus, P. L. McEuen, S. Tarucha, R. M. Westervelt, and N. S. Wingreen, "Electron Transport in Quantum Dots," in *Mesoscopic Electron Transport* (L. L. Sohn, L. P. Kouwenhoven, and G. Schön, eds.), pp. 105–214, Dordrecht: Springer Netherlands, dec 1997.

[50] K. Grove-Rasmussen, H. Jørgensen, and P. Lindelof, "Fabry–Perot interference, Kondo effect and Coulomb blockade in carbon nanotubes," *Physica E: Low-dimensional Systems and Nanostructures*, vol. 40, pp. 92–98, oct 2007.

[51] D. R. Schmid, S. Smirnov, M. Margańska, A. Dirnaichner, P. L. Stiller, M. Grifoni, A. K. Hüttel, and C. Strunk, "Broken SU(4) symmetry in a Kondo-correlated carbon nanotube," *Physical Review B*, vol. 91, p. 155435, apr 2015.

[52] D. R. Schmid, P. L. Stiller, C. Strunk, and A. K. Hüttel, "Liquid-induced damping of mechanical feedback effects in single electron tunneling through a suspended carbon nanotube," *Applied Physics Letters*, vol. 107, p. 123110, sep 2015.

[53] P. E. Lindelof, J. Borggreen, A. Jensen, J. Nygård, and P. R. Poulsen, "Electron Spin in Single Wall Carbon Nanotubes," *Physica Scripta*, vol. T102, no. 1, p. 22, 2002.

[54] M. Gaass, A. K. Hüttel, K. Kang, I. Weymann, J. von Delft, and C. Strunk, "Universality of the Kondo Effect in Quantum Dots with Ferromagnetic Leads," *Physical Review Letters*, vol. 107, p. 176808, oct 2011.

[55] T. S. Jespersen, K. Grove-Rasmussen, J. Paaske, K. Muraki, T. Fujisawa, J. Nygård, and K. Flensberg, "Gate-dependent spin–orbit coupling in multielectron carbon nanotubes," *Nature Physics*, vol. 7, 2011.

[56] Y. Oreg, K. Byczuk, and B. I. Halperin, "Spin Configurations of a Carbon Nanotube in a Nonuniform External Potential," *Physical Review Letters*, vol. 85, pp. 365–368, jul 2000.

[57] S. Sapmaz, P. Jarillo-Herrero, J. Kong, C. Dekker, L. P. Kouwenhoven, and H. S. J. van der Zant, "Electronic excitation spectrum of metallic carbon nanotubes," *Physical Review B*, vol. 71, p. 153402, apr 2005.

[58] D. H. Cobden and J. Nygård, "Shell Filling in Closed Single-Wall Carbon Nanotube Quantum Dots," *Physical Review Letters*, vol. 89, p. 046803, jul 2002.

[59] G.-E. Onac, *High Frequency Noise Detection in Mesoscopic Devices*. PhD thesis, TU Delft, 2005.

[60] J. B. Johnson, "Thermal Agitation of Electricity in Conductors," *Physical Review*, vol. 32, pp. 97–109, jul 1928.

[61] H. Nyquist, "Thermal Agitation of Electric Charge in Conductors," *Physical Review*, vol. 32, pp. 110–113, jul 1928.

[62] S. Kogan, *Electronic Noise and Fluctuations in Solids*. Cambridge University Press, 2008.

[63] U. Fano, "Ionization Yield of Radiations. II. The Fluctuations of the Number of Ions," *Physical Review*, vol. 72, pp. 26–29, jul 1947.

[64] B. J. van Wees, H. van Houten, C. W. J. Beenakker, J. G. Williamson, L. P. Kouwenhoven, D. van der Marel, and C. T. Foxon, "Quantized conductance of point contacts in a two-dimensional electron gas," *Physical Review Letters*, vol. 60, pp. 848–850, feb 1988.

[65] H. Birk, M. J. M. de Jong, and C. Schönenberger, "Shot-Noise Suppression in the Single-Electron Tunneling Regime," *Physical Review Letters*, vol. 75, pp. 1610–1613, aug 1995.

[66] A. Nauen, I. Hapke-Wurst, F. Hohls, U. Zeitler, R. J. Haug, and K. Pierz, "Shot noise in self-assembled InAs quantum dots," *Physical Review B*, vol. 66, p. 161303, oct 2002.

[67] A. Nauen, F. Hohls, N. Maire, K. Pierz, and R. J. Haug, "Shot noise in tunneling through a single quantum dot," *Physical Review B*, vol. 70, p. 033305, jul 2004.

[68] C. A. Merchant and N. Markovic, "Current and shot noise measurements in a carbon nanotube-based spin diode (invited)," *Journal of Applied Physics*, vol. 105, no. 7, p. 07C711, 2009.

[69] S. Kafanov and P. Delsing, "Measurement of the shot noise in a single-electron transistor," *Physical Review B*, vol. 80, p. 155320, oct 2009.

[70] R. Aguado and L. P. Kouwenhoven, "Double Quantum Dots as Detectors of High-Frequency Quantum Noise in Mesoscopic Conductors," *Physical Review Letters*, vol. 84, no. 9, pp. 1986–1989, 2000.

[71] E. Onac, F. Balestro, B. Trauzettel, C. F. J. Lodewijk, and L. P. Kouwenhoven, "Shot-Noise Detection in a Carbon Nanotube Quantum Dot," *Physical Review Letters*, vol. 96, p. 026803, jan 2006.

[72] R. J. Schoelkopf, A. A. Clerk, S. M. Girvin, K. W. Lehnert, and M. H. Devoret, "Qubits as Spectrometers of Quantum Noise," in *Quantum Noise in Mesoscopic Physics*, pp. 175–203, Springer Netherlands, 2003.

[73] D. C. Glattli, P. Jacques, A. Kumar, P. Pari, and L. Saminadayar, "A noise detection scheme with 10 mK noise temperature resolution for semiconductor single electron tunneling devices," *Journal of Applied Physics*, vol. 81, no. 11, p. 7350, 1997.

[74] M. Reznikov, R. D. Picciotto, T. G. Griffiths, M. Heiblum, and V. Umansky, "Observation of quasiparticles with one-fifth of an electron's charge," *Nature*, vol. 399, pp. 238–241, may 1999.

[75] T. Hasler, M. Jung, V. Ranjan, G. Puebla-Hellmann, A. Wallraff, and C. Schönenberger, "Shot Noise of a Quantum Dot Measured with Gigahertz Impedance Matching," *Physical Review Applied*, vol. 4, p. 054002, nov 2015.

[76] M. Hashisaka, Y. Yamauchi, S. Nakamura, S. Kasai, K. Kobayashi, and T. Ono, "Measurement for quantum shot noise in a quantum point contact at low temperatures," *Journal of Physics: Conference Series*, vol. 109, p. 012013, 2008.

[77] L. DiCarlo, Y. Zhang, D. T. McClure, C. M. Marcus, L. N. Pfeiffer, and K. W. West, "System for measuring auto- and cross correlation of current noise at low temperatures," *Review of Scientific Instruments*, vol. 77, no. 7, p. 073906, 2006.

[78] D. T. McClure, L. DiCarlo, Y. Zhang, H.-A. Engel, C. M. Marcus, M. P. Hanson, and A. C. Gossard, "Tunable Noise Cross Correlations in a Double Quantum Dot," *Physical Review Letters*, vol. 98, p. 056801, jan 2007.

[79] M. Hashisaka, Y. Yamauchi, S. Nakamura, S. Kasai, T. Ono, and K. Kobayashi, "Bolometric detection of quantum shot noise in coupled mesoscopic systems," *Physical Review B*, vol. 78, p. 241303, dec 2008.

[80] R. Leturcq, C. Stampfer, K. Inderbitzin, L. Durrer, C. Hierold, E. Mariani, M. G. Schultz, F. von Oppen, and K. Ensslin, "Franck-Condon blockade in suspended carbon nanotube quantum dots," *Nature Physics*, vol. 5, no. 5, p. 327, 2008.

[81] H. Park, J. Park, A. K. L. Lim, E. H. Anderson, A. P. Alivisatos, and P. L. McEuen, "Nanomechanical oscillations in a single C_{60} transistor," *Nature*, pp. 57–60, 2000.

[82] J. Koch and F. von Oppen, "Franck-Condon Blockade and Giant Fano Factors in Transport through Single Molecules," *Physical Review Letters*, vol. 94, p. 206804, may 2005.

[83] J. Koch, F. von Oppen, and A. V. Andreev, "Theory of the Franck-Condon blockade regime," *Physical Review B*, vol. 74, p. 205438, nov 2006.

[84] J. Franck, "Elementary processes of photochemical rections," *Trans. Faraday Soc.*, no. 1923, p. 536, 1924.

[85] E. Condon, "A theory of intensity distribution in band systems," *Physical Review*, vol. 28, no. 6, pp. 1182–1201, 1926.

[86] K. Flensberg, "Electron–vibron coupling in suspended nanotubes," *New Journal of Physics*, vol. 8, no. 1, p. 5, 2006.

[87] S. Braig and K. Flensberg, "Vibrational sidebands and dissipative tunneling in molecular transistors," *Physical Review B*, vol. 68, p. 205324, nov 2003.

[88] S. Sapmaz, P. Jarillo-Herrero, Y. M. Blanter, C. Dekker, and H. S. J. van der Zant, "Tunneling in Suspended Carbon Nanotubes Assisted by Longitudinal Phonons," *Physical Review Letters*, vol. 96, p. 026801, jan 2006.

[89] A. Yar, A. Donarini, S. Koller, and M. Grifoni, "Dynamical symmetry breaking in vibration-assisted transport through nanostructures," *Physical Review B*, vol. 84, p. 115432, sep 2011.

[90] W. Belzig, "Full counting statistics of super-Poissonian shot noise in multilevel quantum dots," *Physical Review B*, vol. 71, p. 161301, apr 2005.

[91] Private communication with M. Niklas.

[92] L. DiCarlo, *Mesoscopic Electronics Beyond DC Transport*. PhD thesis, Harvard University, 2007.

[93] F. Pobell, *Matter and Methods at Low Temperatures*. Springer Berlin Heidelberg, third, rev ed., 2007.

[94] B. D. Myers and V. P. Dravid, "Variable Pressure Electron Beam Lithography (VPe BL): A New Tool for Direct Patterning of Nanometer-Scale Features on Substrates with Low Electrical Conductivity," *Nano Letters*, vol. 6, pp. 963–968, may 2006.

[95] Avago Technologies, *Low Noise Pseudomorphic HEMT in a Surface Mount Plastic Package*, 6 2012. AV02-1283EN.

[96] J. Kong, H. T. Soh, A. M. Cassell, C. F. Quate, and H. Dai, "Synthesis of individual single-walled carbon nanotubes on patterned silicon wafers," *Nature*, vol. 395, pp. 878–881, oct 1998.

[97] S. Yasin, D. Hasko, and H. Ahmed, "Comparison of MIBK/IPA and water/IPA as PMMA developers for electron beam nanolithography," *Microelectronic Engineering*, vol. 61-62, pp. 745–753, 2002.

[98] C. Enss and S. Hunklinger, *Low-Temperature Physics*. Berlin, Heidelberg: Springer-Verlag, 2005.

[99] D. Bozovic, M. Bockrath, J. H. Hafner, C. M. Lieber, H. Park, and M. Tinkham, "Electronic properties of mechanically induced kinks in single-walled carbon nanotubes," *Applied Physics Letters*, vol. 78, no. 23, p. 3693, 2001.

[100] G. Abulizi, A. Baumgartner, and C. Schönenberger, "Full characterization of a carbon nanotube parallel double quantum dot," *physica status solidi (b)*, vol. 5, pp. 1–5, jul 2016.

[101] J. Lefebvre, R. Antonov, M. Radosavljević, J. Lynch, M. Llaguno, and A. Johnson, "Single-wall carbon nanotube based devices," *Carbon*, vol. 38, no. 11-12, pp. 1745–1749, 2000.

[102] W. Clauss, D. J. Bergeron, M. Freitag, C. L. Kane, E. J. Mele, and A. T. Johnson, "Electron backscattering on single-wall carbon nanotubes observed by scanning tunneling microscopy," *Europhysics Letters (EPL)*, vol. 47, pp. 601–607, sep 1999.

[103] T. Sakamoto, S. Hwang, F. Nihey, Y. Nakamura, and K. Nakamura, "Coulomb Blockade of Two Quantum Dots in Series," *Japanese Journal of Applied Physics*, vol. 33, pp. 4876–4877, sep 1994.

[104] D. O. Preusche-Rogstad, *Spin blockade spectroscopy in a carbon nanotube double quantum dot transistor*. PhD thesis, Universität Regensburg, mar 2012.

[105] L. P. Kouwenhoven, D. G. Austing, and S. Tarucha, "Few-electron quantum dots," *Rep. Prog. Phys*, vol. 64, pp. 701–736, 2001.

[106] D. H. Cobden, M. Bockrath, P. L. McEuen, A. G. Rinzler, and R. E. Smalley, "Spin Splitting and Even-Odd Effects in Carbon Nanotubes," *Physical Review Letters*, vol. 81, pp. 681–684, jul 1998.

[107] F. Cavaliere, E. Mariani, R. Leturcq, C. Stampfer, and M. Sassetti, "Asymmetric Franck-Condon factors in suspended carbon nanotube quantum dots," *Physical Review B*, vol. 81, p. 201303, may 2010.

[108] M. S. Dresselhaus and P. C. Eklund, "Phonons in carbon nanotubes," *Advances in Physics*, vol. 49, pp. 705–814, sep 2000.

[109] H. Suzuura and T. Ando, "Phonons and electron-phonon scattering in carbon nanotubes," *Physical Review B*, vol. 65, p. 235412, may 2002.

[110] B. J. LeRoy, S. G. Lemay, J. Kong, and C. Dekker, "Electrical generation and absorption of phonons in carbon nanotubes," *Nature*, vol. 432, pp. 371–374, nov 2004.

[111] W. Izumida and M. Grifoni, "Phonon-assisted tunneling in interacting suspended single wall carbon nanotubes," *New Journal of Physics*, vol. 7, p. 244, 2005.

[112] A. Donarini, A. Yar, and M. Grifoni, "Spectrum and Franck–Condon factors of interacting suspended single-wall carbon nanotubes," *New Journal of Physics*, vol. 14, p. 023045, feb 2012.

[113] C. Meyer, J. M. Elzerman, and L. P. Kouwenhoven, "Photon-Assisted Tunneling in a Carbon Nanotube Quantum Dot," *Nano Letters*, vol. 7, pp. 295–299, feb 2007.

[114] J. Gramich, A. Baumgartner, and C. Schönenberger, "Resonant and Inelastic Andreev Tunneling Observed on a Carbon Nanotube Quantum Dot," *Physical Review Letters*, vol. 115, p. 216801, nov 2015.

[115] B. Camarota, F. Parage, F. Balestro, P. Delsing, and O. Buisson, "Experimental Evidence of One-Dimensional Plasma Modes in Superconducting Thin Wires," *Physical Review Letters*, vol. 86, pp. 480–483, jan 2001.

[116] A. K. Hüttel, M. Poot, B. Witkamp, and H. S. J. van der Zant, "Nanoelectromechanics of suspended carbon nanotubes," *New Journal of Physics*, vol. 10, p. 095003, sep 2008.

[117] A. K. Hüttel, B. Witkamp, M. Leijnse, M. R. Wegewijs, and H. S. J. van der Zant, "Pumping of Vibrational Excitations in the Coulomb-Blockade Regime in a Suspended Carbon Nanotube," *Physical Review Letters*, vol. 102, p. 225501, jun 2009.

[118] K. C. Nowack and M. R. Wegewijs, "Vibration-assisted tunneling through competing molecular states," *arXive: cond-mat/0506552*, pp. 1–16, jun 2005.

[119] W. Häusler, K. Jauregui, D. Weinmann, T. Brandes, and B. Kramer, "Negative differential conductance in non-linear transport of quantum dots," *Physica B: Condensed Matter*, vol. 194-196, pp. 1325–1326, feb 1994.

[120] A. T. Johnson, L. P. Kouwenhoven, W. de Jong, N. C. van der Vaart, C. J. P. M. Harmans, and C. T. Foxon, "Zero-dimensional states and single electron charging in quantum dots," *Physical Review Letters*, vol. 69, pp. 1592–1595, sep 1992.

[121] A. Thielmann, M. H. Hettler, J. König, and G. Schön, "Super-Poissonian noise, negative differential conductance, and relaxation effects in transport through molecules, quantum dots, and nanotubes," *Physical Review B*, vol. 71, p. 045341, jan 2005.

[122] D. Chevallier, J. Rech, T. Jonckheere, and T. Martin, "Current and noise correlations in a double-dot Cooper-pair beam splitter," *Physical Review B*, vol. 83, p. 125421, mar 2011.

[123] Private communication with Dr. N. Paradiso.

[124] H. B. Callen and R. F. Greene, "On a Theorem of Irreversible Thermodynamics," *Physical Review*, vol. 86, pp. 702–710, jun 1952.

Acknowledgment

This work would never have been accomplished without the help of many people. In particular, I would like to thank

- My advisor Prof. Dr. Christoph Strunk for giving me the opportunity to work on this interesting topic of shot noise measurements.
- Prof. Dr. Milena Grifoni who agreed to act as second referee for my thesis and for the help with the theoretical analysis of our measurements
- Prof. Dr. Dieter Weiss for providing the clean room facilities and other infrastructure at the chair.
- Dr. Nicola Paradiso for his help with the circuit analysis, the fabrication of our QPC-chip and many other things concerning the cryostat and electronics.
- Our technicians Tom Haller, Uli Gürster, Michael Weigl, Daniel Pahl and Cornelia Linz for the technical support in the clean room, the cryolab as well as the UHV lab.
- Prof. Dr. Dominique Bougeard and Imke Gronwald for providing the 2DEG material for our calibration chip.
- Michael Schafberger for carrying out the calibration measurements.
- Michael Niklas and Dr. Andrea Donarini for providing the code for the numerical simulations and for the help in our numerous discussions.
- Elke Haushalter und Claudia Rahm for adminstrative and moral support.
- Thomas Solleder and Christian Haimerl for their supply with liquid helium.
- The electronics workshop, especially Dieter Riedl and Gerhard Peter for the fabrication of our sample holders and the supply with electronic parts.
- Dr. Andreas Hüttel, Christian Butschkow, Dr. Alois Dirnaichner and Dr. Stefan Geißler for helping me with Lab::Measurement.
- All members of the group for the pleasant atmosphere.
- My family for their support.